

WASHINGTON UNIVERSITY IN ST. LOUIS

McKelvey School of Engineering

Dissertation Examination Committee:

Tammie Lee Smith Benzinger, Chair

Janine Diane Bijsterbosch

Abhinav Kumar Jha

Richard Justin Perrin

Aristeidis Sotiras

To Ascertain Scientific Reliability in PET Imaging for Alzheimer Disease

by

Charles Dan Chen

A dissertation presented to
the McKelvey School of Engineering
of Washington University in
partial fulfillment of the
requirements for the degree
of Doctor of Philosophy

May 2023

St. Louis, Missouri

© 2023, Charles Dan Chen

Table of Contents

List of Figures	v
List of Tables	vi
Acknowledgments.....	vii
Abstract	ix
Chapter 1: Comparing tau PET visual interpretation with tau PET quantification, CSF biomarkers, and longitudinal clinical assessment.....	1
1.1 Abstract	1
1.1.1 Background	1
1.1.2 Objective	1
1.1.3 Methods.....	1
1.1.4 Results.....	2
1.1.5 Conclusion	2
1.2 Introduction	2
1.3 Materials and Methods	4
1.3.1 Study participants.....	4
1.3.2 Clinical and cognitive assessment.....	4
1.3.3 Tau PET acquisition.....	4
1.3.4 Tau PET SUVR.....	5
1.3.5 Tau PET visual interpretation	5
1.3.6 A β PET.....	6
1.3.7 MR acquisition.....	6
1.3.8 CSF	7
1.3.9 Statistical analyses	7
1.4 Results	8
1.4.1 Study participants.....	8
1.4.2 Tau PET visual interpretation and tau PET SUVR.....	9
1.4.3 Incidental findings.....	10
1.4.4 CSF p-tau181	11
1.4.5 Clinical and cognitive assessment.....	12
1.5 Conclusions	15

Chapter 2: Ante- and postmortem tau in autosomal dominant and late-onset Alzheimer disease	20
2.1 Abstract	20
2.2 Introduction	20
2.3 Methods	21
2.4 Results	22
2.5 Discussion	24
Chapter 3: Comparing amyloid- β plaque burden with antemortem PiB PET in autosomal dominant and late-onset Alzheimer disease.....	28
3.1 Abstract	28
3.2 Introduction	29
3.3 Materials and methods	31
3.3.1 Cohort demographics	31
3.3.2 Postmortem neuropathology	33
3.3.3 Antemortem PiB PET imaging	35
3.3.4 Statistical analysis	36
3.4 Results	37
3.4.1 Cohort demographics	37
3.4.2 Correlations between PiB PET and stereologic measurements	38
3.4.3 Differences between ADAD and LOAD as measured by PiB PET and stereology	39
3.4.4 PiB PET staging in ADAD versus LOAD	42
3.5 Discussion	43
Chapter 4: Longitudinal head-to-head comparison of ^{11}C -PiB and ^{18}F -florbetapir PET in a Phase 2/3 clinical trial of anti-amyloid- β monoclonal antibodies in dominantly inherited Alzheimer disease	56
4.1 Abstract	56
4.1.1 Purpose.....	56
4.1.2 Methods.....	56
4.1.3 Results.....	57
4.1.4 Conclusion	57
4.2 Introduction	58
4.3 Materials and methods	59
4.3.1 Study approval	59

4.3.2 Participant characteristics	60
4.3.3 A β PET acquisition	60
4.3.4 MRI acquisition	61
4.3.5 Statistical analysis of DIAN-TU-001 data	61
4.3.6 Statistical simulations	62
4.4 Results	64
4.4.1 DIAN-TU-001 clinical trial results	64
4.4.2 Simulated clinical trial results	70
4.5 Discussion	71
Chapter 5: Future directions.....	77
References	86

List of Figures

Figure 1.1: Comparison of tau PET visual interpretation with tau PET SUVR	9
Figure 1.2: Three cases with tau-positive visual interpretations, but tau-negative SUVRs	10
Figure 1.3: Two cases of incidental meningioma with tau PET uptake	11
Figure 1.4: Comparison of tau PET visual interpretation with CSF p-tau181 concentration.....	12
Figure 2.1: Exemplar PHF-1 immunostained neuropil threads, neurofibrillary tangles, and neuritic plaques.....	23
Figure 3.1: Regional differences between ADAD and LOAD as measured by [11C]PiB PET SUVRs and plaque area fractions.....	40
Figure 3.2: Regional differences between ADAD and LOAD as measured by [11C]PiB PET SUVRs while using alternative reference regions.....	42
Figure 3.3: Regional distributions of PiB PET SUVRs in ADAD and LOAD	43
Figure 4.1: Rates of longitudinal change in global cortical SUVRs and Centiloids.....	67
Figure 4.2: Rates of longitudinal change in regional SUVRs.....	68
Figure 4.3: Rates of longitudinal change in regional Centiloids	69
Figure 4.4: Rates of longitudinal change in regional SUVRs versus regional Centiloids	70

List of Tables

Table 1.1: Participant characteristics	8
Table 1.2: AD biomarker status for cases with positive tau PET visual interpretation but negative tau PET SUVR analysis	10
Table 1.3: AD biomarker status for cases with incidental meningioma.....	11
Table 1.4: Participant characteristics for those who underwent lumbar puncture.....	12
Table 1.5: Cognitively normal participant follow up	13
Table 1.6: Cognitively impaired participant follow up	14
Table 2.1: Cohort demographics	21
Table 3.1: Cohort demographics	32
Table 3.2: Regional correlations between [11C]PiB PET SUVRs and plaque area fractions.....	38
Table 3.3: Extended imaging cohort demographics	39
Table 4.1: A β PET radiotracers used in Phase 2 and Phase 3 clinical trials of anti-A β monoclonal antibodies for AD	58
Table 4.2: Participant characteristics.....	60
Table 4.3: Mean baseline global cortical SUVR and Centiloid in the gantenerumab and placebo arms as measured by ¹¹ C-PiB and ¹⁸ F-florbetapir.....	65
Table 4.4: Mean rates of longitudinal change in global cortical SUVR and Centiloid in the gantenerumab and placebo arms as measured by ¹¹ C-PiB and ¹⁸ F-florbetapir	66
Table 4.5: Types I error and power (%) comparison when using both Centiloid- ¹¹ C-PiB and Centiloid- ¹⁸ F-florbetapir in 1000 simulated clinical trials	71

Acknowledgments

I am supported by the NSF GRFP (DGE-1745038 and DGE-2139839) and the Knight ADRC T32 (5T32AG058518-04).

Charles Dan Chen

Washington University in St. Louis

May 2023

Dedicated to my parents and grandparents.

ABSTRACT OF THE DISSERTATION

To Ascertain Scientific Reliability in PET Imaging for Alzheimer Disease

by

Charles Dan Chen

Doctor of Philosophy in Imaging Science

Washington University in St. Louis, 2023

Professor Tammie Lee Smith Benzinger, Chair

Alzheimer disease is one of the deadliest and most expensive diseases in the United States. Knowing whether a family member has Alzheimer disease may help households better plan for health-related expenses. However, fewer than half of primary care physicians report being comfortable diagnosing cognitive impairment due to Alzheimer disease. One solution is to supplement cognitive assessments with biomarkers to track abnormal levels of amyloid- β and tau, the pathological hallmarks of Alzheimer disease. Among these, positron emission tomography (PET) has emerged as an established standard that other biomarkers are compared to. However, as PET imaging moves from being used in research settings to clinical settings, its reliability must be established once more under these new conditions. In this dissertation, I aim to ascertain scientific reliability in PET imaging for Alzheimer disease as the technology moves from being used as a quantitative measure to being used for visual reads (Chapter 1, published as Chen, C.D. et al., Comparing tau PET visual interpretation with tau PET quantification, CSF biomarkers, and longitudinal clinical assessment, *Journal of Alzheimer's Disease*, 2023); from being used in patients with late-onset Alzheimer disease to patients with rare, dominantly inherited forms of Alzheimer disease (Chapter 2, published as Chen, C.D. et al., Ante- and postmortem tau in autosomal dominant and late-onset Alzheimer's disease, *Annals of Clinical and Translational*

Neurology, 2020 and Chapter 3, published as Chen, C.D. et al., Comparing amyloid- β plaque burden with antemortem PiB PET in autosomal dominant and late-onset Alzheimer disease, *Acta Neuropathologica*, 2021); and from being used for tracking disease progression in observational studies to tracking treatment effects in clinical trials (Chapter 4, published as Chen, C.D. et al., Longitudinal head-to-head comparison of ^{11}C -PiB and ^{18}F -florbetapir in a Phase 2/3 clinical trial of anti-amyloid- β monoclonal antibodies in dominantly inherited Alzheimer disease, *European Journal of Nuclear Medicine and Molecular Imaging*, 2023).

Chapter 1: Comparing tau PET visual interpretation with tau PET quantification, CSF biomarkers, and longitudinal clinical assessment

1.1 Abstract

1.1.1 Background

^{18}F -flortaucipir PET received FDA approval to visualize aggregated neurofibrillary tangles (NFTs) in brains of adult patients with cognitive impairment being evaluated for Alzheimer disease (AD). However, manufacturer's guidelines for visual interpretation of ^{18}F -flortaucipir PET differ from how ^{18}F -flortaucipir PET has been measured in research settings using standardized uptake value ratios (SUVRs). How visual interpretation relates to ^{18}F -flortaucipir PET SUVR, CSF biomarkers, or longitudinal clinical assessment is not well understood.

1.1.2 Objective

We compare various diagnostic methods in participants enrolled in longitudinal observational studies of aging and memory (n=189, 23 were cognitively impaired).

1.1.3 Methods

Participants had tau PET, A β PET, MRI, and clinical and cognitive evaluation within 18 months (n=189); the majority (n=144) also underwent lumbar puncture. Two radiologists followed manufacturer's guidelines for ^{18}F -flortaucipir PET visual interpretation.

1.1.4 Results

Visual interpretation had high agreement with SUVR (98.4%) and moderate agreement with CSF p-tau181 (86.1%). Two participants demonstrated ^{18}F -flortaucipir uptake from meningiomas.

Visual interpretation could not predict follow-up clinical assessment in 9.52% of cases.

1.1.5 Conclusion

Visual interpretation was highly consistent with SUVR (discordant participants had hemorrhagic infarcts or occipital-predominant AD NFT deposition) and moderately consistent with CSF p-tau181 (discordant participants had AD pathophysiology not detectable on tau PET). However, close association between AD NFT deposition and clinical onset in group-level studies does not necessarily hold at the individual level, with discrepancies arising from atypical AD, vascular dementia, or frontotemporal dementia. A better understanding of relationships across imaging, CSF biomarkers, and clinical assessment is needed to provide appropriate diagnoses for these individuals.

1.2 Introduction

The pathological hallmarks of Alzheimer disease (AD) are amyloid- β ($\text{A}\beta$) plaques and misfolded hyperphosphorylated tau neurofibrillary tangles (NFTs) [1,2]. *In vivo* evaluation of aggregated tau or associated pathophysiology in AD was first performed using immunoassays for cerebrospinal fluid (CSF) tau phosphorylated at position 181 (p-tau) [3]. Later, tau PET radiotracers were developed [4–6], along with methods for tau PET standardized uptake value ratio (SUVR) analyses [7,8]. The first generation of tau PET radiotracers includes the arylquinoline derivatives ^{18}F -THK5317 and ^{18}F -THK5351, the pyrido-indole derivative ^{18}F -flortaucipir, and the phenyl/pyridinyl-butadienyl-benzothiazole/benzothiazolium derivative ^{11}C -PBB3. Among these, ^{18}F -flortaucipir (TauvidTM, Avid Radiopharmaceuticals) became the first to be approved by the

United States Food and Drug Administration to estimate the density and distribution of aggregated tau NFTs in adult patients with cognitive impairment being evaluated for AD. Following the manufacturer's guidelines for performing a visual interpretation of ^{18}F -flortaucipir PET imaging involves identifying the presence or absence of contiguous radiotracer uptake greater than 1.65 times the cerebellar uptake in either the posterolateral temporal, occipital, or parietal/precuneus regions. This method differs greatly from most research procedures for automated quantification of tau PET imaging data, such as taking the volume-weighted mean standardized uptake value ratio (SUVR) in a temporal meta-region of interest (ROI) and comparing that to a cohort-defined threshold [7,8]. These methodological differences may lead to disagreements between visual interpretation and SUVR quantification. In particular, the temporal meta-ROI often used in SUVR quantification does not contain any of the occipital or parietal/precuneus structures used in visual interpretation, and includes several medial temporal lobe structures ignored in visual interpretation. Additionally, in the clinic ^{18}F -flortaucipir PET imaging is only indicated for use in adult patients with cognitive impairment who are being evaluated for AD, whereas in a research setting ^{18}F -flortaucipir PET imaging is performed regardless of cognitive status, calling into question whether ^{18}F -flortaucipir PET imaging is a reliable measure of NFT deposition during preclinical stages of AD. Tau pathophysiology can also be evaluated by measuring phosphorylated tau concentrations in the CSF, and several studies have provided additional evidence that tau PET is more strongly coupled to cognitive decline, whereas CSF p-tau181 is more tightly linked to preclinical AD [9–12]. Understanding where these three methods – tau PET visual interpretation, tau PET SUVR quantification, and CSF p-tau181 concentration – agree and differ may improve how we define AD NFT deposition and AD clinical diagnoses.

1.3 Materials and Methods

1.3.1 Study participants

Participants selected for this study were enrolled in longitudinal observational studies of aging and memory at the Charles F. and Joanne Knight Alzheimer Disease Research Center (Knight ADRC, n=189, of whom 23 were cognitively impaired, Table 1.1). All participants met the inclusion criteria of having a tau PET usable for visual reads, and an A β PET, MRI, and clinical and cognitive evaluation, all within 18 months; the majority of participants (n=144) also underwent lumbar puncture within 18 months of their tau PET scan. The study was approved by the Washington University in St. Louis Human Research Protection Office and Institutional Review Board, and all participants or their designees signed an informed consent form.

1.3.2 Clinical and cognitive assessment

Participants were assessed clinically and cognitively using the neuropsychological test battery from the Uniform Data Set (UDS) [13], which includes the Clinical Dementia Rating (CDR®) [14] and the Mini Mental State Examination (MMSE) [15]. The CDR assesses three domains of cognition (memory, orientation, judgment and problem solving) and three domains of function (community affairs, home and hobbies, personal care): scores from the six domains can either be summed to yield the CDR Sum of Boxes score, or passed to a lookup table to yield the CDR Global score.

1.3.3 Tau PET acquisition

Participants were scanned on a Siemens Biograph 40 TruePoint (Siemens Healthineers). Participants received a single intravenous bolus injection (341 ± 29.8 MBq) of ^{18}F -flortaucipir (Tauvid™, Avid Radiopharmaceuticals). Emission data were collected 80-100 minutes post injection. List-mode data were reconstructed using ordered subset expectation maximization with

three iterations and 21 subsets. A low-dose CT scan preceded PET acquisition for attenuation correction.

1.3.4 Tau PET SUVR

Reconstructed PET images were processed using the PET Unified Pipeline (<https://github.com/ysu001/PUP>) and coregistered to corresponding MR images [16,17]. After segmenting MR images into regions of interest (ROIs) using FreeSurfer version 5.3 [18], regional SUVRs were defined from the reconstructed PET images using a cerebellar gray reference region. The temporal meta-ROI SUVR was defined as the volume-weighted mean SUVR of the amygdala, entorhinal cortex, fusiform, parahippocampal, inferior temporal, and middle temporal ROIs [7,8].

1.3.5 Tau PET visual interpretation

Two radiologists with training in nuclear medicine (J.A.L. and M.R.P.) followed the manufacturer's guidelines for ^{18}F -flortaucipir PET visual interpretation of participant scans using MIM Encore (MIM Software). Reconstructed PET images were coregistered with corresponding MR images. A ROI was drawn around the whole cerebellum in the axial plane that maximizes its cross-sectional area. A color scale with a rapid transition at 1.65 times the mean cerebellar counts was defined. The temporal lobe was divided into the anterolateral, anterior mesial, posterolateral, and posterior mesial temporal quadrants by placing the horizontal crosshair posterior to the brainstem nuclei, and the vertical crosshair at the widest portion of the temporal pole. An image was considered positive if it showed contiguous activity above the rapid transition/cutoff in the cortical gray matter of the posterolateral temporal, occipital, or parietal/precuneus regions. An image was considered negative if it showed no activity above the cutoff in the cortical gray matter of the posterolateral temporal, occipital, or parietal/precuneus regions, or if it showed activity above the cutoff in the cortical gray matter restricted to the medial temporal, anterolateral temporal

and frontal regions. Off-target binding, which may be seen in the choroid plexus, striatum, and brainstem nuclei, and small foci of noncontiguous activity, which may be seen throughout the cortical gray matter, were not used when determining tau positivity. Radiologists were blinded to all other information about each participant. In addition to following the manufacturer's guidelines for ^{18}F -flortaucipir PET visual interpretation, in this study, radiologists also reported whether radiotracer activity was symmetric across left and right hemispheres and whether there was off-target binding in the choroid plexus, striatum, brainstem nuclei, or bone/meninges. Notable findings (such as incidental meningiomas) were also reported. Both radiologists determined off-target binding and incidental findings using MR imaging. Additionally, incidental findings were confirmed with a neuroradiologist (T.L.S.B.).

1.3.6 A β PET

Participants were scanned on either a Siemens Biograph 40 TruePoint, Biograph mMR, or Biograph Vision 600 (Siemens Healthineers). Participants received either a single intravenous bolus injection (539 ± 159 MBq) of ^{11}C -Pittsburgh compound B (PiB) or (369 ± 22.4 MBq) of ^{18}F -florbetapir (AmyvidTM, Avid Radiopharmaceuticals). Emission data were either collected 30-60 minutes post injection (^{11}C -PiB) or 50-70 minutes post injection (^{18}F -florbetapir). Reconstructed PET images were formed and pre-processed in the same manner as tau PET. An A β PET SUVR was defined for each radiotracer [16,17] and standardized to the Centiloid scale [19,20].

1.3.7 MR acquisition

Participants were scanned on either a Siemens Biograph mMR or Magnetom Vida (Siemens Healthineers). Across all scanners, T1-weighted head MR images were acquired using a magnetization prepared rapid gradient echo (MPRAGE) generalized autocalibrating partial

parallel acquisition (GRAPPA) sequence using a repetition time=2300 ms, echo time=2.95 ms, flip angle=9°, at 1.1x1.1x1.2 mm³ voxel resolution.

1.3.8 CSF

CSF was collected under standardized operating procedures. Participants underwent lumbar puncture in the morning following overnight fasting and 20-30 ml of CSF was collected in a 50 ml polypropylene tube via gravity drip using an atraumatic Sprotte 22-gauge spinal needle. CSF samples were kept on ice and centrifuged at low speed within two hours of collection, then transferred to another 50 ml tube to remove cells. CSF was aliquoted at 500 µl into polypropylene tubes and stored at -80°C. Concentrations of CSF p-tau181, Aβ42, and Aβ40 were measured by chemiluminescent enzyme immunoassay using a fully automated platform (LUMIPULSE G1200, Fujirebio) according to the manufacturer's specifications.

1.3.9 Statistical analyses

Cutoffs for binarizing tau PET, Aβ PET, CSF p-tau181, and CSF Aβ42/Aβ40 values were determined by fitting a two-component univariate Manly mixture model [21] in R software [22] to all relevant baseline PET SUVR or CSF measurements available in the Knight ADRC Data Freeze 17 (Supplementary table 1) and finding the decision boundary. Manly mixture modeling was used to account for possible severe skewness in the data that would be difficult to model using Gaussian mixture modeling, and to account for skewness that can vary from component to component, which would be impossible to model using log or Box-Cox transformations [21]. Cohen's kappa (κ) was used to measure inter-rater reliability between the two radiologists' tau PET visual interpretations, as well as between tau PET visual interpretation and tau PET SUVR quantification, and between tau PET visual interpretation and CSF p-tau181 concentration.

1.4 Results

1.4.1 Study participants

Overall, participants were on average (\pm standard deviation) 69.8 ± 8.51 years old, most were cognitively normal with a global Clinical Dementia Rating (CDR®) [14] of 0 ($n=166/189$, 87.8%) and most did not carry the *APOE* $\epsilon 4$ allele ($n=120/188$, 63.8%). (Table 1.1). Cognitively normal participants had a mean tau PET temporal meta-ROI SUVR of 1.15 ± 0.106 and a mean Centiloid of 19.9 ± 34.4 . Cognitively impaired participants ($n=23/189$, 12.2%) had a clinical diagnosis of either uncertain dementia ($n=9$), a CDR=0.5 in memory only ($n=1$), or AD dementia ($n=13$). They also had a mean tau PET temporal meta-ROI SUVR of 1.44 ± 0.364 and a mean Centiloid of 74.3 ± 45.6 .

Table 1.1 Participant characteristics

		Cognitively normal	Cognitively impaired	Total
Number		166	23	189
Mean age in years (SD)		68.9 ± 8.34	75.7 ± 7.36	69.8 ± 8.51
Female (%)		93 (56.0)	12 (52.2)	105 (55.6)
Race	White	147	23	170
	Black or African American	18	0	18
	Asian	1	0	1
Mean MMSE (SD)		$29.2 (1.12)$	$26.0 (3.66)$	$28.8 (1.94)$
CDR®	0	166	0	166
	0.5	0	16	16
	1	0	6	6
	2	0	1	1
Clinical diagnosis	Cognitively normal	166	0	166
	Uncertain dementia	0	9	9
	0.5 in memory only	0	1	1
	AD dementia	0	13	13
<i>APOE</i> genotype	2/2	1	0	1
	2/3	27	1	28
	2/4	6	1	7
	3/3	83	8	91
	3/4	42	11	53
	4/4	6	2	8
	Unknown	1	0	1
Tau PET temporal meta-ROI SUVR	Mean \pm SD [min, max]	$1.15 \pm 0.106 [0.924, 1.882]$	$1.44 \pm 0.364 [1.024, 2.43]$	$1.18 \pm 0.185 [0.924, 2.43]$
	Positive (%)	4 (2.41)	13 (56.5)	17 (8.99)
Tau PET visual interpretation	Positive (%)	6 (3.61)	14 (60.9)	20 (10.6)
A β PET (Centiloid)	Mean \pm SD	19.9 ± 34.4	74.3 ± 45.6	26.5 ± 40.0
	Positive (%)	45 (27.1)	19 (82.6)	64 (33.9)

Abbreviations: CDR®=Clinical Dementia Rating®, MMSE=Mini-Mental State Exam, SD=standard deviation.

The following quantitative cutoffs were identified through statistical modeling and are used to determine biomarker positivity in the remainder of the analyses: tau PET temporal meta-ROI SUVR cutoff=1.32, A β PET (Centiloid) cutoff=21.6, CSF p-tau181 cutoff=58.1 pg/ml, and CSF A β 42/A β 40 cutoff=0.0737.

1.4.2 Tau PET visual interpretation and tau PET SUVR

Of the 189 ^{18}F -flortaucipir PET images, 20 (10.6%) were read as positive by both radiologists.

Both radiologists also read 169 images as negative and thus agreed on the overall visual interpretation of each image in the current study ($n=189/189$, 100%, $\kappa=1$). Agreement between visual interpretation and SUVR quantification was high ($n=186/189$, 98.4%, $\kappa=0.910$) (Figure 1.1).

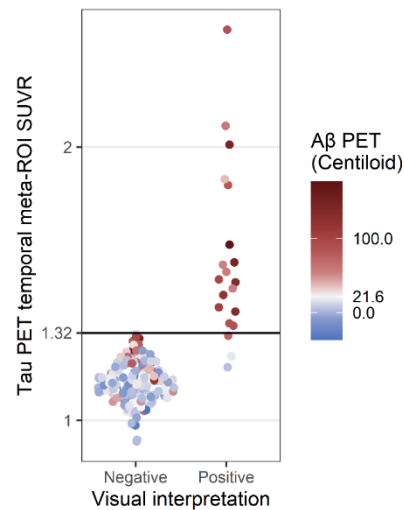


Figure 1.1 Comparison of tau PET visual interpretation with tau PET SUVR. Each PET study was assessed by visual interpretation using the manufacturer's guidelines to determine positivity (x-axis) and by temporal meta-ROI SUVR analysis using a cutoff of $\text{SUVR}=1.32$ to determine positivity (y-axis). The color indicates the A β PET status for each case (positive A β PET, red; negative A β PET, blue; cutoff=21.6 Centiloids).

The three participants who had discordant results between visual interpretation and SUVR quantification all had tau-positive visual interpretations and tau-negative SUVRs. One participant (Figure 1.2a) demonstrated elevated ^{18}F -flortaucipir uptake in the right precuneus and was A β PET, CSF A β 42/A β 40, and CSF p-tau181 negative (Table 1.2). Additional MR imaging revealed a hypointensity on T2*-weighted MRI that colocalized with the elevated right precuneus radiotracer uptake on ^{18}F -flortaucipir PET, suggesting a hemorrhagic infarct to be the cause of elevated radiotracer uptake instead of AD NFT deposition (Figure 1.2b). Upon review of the

additional T2*-weighted MR imaging, the readers also revised their interpretation of the image to be tau negative.

The other two participants (Figures 1.2c and 1.2d) demonstrated lateralized occipital uptake, with greater uptake in either the left (Figure 1.2c) or right (Figure 2d), and were A β PET, CSF A β 42/A β 40, and CSF p-tau181 positive (Table 1.2). The participant with greater left occipital uptake than right, likely has an occipital-predominant form of AD tau pathology [23].

The participant with greater right occipital uptake than left also had posterolateral temporal and parietal/precuneus uptake. The temporal meta-ROI SUVR was borderline negative, suggesting that, perhaps due to the lateralized uptake, the SUVR was artificially low for this case.

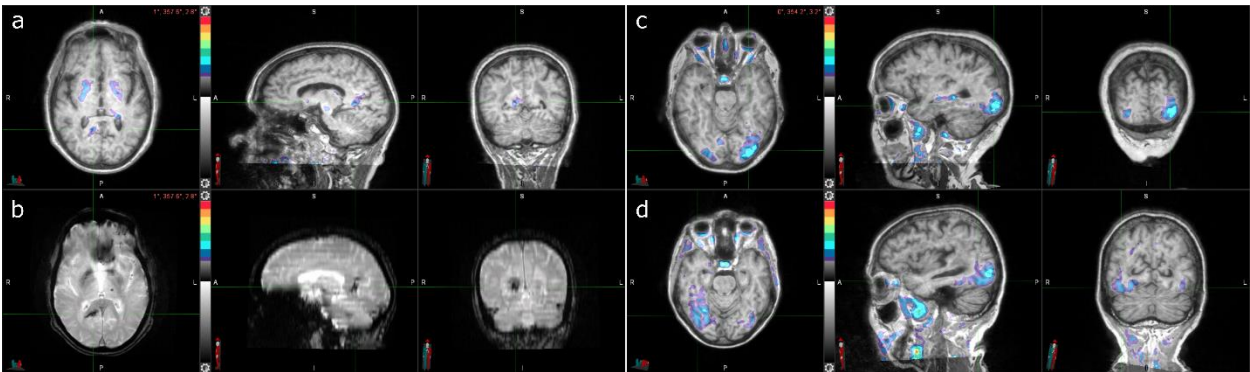


Figure 1.2 Three cases with tau-positive visual interpretations, but tau-negative SUVRs. (a) Tau PET coregistered with MRI of a male participant in his 80s with elevated right precuneus uptake. (b) Corresponding T2*-weighted MRI showing a hypointensity (indicated by the crosshair) that colocalizes with the elevated right precuneus uptake from (a). (c) Tau PET coregistered with MRI of a female participant in her 70s with elevated occipital lobe uptake, left greater than right. (d) Tau PET coregistered with MRI of a female participant in her 70s with elevated posterolateral temporal, occipital, and parietal/precuneus lobe uptake, right greater than left.

	Age	Sex	APOE	CDR®	A β (Centiloid)	PET	Tau (SUVR)	CSF A β 42/A β 40	CSF p-tau181 (pg/ml)
Parietal/precuneus hemorrhagic infarct	80s	Male	3/4	0	3.87		1.19	0.0975	21.6
Left occipital	70s	Female	3/4	0	17.0→ 50.0*		1.23	0.0523	69.2
Right occipital	70s	Female	3/3	0.5	72.1		1.31	0.0493	63.5

Numbers in bold denote positive biomarker status.
 *This participant had a Centiloid=17.0 (below cutoff) approximately one year before their tau PET visit, and a Centiloid=50.0 (above cutoff) approximately two years after their tau PET visit.

1.4.3 Incidental findings

In terms of incidental findings, frontal meningiomas were identified in two participants. One participant had a meningioma in their left posterior frontal lobe (Figure 3a and 3b); the other

participant had it in their left frontal lobe (Figure 1.3c and 1.3d). Both meningiomas had elevated levels of radiotracer uptake. The first participant also had elevated right posterolateral temporal uptake and tau-positive visual interpretation and SUVR and was A β PET positive (Table 1.3). The other participant had tau-negative visual interpretation and SUVR and was A β PET negative.

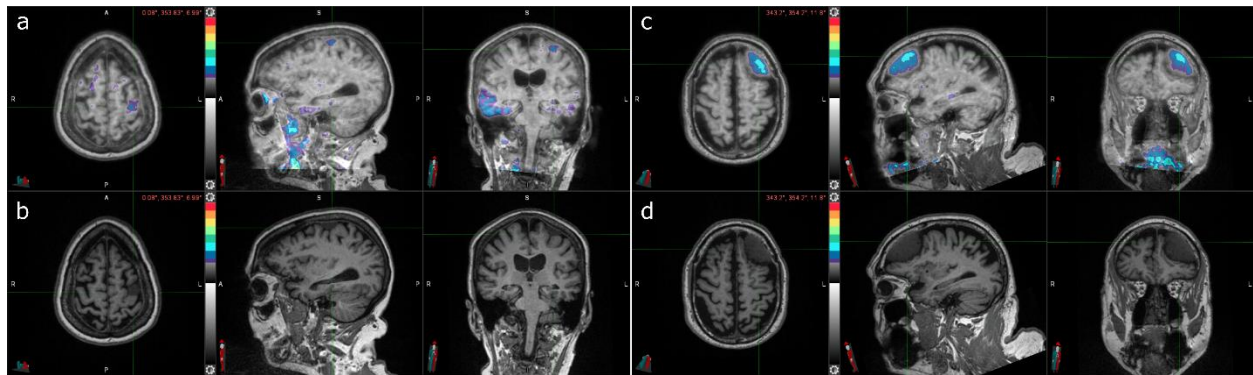


Figure 1.3 Two cases of incidental meningioma with tau PET uptake. (a) Tau PET coregistered with MRI of a female participant in her 70s with a left frontal posterior meningioma (indicated by the crosshair) with tau radiotracer uptake. (b) Corresponding MRI image. (c) Tau PET coregistered with MRI of a male participant in his 70s with a left frontal meningioma (indicated by the crosshair) with tau radiotracer uptake. (d) Corresponding MRI image.

Table 1.3 AD biomarker status for cases with incidental meningioma

	Age	Sex	APOE	CDR®	A β PET (Centiloid)	Tau PET (SUVR)	CSF A β 42/A β 40	CSF p-tau181 (pg/ml)
Left posterior frontal meningioma	70s	Female	2/4	0	177	1.64	0.0481*	49.9*
Left frontal meningioma	70s	Male	2/3	0	8.94	1.16	0.0848*	30.3*

Numbers in bold denote positive biomarker status.

*CSF lumbar punctures were performed approximately 10 years prior to tau PET

1.4.4 CSF p-tau181

Agreement between visual interpretation and CSF p-tau181 was moderate ($n=124/144$, 86.1%, $\kappa=0.526$, Table 1.4). Two participants had tau-positive visual interpretations but were CSF p-tau181 negative (Figure 1.4a and 1.4b). One participant was previously identified as having a tau-positive visual interpretation but tau-negative SUVR (the same case as in Figure 1.2a and 1.2b). The other participant demonstrated posterolateral temporal uptake in both hemispheres and was A β PET and CSF A β 42/A β 40 positive. In addition, 18 participants had tau-negative visual interpretations but were CSF p-tau181 positive (Figure 1.4a and 1.4b). These cases were mostly A β PET positive ($n=14/18$, 77.8%) and/or CSF A β 42/A β 40 positive ($n=17/18$, 94.4%).

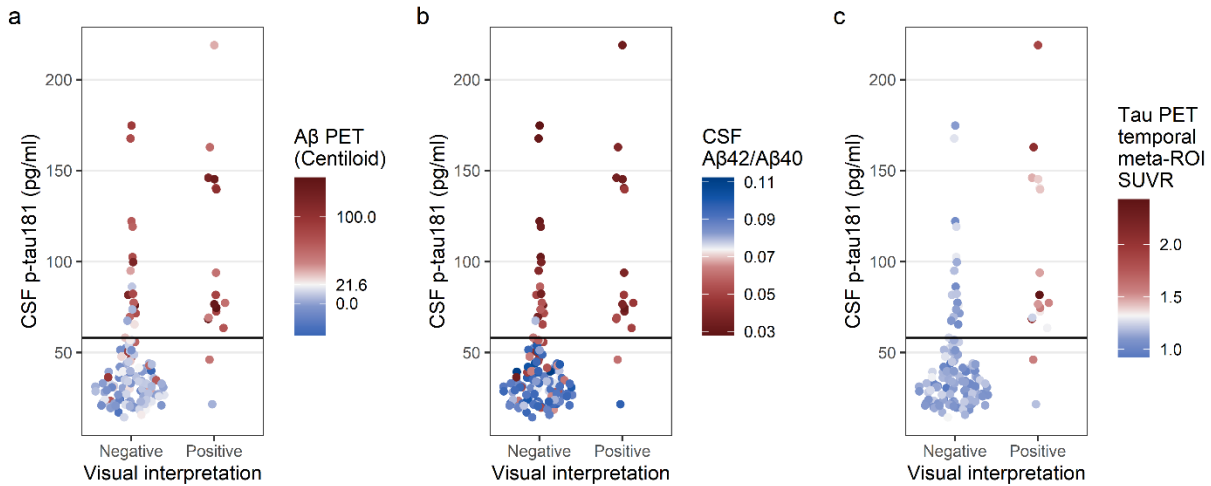


Figure 1.4 Comparison of tau PET visual interpretation with CSF p-tau181 concentration. Each participant is plotted by visual interpretation (x-axis) and CSF p-tau181 concentration (y-axis); participants with p-tau181 \geq 58.1 pg/ml were considered positive. In (a), the color indicates the A β PET status for each participant (positive A β PET, red; negative A β PET, blue; cutoff=21.6 Centiloid). In (b), the color indicates the CSF A β 42/A β 40 status for each participant (positive CSF A β 42/A β 40, red; negative CSF A β 42/A β 40, blue; cutoff=0.0737). In (c), the color indicates the tau PET temporal meta-ROI SUVR status for each participant (positive tau PET, red; negative tau PET, blue; cutoff=1.32 SUVR).

Table 1.4 Participant characteristics for those who underwent lumbar puncture

		Cognitively normal	Cognitively impaired	Total
Number		126	18	144
Mean age in years (SD)		68.6 \pm 8.32	76.1 \pm 7.84	69.5 \pm 8.60
Female (%)		70 (48.6)	10 (55.6)	80 (55.6)
Race	White	114	18	132
	Black or African American	11	0	11
	Asian	1	0	1
Mean MMSE (SD)		29.3 (1.07)	25.7 (3.90)	28.8 (2.06)
CDR®	0	126	0	126
	0.5	0	12	12
	1	0	5	5
	2	0	1	1
Clinical diagnosis	Cognitively normal	126	0	126
	Uncertain dementia	0	6	6
	AD dementia	0	12	12
APOE genotype	2/2	1	0	1
	2/3	22	1	23
	2/4	3	1	4
	3/3	62	7	69
	3/4	31	7	38
	4/4	6	2	8
	Unknown	1	0	1
Tau PET temporal meta-ROI SUVR	Mean \pm SD [min, max]	1.15 \pm 0.108 [0.924, 1.882]	1.47 \pm 0.367 [1.042, 2.43]	1.19 \pm 0.194 [0.924, 2.43]
	Positive (%)	3 (2.38)	11 (61.1)	14 (9.72)
Tau PET visual interpretation	Positive (%)	5 (3.97)	12 (66.7)	17 (11.8)
Aβ PET (Centiloid)	Mean \pm SD	19.0 \pm 32.2	80.3 \pm 46.7	26.7 \pm 39.8
	Positive (%)	34 (27.0)	16 (88.9)	50 (34.7)
CSF p-tau181	Mean \pm SD	42.6 \pm 30.4	88.7 \pm 42.6	48.4 \pm 35.5
	Positive (%)	19 (15.1)	14 (77.8)	33 (22.9)
CSF Aβ42/Aβ40	Mean \pm SD	0.0777 \pm 0.0217	0.0502 \pm 0.0196	0.0743 \pm 0.0233
	Positive (%)	41 (32.5)	16 (88.9)	57 (39.6)

1.4.5 Clinical and cognitive assessment

Six participants were assessed at baseline to be cognitively normal but tau-positive on visual interpretation (Table 1.5). One participant (Case 1) was previously mentioned to have PET radiotracer uptake colocalized to a parietal/precuneus hypointensity on T2*-weighted MRI and no other positive AD biomarkers (Figure 1.2 and Table 1.2). The remaining five participants were all

A β PET positive. No participant reliably converted from cognitively normal to AD dementia. One participant (Case 2) did convert to AD dementia at their three-year follow up, but was reassessed to have a clinical diagnosis of uncertain dementia, more specifically, possible non-AD dementia of vascular origin at their five-year follow up. Another participant (Case 4) converted to AD dementia at their two-year follow up, but was reassessed to have frontotemporal dementia (FTD) at their four-year follow up.

Four participants were assessed at baseline to be cognitively normal and tau-negative on visual interpretation, but would convert to AD dementia at follow up (Table 1.5). Two participants (Case 7 and Case 10) converted to AD dementia at their one-year follow ups, but were reassessed as cognitively normal at their two-year follow ups. The remaining two participants (Case 8 and Case 9) converted to AD dementia at their second- and fourth-year follow ups, respectively, but only Case 2 demonstrated A β PET positivity at baseline.

Table 1.5 Cognitively normal participant follow up

	Age	Sex	APOE	Baseline tau PET temporal meta-ROI	Baseline tau PET visual interpretation	Asymmetry	Baseline Aβ PET (Centiloid)	Yearly follow-up clinical diagnosis				
								1	2	3	4	5
Baseline cognitively normal and tau PET visual interpretation positive												
1*	80s	Male	3/4	1.19	Positive	Right	3.87	CN	CN	CN	CN	CN
2	70s	Male	2/3	1.35	Positive	Left	86.6		CN	AD	AD	UD
3**	70s	Female	3/4	1.23	Positive	Left	17.0→50.0	CN	CN	CN	CN	CN
4	80s	Male	3/3	1.88	Positive	Left	37.6	UD	AD	AD	FTD	
5	80s	Male	3/4	1.54	Positive		57.3	CN				
6***	70s	Female	2/4	1.64	Positive	Right	177	CN	CN	CN		
Baseline cognitively normal (and tau PET visual interpretation negative), but converts at follow up												
7	70s	Female	3/4	1.22	Negative		-2.35	AD	CN	CN		
8	80s	Female	3/4	1.21	Negative		120	CN	AD	AD		
9	50s	Male	3/3	0.93	Negative		3.38			UD	AD	
10****	70s	Male	2/3	1.16	Negative		8.94	AD	CN	CN		

Numbers in bold denote positive biomarker status.

Abbreviations: AD=Alzheimer disease (dementia), CN=cognitively normal, FTD=frontotemporal dementia, UD=uncertain dementia. *Same case as the “Parietal/precuneus hemorrhagic infarct” case in Table 2. **Same case as the “Left occipital” case in Table 2. ***Same case as the “Left posterior frontal meningioma” case in Table 3. ****Same case as the “Left frontal meningioma” case in Table 3.

Twenty-three participants were assessed at baseline to have cognitive impairment (Table 1.6). Nine of these participants received a clinical assessment of uncertain dementia and two of the nine had a baseline tau-positive visual assessment. Both cases (Case 2 and Case 4) converted to AD dementia

by their first- and second-year follow ups, respectively and were both A β PET positive. Nonetheless, three cases with a tau-negative visual interpretation at baseline (Case 5, Case 7, and Case 8) converted to AD dementia at their two-, two-, and three-year follow ups, respectively, although Case 5 was reassessed to be cognitively normal at their five-year follow up.

Thirteen of the 23 participants with baseline cognitive impairment received a clinical assessment of AD dementia. All 13 participants were A β PET positive (Table 6). Twelve of these participants had tau-positive visual interpretation; the remaining participant (Case 18) was tau PET negative, but at their one-year follow up had their clinical assessment changed to frontotemporal dementia (FTD). Additionally, Case 21 was tau PET positive, but was reassessed to be cognitively normal at their one- and two-year follow ups.

Table 1.6 Cognitively impaired participant follow up

Age	Sex	APOE	Baseline tau PET temporal meta-ROI	Baseline tau PET visual interpretation	Asymmetry	Baseline A β PET (Centiloid)	Yearly follow-up clinical diagnosis				
							1	2	3	4	5
Baseline uncertain dementia											
1	60s	Male	3/4	1.11	Negative	51.0		UD	UD	CN	UD
2	70s	Female	3/4	1.86	Positive	82.7	AD	AD	AD		
3	60s	Female	3/3	1.14	Negative	37.6	CN	CN	CN	CN	CN
4*	70s	Female	3/3	1.31	Positive	72.1	UD	AD	AD	AD	
5	70s	Male	3/4	1.10	Negative	77.9	CN	UD	AD	UD	CN
6	70s	Female	2/3	1.16	Negative	-25.7	UD				
7	80s	Male	2/4	1.04	Negative	9.49	CN	AD			
8	70s	Female	4/4	1.29	Negative	80.1	UD	AD	AD		
9	70s	Male	3/4	1.02	Negative	19.2	CN	CN	CN	CN	
Baseline 0.5 in memory only											
10	80s	Male	3/3	1.07	Negative	12.2	CN	CN			
Baseline AD dementia											
11	70s	Female	3/4	1.57	Positive	54.7	AD	AD			
12	60s	Male	3/3	2.43	Positive	85.7					
13	70s	Female	3/4	2.08	Positive	60.1	AD	AD	AD	AD	
14	80s	Male	3/3	1.46	Positive	121	AD	AD			
15	80s	Male	3/4	1.35	Positive	87.5	AD	AD	AD	AD	
16	70s	Female	4/4	1.58	Positive	145	AD	AD			
17	70s	Female	3/4	1.52	Positive	97.2	AD				
18	70s	Female	3/4	1.18	Negative	62.8	FTD				
19	70s	Male	3/4	1.40	Positive	134	AD	AD	AD	AD	
20	80s	Male	3/4	1.51	Positive	138	AD	AD			
21	80s	Female	3/3	1.41	Positive	106	CN	CN			
22	70s	Female	3/4	1.48	Positive	55.9	AD	AD			
23	50s	Male	3/3	2.01	Positive	145					

Numbers in bold denote positive biomarker status.

Abbreviations: AD=Alzheimer disease (dementia), CN=cognitively normal, FTD=frontotemporal dementia, UD=uncertain dementia. *Same case as the "Right occipital" case in Table 2.

1.5 Conclusions

^{18}F -flortaucipir PET visual interpretation was found to be consistent between readers in this study ($n=189/189$, 100%, $\kappa=1$) and highly consistent with SUVR quantification ($n=186/189$, 98.4%, $\kappa=0.910$), suggesting these two approaches to determining tau PET positivity give similar results despite their different methodologies. However, three participants had discordant visual interpretations and SUVRs, likely due to a hemorrhagic infarct with elevated radiotracer uptake, an atypical, occipital-predominant presentation of AD NFT deposition, and a highly lateralized presentation of AD NFT deposition, respectively. These cases suggest the need for MR imaging to accompany ^{18}F -flortaucipir PET visual interpretation, and the need to consider regions outside the temporal meta-ROI for SUVR quantification.

Among non-AD sources of ^{18}F -flortaucipir uptake, the most studied is off-target binding in the choroid plexus, striatum, brainstem, and bone/meninges [24,25]. In this study, off-target binding did not mimic the appearance of the AD tau pattern when assessed by visual readers, nor did it cause any tau PET temporal meta-ROI SUVR to be falsely positive when compared to visual interpretation. However, we observed two other sources of off-target binding that were not mentioned in the manufacturer's guidelines for ^{18}F -flortaucipir PET visual interpretation and which can potentially confound tau PET interpretations: hemorrhagic infarcts and meningiomas. The hemorrhagic infarct case was the case previously described as having a tau-positive visual interpretation and a tau-negative SUVR quantification. The two meningioma cases demonstrated elevated levels of radiotracer uptake in the frontal lobe, which is immaterial when assessing tau PET positivity by visual interpretation, but meningiomas in the posterolateral temporal, occipital, or parietal/precuneus regions might plausibly interfere with visual interpretation and SUVR quantification.

^{18}F -flortaucipir PET visual interpretation was found to be moderately consistent with CSF p-tau181 ($n=124/144$, 86.1%, $\kappa=0.526$). Most discordant cases ($n=18/20$) are amyloid-positive and CSF p-tau181 positive, but tau-negative on visual interpretation. This suggests that the discordance between ^{18}F -flortaucipir PET and CSF p-tau181 may be attributed to participants with early changes in AD pathophysiology. Moloney and colleagues have found in an autopsy study that p-tau181, 205, 217, and 231 fluid biomarker sites are present in the early stages of NFT maturity [26]. Wennström and colleagues have found that p-tau217 can be found within NFTs and neuropil threads along with p-tau181, 231, 202, 202/205, and 369/404, and that p-tau217 area fraction correlated with antemortem plasma p-tau217 in individuals with confirmed A β plaque pathology [27]. Furthermore, plasma p-tau and CSF p-tau have been shown to be strongly correlated [28–30]. Taken together, these findings suggest a possibility that CSF p-tau181 is tracking changes in AD pathophysiology that occur earlier than the more advanced stages of NFT aggregation that ^{18}F -flortaucipir PET may be more sensitive to.

When interpreting tau PET visual interpretation alongside clinical diagnosis after the study (both visual interpretation and clinical diagnosis were performed independently) a few relationships between the two kinds of AD diagnoses were remarkable. First, a baseline tau-positive visual interpretation in participants who were cognitively normal at baseline did not reliably predict conversion to AD dementia at follow up. If anything, tau PET positivity in cognitively normal participants was more likely to be either a sign of atypical AD, of related dementias (vascular dementia or FTD), or of resilience to AD dementia. Second, a baseline tau-negative visual interpretation in participants who were cognitively normal at baseline did not rule out conversion to AD dementia at follow up. Four cases were found to demonstrate conversion to AD dementia at follow up under these circumstances, although two of these were later reassessed to be cognitively

normal. Third, baseline tau PET positivity in cognitively impaired participants did not guarantee a diagnosis of AD dementia at follow up: one participant was assessed to be cognitively normal at follow up even under these circumstances and another was reassessed to have FTD. Finally, baseline tau PET negativity in cognitively impaired participants cannot be used to rule out conversion to AD dementia at follow up: three such participants converted to AD dementia at their follow up visits, respectively, although one was reassessed to be cognitively normal at a later date.

A bias of the current study lies in the inclusion of cognitively normal participants. In a clinical setting, ^{18}F -flortaucipir PET is indicated for use in patients with cognitive impairment. Two of the three cases discordant between visual interpretation and SUVR quantification in this study were from cognitively normal participants and would not warrant the use of ^{18}F -flortaucipir visual interpretation in a clinical setting to begin with. Six of the 20 cases discordant between visual interpretation and CSF p-tau181 quantification were from cognitively normal participants and also would not warrant the use of ^{18}F -flortaucipir visual interpretation in a clinical setting. Furthermore, the inclusion of cognitively normal participants, who represent the majority of the cases studied, also introduces a negative case bias, as they also represent a majority of the tau PET negative cases. Since most of these cases have tau PET SUVRs much lower than the SUVR positivity threshold, the agreement between visual interpretation and SUVRs is higher in the current study compared to a more challenging study comparing exclusively borderline cases. Nonetheless, exploring tau positivity in cognitively normal participants in this study identified individuals who have atypical AD tau and clinical progression.

The current study is focused on ^{18}F -flortaucipir PET, and its conclusions do not necessarily apply to other tau PET radiotracers, which may have their own distinctive characteristics regarding

off-target binding and sensitivity, which need to be accounted for on a tracer-by-tracer basis in studies of visual interpretation guidelines [31].

Future studies may also explore the discordances between tau PET visual interpretation and tau PET SUVR more thoroughly by investigating those participants with questionable or very mild dementia. Future studies may also explore the consequences of using regions of interest beyond the temporal meta-ROI used in the current study, such as the MUBADA [32]. These alternative ROIs may be appropriate for increasing concordance between visual interpretation and SUVR quantification, especially if crucial differences between the two lie in elevated radiotracer uptake outside the temporal meta-ROI. That said, the most direct way of harmonizing visual interpretation and SUVR quantification may be to construct an entirely new ROI for SUVR quantification that covers the critical regions in visual interpretation (posterolateral temporal, occipital, and parietal/precuneus regions) and develop a quantification method sensitive to contiguous uptake within this ROI.

In conclusion, ^{18}F -flortaucipir PET visual interpretation can identify atypical AD NFT deposition that may be missed by SUVR quantification depending upon the regions of interest used. However, while the manufacturer's guidelines for ^{18}F -flortaucipir PET visual interpretation address non-AD sources of uptake such as off-target binding, they do not address other non-AD sources of uptake such as hemorrhagic infarcts and meningiomas. Temporal meta-ROI SUVR was highly concordant with visual interpretation for the cohort considered in this study. However, SUVR analyses could not detect lateralized occipital-predominant AD NFT deposition because the occipital lobe falls outside the temporal meta-ROI. CSF p-tau181 concentration was moderately concordant with visual interpretation and enabled detection of early changes in AD pathophysiology associated with tau hyperphosphorylation. However, these changes cannot be seen

on PET. Finally, a positive visual interpretation did not make a follow up diagnosis of AD dementia inevitable, and a negative visual interpretation did not exclude the possibility of a follow up diagnosis of AD dementia. Additional work is needed to understand how multiple AD PET and CSF biomarkers might conceivably be used in tandem in a clinical setting alongside AD clinical evaluation in order to correctly diagnose and treat all individuals, not just those who demonstrate AD biomarker and clinical findings concordant with group-level trends.

Chapter 2: Ante- and postmortem tau in **autosomal dominant and late-onset** **Alzheimer disease**

2.1 Abstract

Antemortem tau positron emission tomography imaging suggests elevated tau pathology in autosomal dominant versus late-onset Alzheimer disease at equivalent clinical stages, but does not implicate the specific tau pathologies responsible. Here we made stereological measurements of tau neurofibrillary tangles, neuritic plaques, and neuropil threads and found compared to late-onset Alzheimer disease, autosomal dominant Alzheimer disease showed even greater tangle and thread burdens. Regional tau burden resembled that observed in tau imaging of a separate cohort at earlier clinical stages. Finally, our results suggest tau imaging measures total tau burden in Alzheimer disease, composed predominantly of tangle and thread pathology.

2.2 Introduction

Antemortem tau positron emission tomography (PET) imaging suggests elevated tau pathology in autosomal dominant (ADAD) versus late-onset Alzheimer disease (LOAD) at equivalent clinical stages. Compared to LOAD, ADAD has shown elevated ^{18}F -flortaucipir [33] radioligand binding in prefrontal, premotor, and inferior parietal cortices [34], as well as precuneus and lateral parietal cortices [35]. However, PET imaging does not implicate specific tau pathologies responsible. Previous work quantitatively comparing AD tau pathology with PET imaging has typically been performed in a single individual [36,37], and it is not known whether these results generalize, given the disease heterogeneity of both ADAD [38] and LOAD [39]. To investigate which tau pathologies contribute to elevated ^{18}F -flortaucipir binding in ADAD versus LOAD cohorts, we

made stereological measurements of three major features of AD tau pathology: neurofibrillary tangles, neuritic plaques, and neuropil threads.

2.3 Methods

Protocols for the study have received prior approval by the local Institutional Review Board of each Dominantly Inherited Alzheimer Network site. Informed consent was obtained from each participant.

Cases selected for postmortem study were participants in the Dominantly Inherited Alzheimer Network ($n=7$) or in studies directed by the Knight Alzheimer Disease Research Center ($n=10$) (Table 2.1). These individuals met the inclusion criteria of high AD neuropathological change [40] without comorbid neurodegenerative or vascular disease.

Table 2.1 Cohort demographics

	Neuropathology cohort		Imaging cohort	
	LOAD	ADAD	LOAD	ADAD
Number	10	7	35	14
Age at visit, years (SD)			74.9 (6.75)	50 (12.5)
Age at onset, years (SD)	63.1 (9.83)	38.4 (4.65)		48.3 (0.83)*
Age at death, years (SD)	73.4 (8.29)	44.9 (7.47)		
Female (%)	6 (60%)	4 (57.1%)	19 (54.3%)	8 (57.1%)
MMSE at visit, score (SD)			25.3 (3.88)	21.9 (6.40)
CDR at visit, score (0/0.5/1/2/3)			0.657 (0/26/8/1/0)	0.714 (0/12/1/0/1)
CDR at death, score (0/0.5/1/2/3)	2.75 (0/0/1/0/7)	3 (0/0/0/0/6)		
<i>APOE</i> ϵ 4 (%)	7/9 (77.8%)	1/7 (14.3%)	22/34 (64.7%)	4/14 (28.6%)
Family Mutation <i>APP/PSEN1/PSEN2</i>		0/7/0		1/12/1
A β plaque score (A0/1/2/3)	3 (0/0/0/10)	3 (0/0/0/7)		
NFT stage (B0/1/2/3)	3 (0/0/0/10)	3 (0/0/0/7)		
Neuritic plaque score (C0/1/2/3)	2.9 (0/0/1/9)	3 (0/0/0/7)		

*Includes estimated age at onset using expected years to symptom onset (EYO).

Neuropathological assessment of cases involved expert evaluation of histology slides representing 16 brain areas from the left side of each brain [41]. Stereology focused on tissues sampled in the coronal plane, including the frontal lobe (middle frontal gyrus), temporal lobe (superior and middle temporal gyri), parietal lobe (inferior parietal lobe including angular gyrus), occipital lobe (calcarine sulcus and peristriate cortex), parahippocampal gyrus, and hippocampal subfield CA1 (both sampled at the level of the lateral geniculate nucleus). From these regions, stereological

measurements of PHF-1 immunostained tangles, plaques, and threads were made using the Area Fraction Fractionator (MBF Bioscience).

In a separate cohort (ADAD $n=14$, LOAD $n=35$), antemortem ^{18}F -flortaucipir PET was quantified using regional standardized uptake value ratios (SUVRs) [42]. These individuals met the inclusion criteria of having a Clinical Dementia Rating (CDR®) [43] greater than 0; individuals with LOAD additionally had positive amyloid PET imaging [44]. Regional SUVRs of interest were defined by FreeSurfer [45] regions best corresponding to neuropathology regions: caudal middle frontal cortex, middle temporal cortex, inferior parietal cortex, pericalcarine cortex, parahippocampal cortex, and hippocampus.

Regional differences across and within ADAD and LOAD in neuropathology and imaging were assessed using the Kruskal-Wallis test. Post hoc Wilcoxon rank-sum tests were performed with Bonferroni-Holm multiple comparisons correction to assess which regions showed elevated tau burden in ADAD versus LOAD.

2.4 Results

Tangle, plaque, thread burden, and SUVR showed statistically significant regional differences across ADAD and LOAD. Only tangle burden and SUVR showed significant regional differences within ADAD and LOAD as well (Figure 2.1).

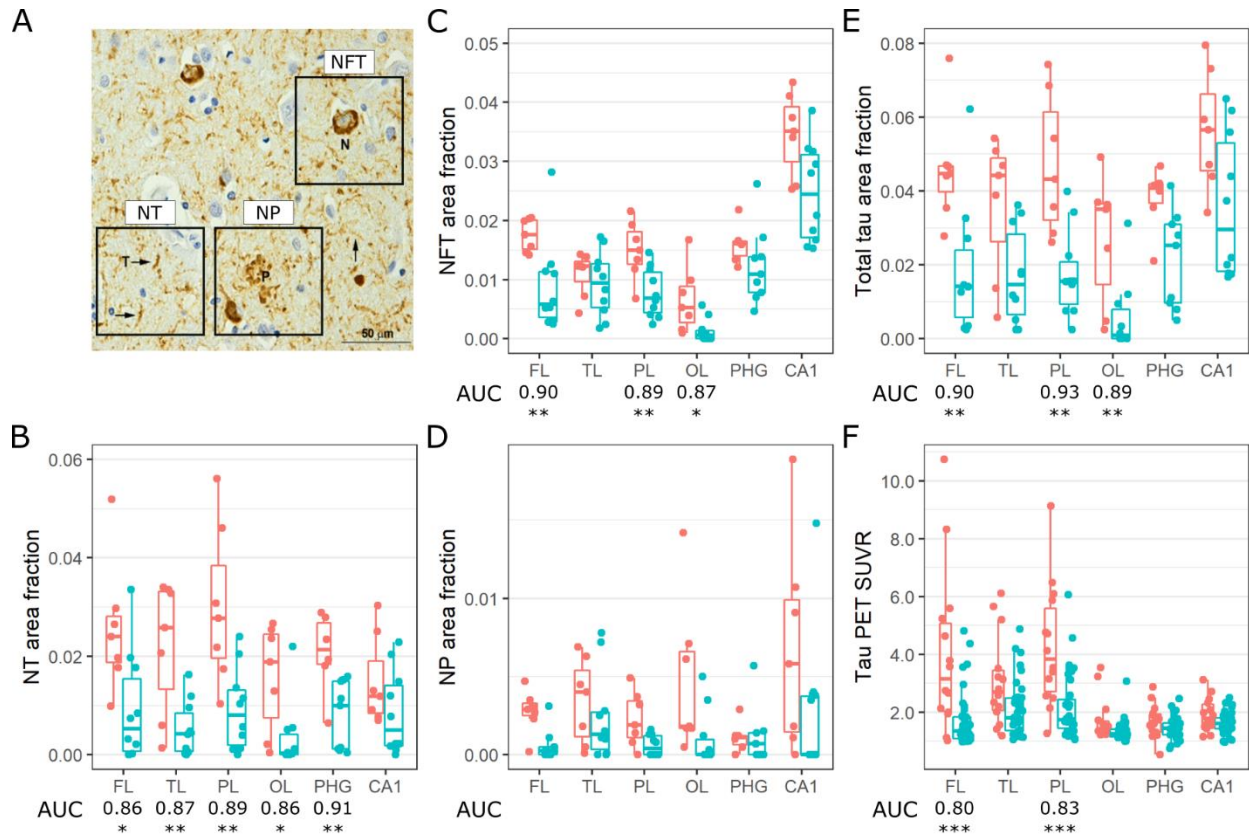


Figure 2.1 (A) Exemplar PHF-1 immunostained neuropil threads (NT), neurofibrillary tangles (NFT), and neuritic plaques (NP). (B) Regional NT burden in the frontal lobe (FL), temporal lobe (TL), parietal lobe (PL), occipital lobe (OL), parahippocampal gyrus (PHG), and hippocampal subfield CA1 in ADAD and LOAD. (C) Regional NFT burden. (D) Regional NP burden. (E) Regional total tau (NT+NFT+NP) burden. (F) Regional 18F-flortaucipir PET imaging SUVRs. Asterisks denote p-values < 0.05 (*), 0.01 (**), and 0.001 (***) for regionwise Wilcoxon rank-sum tests between ADAD and LOAD. Only area under the curves (AUCs, the probability that a randomly selected ADAD individual has a higher regional tau burden than a randomly selected LOAD individual) that are statistically significant after Bonferroni-Holm multiple comparisons correction are displayed.

Compared to LOAD, tangle burden in ADAD was significantly elevated outside the temporal lobe. Patterns of regional tangle burden resembled those of regional SUVRs. However, while CA1 is highest in median tangle burden, the hippocampus has only the third and fourth highest median SUVR in ADAD and LOAD, respectively (Figures 2.1C and 2.1F).

Neuritic plaque burden was elevated in ADAD, but no post hoc test reached statistical significance after multiple comparisons correction. Thread burden was elevated outside CA1 (Figures 2.1B and 2.1D).

2.5 Discussion

Antemortem tau PET SUVRs and postmortem tangle burden in frontal and parietal regions were elevated in ADAD versus LOAD. This concordance appears robust at the group level, even though antemortem imaging and postmortem neuropathology were assessed in different cohorts, roughly representing early and late clinical stages of AD, respectively (Table 2.1). Additionally, the ADAD neuropathology cohort demonstrates an earlier age of onset than the ADAD imaging cohort, suggesting more aggressive forms of AD pathology in the former.

Given differences in clinical stage and age of onset, it is not surprising there are also discordant findings. First, in ADAD, tangle burden is elevated in the occipital lobe relative to LOAD, but SUVR is not. Second, medial temporal lobe regions show some of the highest regional tangle burden in the neuropathology, but not imaging, cohort. There are several potential explanations. Firstly, tau burden may be particularly modest in the medial temporal lobe at early symptomatic stages of AD, but increase substantially by end stage. Secondly, PET imaging may have difficulty resolving the tau burden of small brain structures compared to histopathological assessment. Finally, some individuals in the imaging cohort may have subtle neuropathological comorbidities that contribute to cognitive impairment, qualifying an amyloid PET positive case with low AD neuropathological change (transentorhinal versus limbic stages of tau pathology) for inclusion in this study.

More discordances between imaging and neuropathology come from patterns of regional neuritic plaque and thread burden. Plaque burden was elevated in ADAD, though no post hoc test reached statistical significance, and thread burden was elevated outside CA1. Ringman *et al.* [46] found statistically significant elevation of plaque burden in a larger cohort (ADAD $n=60$, LOAD $n=120$), but used a semi-quantitative global score for each individual. We could not find any

published studies comparing levels of neuropil threads between ADAD and LOAD. We also attribute these discordant findings to differences in clinical stage between neuropathology and imaging cohorts.

Comparing frontal, temporal, and parietal lobe values suggests tau PET SUVRs may correspond best to total tau burden (summed contributions from tangles, plaques, and threads). Similarly, Smith *et al.* [36] found regional SUVRs correlated best with regional total tau burdens in a single individual with ADAD. However, that study also found threads outnumbered tangles in every studied brain region; we found no significant statistical dominance of thread over tangle burden in any region in either ADAD or LOAD.

Given our findings, we can make two conservative claims. First, although tau PET did not assess individuals in late stages of AD, and our neuropathologic assessments focused on very late stages, the regional pattern of elevated tau radioligand binding is largely concordant with the regional pattern of elevated postmortem total tau burden in ADAD versus LOAD. This suggests regional differences in tau pathology between ADAD and LOAD are consistent throughout their symptomatic stages. We propose that tau PET did not identify the relatively high tau burdens seen in the neuropathological assessment of CA1 and the parahippocampal gyrus because, at the level of the lateral geniculate nucleus, these areas develop far more robust tauopathy only in late stages of AD neuropathological change [47,48], that are more likely to be associated with a terminal Clinical Dementia Rating of 3 than 0.5 or 1. In contrast, the entire hippocampus was assessed in tau PET imaging, which may explain some of the discordance in this comparison.

Second, like tangle burden, thread burden is elevated in ADAD versus LOAD, and across more brain regions, while plaque burden is elevated to a lesser extent. A possible explanation for

greater tangle and thread burden in ADAD than LOAD might be that LOAD is often a multifactorial process, with cerebral small vessel disease, TDP-43, and other co-pathologies contributing to the clinicopathological phenotype such that less AD neuropathologic change is needed to reach similar states of dementia severity. That said, enhancement of tangle and thread burden in ADAD compared to LOAD without an equally strong enhancement of plaque burden may seem unusual. One explanation suggests tangles and threads are pathophysiologically closely linked, with tangles appearing first, and threads reflecting more severe saturation of neuronal processes by abnormal tau, whereas neuritic plaques develop later,[48] and reflect more focal disturbances that leave remaining neuronal cytosol unperturbed. Another explanation: on sections immunostained for tau, within areas of very dense threads, plaques are occasionally difficult to discern, and might be undercounted.

We note the limitations to this study. First, no individuals in our neuropathology cohort had undergone antemortem tau PET, precluding direct imaging-neuropathology comparisons. Second, regions included in the neuropathology portion of this study were limited in number and not perfectly correspondent to those from tau PET. Third, most ADAD individuals who came to autopsy were at the end stage of disease. Finally, there is a difference in age of AD symptom onset between the imaging and neuropathology cohorts. Earlier ages of onset appear to be correlated with higher cortical tau PET signal [49–51] and thus there may be a mixed contribution of mutation and early age of onset to the tau PET imaging of the ADAD cohort. From the current study, the tau pathologies responsible for differences observed in tau PET between ADAD versus LOAD were revealed to be predominantly neurofibrillary tangles and neuropil threads. However, our current findings cannot address how temporal progression of tau pathology in ADAD differs from that in LOAD (hypothesized to begin in the brain stem [52,53] and suspected to share early-stage

distribution in the medial temporal lobe with primary age-related tauopathy [54]). Future work can investigate the temporal progression of AD tau pathology more broadly by studying the relationship between earlier/later ages of AD symptom onset and tau pathology. One possibility is to introduce an early-onset sporadic AD cohort to help disentangle the contributions of an earlier age of onset from the specific mutations that define the ADAD cohort.

Chapter 3: Comparing amyloid- β plaque burden with antemortem PiB PET in autosomal dominant and late-onset Alzheimer disease

3.1 Abstract

Pittsburgh compound B (PiB) radiotracer for positron emission tomography (PET) imaging can bind to different types of amyloid- β plaques and blood vessels (cerebral amyloid angiopathy). However, the relative contributions of different plaque subtypes (diffuse versus cored/compact) to *in vivo* PiB PET signal on a region-by-region basis is incompletely understood. Of particular interest is whether the same staging schemes for summarizing amyloid- β burden are appropriate for both late-onset and autosomal dominant forms of Alzheimer disease (LOAD and ADAD). Here we compared antemortem PiB PET with follow-up postmortem estimation of amyloid- β burden using stereologic methods to estimate the relative area fraction of diffuse and cored/compact amyloid- β plaques across 16 brain regions in 15 individuals with ADAD and 14 individuals with LOAD. In ADAD, we found that PiB PET correlated with diffuse plaques in the frontal, parietal, temporal, and striatal regions commonly used to summarize amyloid- β burden in PiB PET, and correlated with both diffuse and cored/compact plaques in the occipital lobe and parahippocampal gyrus. In LOAD, we found that PiB PET correlated with both diffuse and cored/compact plaques in the anterior cingulate, frontal lobe (middle frontal gyrus), and parietal lobe, and showed additional correlations with diffuse plaque in the amygdala and occipital lobe, and with cored/compact plaque in the temporal lobe. Thus, commonly used PiB PET summary regions predominantly reflect diffuse plaque burden in ADAD and a mixture of diffuse and cored/compact

plaque burden in LOAD. In direct comparisons of ADAD and LOAD, postmortem stereology identified much greater mean amyloid- β plaque burdens in ADAD versus LOAD across almost all brain regions studied. However, standard PiB PET did not recapitulate these stereologic findings, likely due to non-trivial amyloid- β plaque burdens in ADAD within the cerebellum and brainstem – commonly used reference regions in PiB PET. Our findings suggest that PiB PET summary regions correlate with amyloid- β plaque burden in both ADAD and LOAD; however, they might not be reliable in direct comparisons of regional amyloid- β plaque burden between the two forms of AD.

3.2 Introduction

Pittsburgh compound B (PiB) positron emission tomography (PET) is a powerful diagnostic tool that enables *in vivo* imaging of insoluble amyloid- β throughout the human brain at near-millimeter resolution [55]. This offers an opportunity to detect and monitor changes in amyloid- β plaque deposition during the course of Alzheimer disease (AD) clinical trials. However, some important characteristics of PiB, as it is applied *in vivo*, remain incompletely understood. Although PiB is known to bind to amyloid- β peptides associated with both diffuse and amyloid- β cored/compact plaques [56], the relative contributions of these plaque subtypes to *in vivo* PiB PET signal on a region-by-region basis remains incompletely understood. The distinction is of interest from a clinicopathological perspective, as cored/compact plaques are more likely than their diffuse counterparts to be neuritic [57–59]. Nonetheless, diffuse plaques are associated with deleterious effects on cognitive performance and are unlikely to be benign [60]. Additionally, as AD clinical trials involve both late-onset AD (LOAD) and autosomal dominant AD (ADAD) populations, there is a need to understand whether the staging schemes for summarizing amyloid- β burden in the former are appropriate for investigating the severity of β -amyloidosis in the latter. In contrast

to individuals with LOAD, those with ADAD carry a mutation in one of three genes – *APP*, *PSEN1*, or *PSEN2* – and develop AD with a relatively predictable time of clinical onset. This defining characteristic of ADAD allows investigators to assess the extent to which candidate drugs are preventing or delaying the onset of AD dementia, but this underlying difference in disease etiology may also lead to differences in the characteristics of β -amyloidosis between LOAD and ADAD populations [46,61].

Commonly, postmortem staging of amyloid- β deposition in AD involves assessment of Thal phase [62] and the Consortium to Establish a Registry for Alzheimer disease (CERAD) neuritic plaque score [63], which have recently been incorporated, along with Braak neurofibrillary tangle (NFT) stage [48], into the ABC score [64]. Although very useful for some purposes, these systems only describe the general anatomic pattern of amyloid- β plaque deposition within the central nervous system (Thal phase) and the semi-quantitative maximal density of neuritic plaques within a prescribed, limited set of cortical regions (CERAD). For antemortem staging of amyloid- β deposition in AD, a volume of interest comprised of frontal, parietal, temporal, and striatal regions is typically constructed to focus on brain regions of greater relevance to AD disease pathology [42,65]; however, these regions were derived by comparing groups of healthy individuals and individuals with LOAD. Thus, from both neuropathologic and imaging perspectives, it is unclear whether these staging schemes for amyloid- β burden are equally applicable to both ADAD and LOAD.

Therefore, to investigate more fully the qualities of β -amyloidosis in these two forms of AD, we examined two cohorts, representing ADAD and LOAD, using antemortem PiB PET imaging and unbiased stereologic methods to quantify postmortem amyloid- β burden contributed by diffuse and cored/compact plaques in 16 brain regions of interest, including seven summary

regions typically of interest in PiB PET imaging of AD (frontal, parietal, and temporal lobes, anterior and posterior regions of the cingulate gyrus, caudate, and putamen), seven other regions typically of interest for the evaluation of various other AD and non-AD pathologic features (occipital lobe, amygdala, hippocampus, parahippocampal gyrus, entorhinal cortex, globus pallidus, and thalamus), and two reference regions typically of interest in PiB PET imaging of AD (cerebellum and brainstem). We then compared these findings to corresponding antemortem PiB PET, to determine whether the relationship between histologic and PET assessments of amyloid- β pathology is influenced by plaque type, anatomic region, and form of AD. This study provides insights into the extent to which plaque subtypes are represented in typical PiB PET neuroimaging and the extent to which differences in amyloid- β plaque burden between ADAD and LOAD are represented in typical PiB PET. Thus, this study informs how PiB PET might best be applied to evaluate ADAD progression in AD clinical trials, and how amyloid- β clearance might be appropriately monitored in anti-amyloid- β drug trials.

3.3 Materials and methods

3.3.1 Cohort demographics

Participants selected for this histological/radiological comparison study were either enrolled in the Dominantly Inherited Alzheimer Network Observational Study (DIAN-Obs, $n=14$) or in longitudinal observational studies of the Charles F. and Joanne Knight Alzheimer Disease Research Center (Knight ADRC, $n=15$). One participant was enrolled in studies of the Knight ADRC, but had an ADAD mutation; this individual was grouped with participants from the DIAN-Obs to form the ADAD cohort ($n=15$), and the remaining participants from the Knight ADRC formed the LOAD cohort ($n=14$) in the current study (Table 3.1). All participants met the inclusion criteria, having undergone PiB PET prior to death, and having *high* AD neuropathologic change

(ADNC) upon subsequent postmortem examination [40]. Cohort demographics are reported in Table 4.1.

Table 3.1 Cohort demographics

ADAD	Family mutation	APOE	Sex	MMSE	CDR	Clinical cause of death	CDR at death	Age at death	Imaging-autopsy interval (years)	Thal phase	Braak stage	CERAD score	CAA	Final Dx 1	Final Dx 2-4
1	<i>PSEN1</i>	44	M	21	1	Aspiration, pneumonia, AD	3	40-50	0.68	5	6	3	1	ADNC	Glioblastoma
2	<i>PSEN1</i>	23	F	16	1	Probable pneumonia	3	30-40	1.1	5	6	3	1	ADNC	
3	<i>PSEN1</i>	33	M	9	3	Inanition	3	40-50	1	5	6	3	2	ADNC	DLB (neocortical), SVD: CAA (moderate-severe), Art. (mild)
4	<i>PSEN1</i>	34	F	21	1	AD	3	40-50	3.3	5	6	3	3	ADNC	DLB
5	<i>PSEN1</i>	23	F	12	2	Probable pneumonia	3	40-50	2.3	5	6	3	2	ADNC	
6	<i>PSEN1</i>	33	M	10	1	AD, inanition		40-50	1.8	5	6	3	1	ADNC	DLB
7	<i>PSEN1</i>	33	M	13	2	AD, inanition	3	50-60	1.3	5	6	3	1	ADNC	ALB
8	<i>PSEN1</i>	23	F	8	2	Respiratory failure, cardiac arrest, AD	3	40-50	1.5	5	6	3	1	ADNC	MH (BG)
9	<i>PSEN1</i>	34	F	21	0.5	AD	3	30-40	2.5	5	6	3	3	ADNC	
10	<i>PSEN1</i>	33	M	0	3	Heart attack, Inanition	3	60-70	4	5	6	3	1	ADNC	ALB
11	<i>PSEN1</i>	34	F	8	3	AD, inanition	3	40-50	2.3	5	6	3	3	ADNC	ALB
12	<i>PSEN1</i>	33	M	15	1	Aspiration, inanition	3	50-60	2	5	6	3	3	ADNC	CAA
13	<i>PSEN1</i>	33	M	19	1	Brain hemorrhage, inanition	3	50-60	3.4	5	6	3	2	ADNC	ALB
14	<i>APP</i>	44	M	21	2	Pneumonia, inanition	3	60-70	5.6	5	6	3	3	ADNC	ALB
15	<i>PSEN1</i>	33	M	27	0.5	AD	3	30-40	3.3	5	6	3	3	ADNC	
Mean (SD)				15 (7)	1.6 (0.9)		3 (0)	47 (9)	2.4 (1.3)	5 (0)	6 (0)	3 (0)	2 (0.9)		
LOAD	Family mutation	APOE	Sex	MMSE	CDR	Clinical cause of death	CDR at death	Age at death	Imaging-autopsy interval	Thal phase	Braak stage	CERAD score	CAA	Final Dx 1	Final Dx 2-4
1		34	M	30	0.5	UTI, diabetes mellitus, AD contributing	2	80-90	3.7	5	5	3	1	ADNC	SVD: Art. (moderate), LVD: Art. (moderate)
2		33	M	21	1	Lymphoma	2	60-70	3.9	5	6	3	1	ADNC	
3		34	F	20	1	AD	3	80-90	3.8	5	5	3	1	ADNC	
4		34	F	26	0.5	Inanition	3	70-80	3.9	5	5	3	3	ADNC	

5	34	M	12	2	AD	3	70-80	4.7	5	5	3	1	ADNC	
6	34	F	28	0	AD	3	80-90	4.8	5	4	3	1	ADNC	
7	34	M	25	0.5	DLB, UTI, dehydration	3	70-80	3.7	5	5	3	1	ADNC	
8	33	M	22	1		1	80-90	0.3	5	5	3	1	ADNC	
9	34	M	26	0.5	Inanition	3	80-90	3.4	4	5	3	1	ADNC	
10	34	F	25	0.5	Inanition	3	90-100	8.4	4	6	3	2	ADNC	Infarcts (BG, Th)
11	34	M	26	0.5	Inanition	3	90-100	9.6	5	5	3	3	ADNC	ALB, TDP-43 (MTL)
12	34	M	23	0.5	Inanition	3	70-80	4.2	5	5	3	1	ADNC	
13	33	F	25	0.5		2	90-100	6.1	5	5	3	2	ADNC	Infarcts (PL, FL), microinfarct (FL)
14	33	M	23	0.5	AD	3	70-80	4.9	5	6	3	1	ADNC	DLB (olfactory), SVD: Art. (moderate), SVD: CAA (mild)
Mean (SD)			24 (4)	0.7 (0.5)			2.6 (0.6)	83 (9)	4.7 (2.2)		5.1 (0.5)	3 (0)	1.4 (0.8)	

Age at death is reported as an age range to protect the identities of the study participants. Exact ADAD mutations of the *PSEN1* gene are presented in Table A.1 in the interests of better understanding the clinicopathologic variability in this population, but are not linked to the individual-level demographics in this table in order to protect the identities of the study participants. Abbreviations: ADNC (Alzheimer disease neuropathologic change), ALB (amygdala Lewy bodies), Art. (arteriosclerosis), BG (basal ganglia), CAA (cerebral amyloid angiopathy), DLB (dementia with Lewy bodies), Dx (diagnosis), FL (frontal lobe), LVD (large vessel disease), MH (microhemorrhage), MTL (medial temporal lobe), PL (parietal lobe), SAH (subarachnoid hemorrhage), SD (standard deviation), SVD (small vessel disease), Th (thalamus), UTI (urinary tract infection).

To address other questions about PiB PET amyloid staging, a separate extended imaging cohort of 317 DIAN-Obs participants and 734 Knight ADRC participants was selected. These participants met the inclusion criteria of having had a clinical and cognitive assessment within 18 months of a PiB PET scan. Extended imaging cohort demographics are reported in Table 3.3. Protocols for the study have received prior approval by the local Institutional Review Board (IRB) or Ethics Committee of each DIAN site, and by the Washington University IRB for the Knight ADRC. Participants or their caregivers provided written informed consent.

3.3.2 Postmortem neuropathology

Neuropathologic assessment of cases included a systematic evaluation of histologic slides representing 16 areas from the left hemibrain by experienced neuropathologists (authors R.J.P. and N.J.C.) [41]. Following an established protocol, each left hemibrain was sliced after formalin fixation. The supratentorial portion of the cerebral hemisphere was sliced in the coronal plane; the cerebellum, parasagittally; and the brainstem, axially. Sixteen representative brain areas were

sampled: the frontal lobe (middle frontal gyrus); temporal lobe (superior and middle temporal gyri); parietal lobe (inferior parietal cortex including the angular gyrus); occipital lobe (including the calcarine sulcus and parastriate cortex); anterior cingulate gyrus (at the level of the genu of the corpus callosum); posterior cingulate gyrus (including precuneus at the level of the splenium); amygdala; hippocampus, parahippocampal gyrus, and entorhinal cortex (at the level of the lateral geniculate nucleus); caudate, putamen, and globus pallidus (at the level of the anterior commissure); thalamus (including subthalamic nucleus); brainstem (midbrain, pons, medulla oblongata); and cerebellum (with the dentate nucleus). Slide-mounted six-micron-thick sections of formalin-fixed, paraffin-embedded tissue were stained with hematoxylin and eosin (H&E), with a modified Bielschowsky silver impregnation, and by immunohistochemistry (IHC) using antibodies for amyloid- β (10D5, Eli Lilly, Indianapolis, IN, USA), phosphorylated tau (PHF-1, a gift from Dr. Peter Davies), phosphorylated alpha-synuclein (Cell Applications, San Diego, CA, USA), and phosphorylated TAR DNA binding protein of 43 kDa (TDP-43, Cosmo Bio USA, Carlsbad, CA, USA) to detect the histopathological hallmarks of AD as well as those of frequent comorbid pathologies (including non-AD tauopathies, TDP-43 proteinopathies, and α -synucleinopathies). The Area Fraction Fractionator probe in Stereo Investigator 10 (MBF Bioscience, Williston, VT, USA) was used to assess the burden of diffuse and cored/compact amyloid- β using stereologic methods as implemented in a computerized image analysis system. Plaque area fraction was assessed either in the gray matter of cortical gyri or subcortical nuclei. Diffuse amyloid- β plaques were identified by raters (A.Z. and N.S.) to be irregularly-shaped amyloid- β deposits, while cored/compact amyloid- β plaques were identified to be spherically-shaped amyloid- β deposits representing a dense central core (surrounded by a less compact halo of amyloid- β oligomers contributing to the diffuse rather than the compact amyloid- β plaque area

fraction) [66,67]. The degree of agreement among raters in assessing diffuse and cored/compact amyloid- β plaque burden was high (Cohen's $\kappa > 0.8$). When assessing amyloid- β plaque area fraction, raters were blinded to any demographic information regarding the individuals who donated the tissue samples, as well as any information regarding their antemortem PiB PET acquisition.

3.3.3 Antemortem PiB PET imaging

Methods for antemortem PiB PET acquisition, performed in compliance with the DIAN protocol, have been described previously [68,69]. Briefly, participants received an intravenous injection of approximately 15 mCi of [^{11}C]PiB radiotracer [70]. PET images were attenuation compensated with the corresponding CT image, and reconstructed using the ordered subset expectation maximization technique. Data from 40 to 70 minutes post injection were converted to regional standardized uptake value ratios (SUVRs) with the cerebellar gray matter as the standard reference region, with cerebellar white matter and brainstem evaluated as alternative reference regions in later analyses. Regional SUVRs of interest were defined by FreeSurfer [45] version 5.3 regions best corresponding to the areas sampled for neuropathology in a consensus between an experienced neuropathologist and radiologist (authors R.J.P. and T.L.S.B.) [71]. MR images used for FreeSurfer segmentation were also performed in compliance with the DIAN protocol, as described previously [68,69]. Briefly, T1-weighted images (1.1 x 1.1 x 1.2 mm resolution) were acquired for all DIAN-Obs participants on 3T scanners within one year of their PET scan.

Methods for antemortem PiB PET and MRI at the Knight ADRC have been described previously [42,72]. These methods notably differ from the DIAN protocol in the following manner: PET imaging data from the 30 to 60 minutes post injection were converted to regional SUVRs (in

contrast to the 40-70 minute post-injection time window for DIAN) and MR imaging was acquired on either a 1.5 or 3T scanner (in contrast to only 3T scanners for DIAN).

Briefly, brain areas sampled for neuropathologic assessment were matched to FreeSurfer regions on the basis of shared nomenclature and spatial overlap on the left hemisphere (Figure A.1). All data processing steps were performed using the PET Unified Pipeline [42,73], a publicly-available software developed in house.

3.3.4 Statistical analysis

All statistical analyses were performed in R version 3.5.2 “Eggshell Igloo”. Multiple imputation was used in the ADAD (15 participants) and LOAD (14 participants) cohorts to estimate missing observations due to the occasional unavailability of postmortem tissue samples; specifically, 17 tissue samples in the ADAD cohort (out of a possible 240, yielding 7.1% missingness) and 13 tissue samples in the LOAD cohort (out of a possible 224, yielding 5.8% missingness) were unavailable and subsequently estimated by multiple imputation by chained equations using the predictive mean matching method and five imputations [74]. Pearson’s r was used to measure the linear correlation between regional PiB PET SUVR and diffuse and compact plaque area fractions in ADAD and LOAD cohorts. T -values from Welch two sample t -tests were used to determine the extent to which regional PiB PET SUVR and diffuse and compact plaque area fractions differed between ADAD and LOAD cohorts. Area under the receiver operating characteristic curves (AUCs, interpreted as the probability that a randomly selected ADAD/LOAD individual has a higher regional PiB PET SUVR than a randomly selected non-carrier/young healthy control) were used to determine which regions were most frequently elevated in ADAD/LOAD versus young healthy controls. Hierarchical agglomerative clustering was used to visualize similarities in regional PiB PET SUVR distributions across participants (complete-linkage clustering using a

Euclidean distance metric). All test statistics are accompanied by p -values adjusted for false discovery rate (FDR) control by the Benjamini-Hochberg procedure. A FDR of $q=0.05$ was chosen for discussion purposes, but all FDR-adjusted p -values have been reported for transparency [75].

3.4 Results

3.4.1 Cohort demographics

Participants who formed the ADAD cohort in this study ($n=15$) were mostly known *PSEN1* mutation carriers ($n=13$), male ($n=9$), lacking the *APOE4* allele ($n=10$), and died at the average age of 47 from AD with other co-morbidities (Table 3.1). All ADAD participants were Thal phase 5, and Braak NFT stage VI, with “frequent” CERAD neuritic plaque scores.

Participants who formed the LOAD cohort in this study ($n=14$) were mostly male ($n=9$) *APOE4* carriers ($n=10$) who died at the average age of 83 with AD and other co-morbidities. LOAD participants were largely Thal phase 5 (with two borderline Thal phase 4/5 cases), Braak NFT stage V ($n=10$), with “frequent” CERAD neuritic plaque scores.

In addition to the age of death, the major difference to note between the ADAD and LOAD cohorts is that the imaging-autopsy interval in the ADAD cohort is on average less than the imaging-autopsy interval in the LOAD cohort (an average of 2.4 years versus an average of 4.7 years) due to procedural differences between DIAN-Obs and Knight ADRC studies. We address the potential impact of this difference in the Discussion.

In the extended imaging cohort, ADAD participants ($n=317$) were mostly *PSEN1* mutation carriers ($n=131$) or non-carriers/young healthy controls ($n=133$), female ($n=182$), and cognitively normal ($n=251$), lacked the *APOE4* allele ($n=222$), and underwent PiB PET at an average age of 38 (Table 3.3).

LOAD participants ($n=734$) were mostly female ($n=421$) and cognitively normal ($n=615$), lacked the *APOE4* allele ($n=451$), and underwent PiB PET at an average age of 69.

3.4.2 Correlations between PiB PET and stereologic measurements

Regional correlations between PiB PET SUVR and diffuse and compact plaque area fractions in the ADAD and LOAD cohorts are shown in Table 3.2. In the ADAD cohort, PiB PET SUVR was significantly correlated (FDR-adjusted p -value<0.05) with diffuse plaque burden in all PiB PET summary regions except for the putamen, and with both diffuse and cored/compact plaque burden in the occipital lobe and parahippocampal gyrus (reference regions were not assessed in these correlational analyses). In the LOAD cohort, PiB PET SUVR was significantly correlated with both diffuse and cored/compact plaque burdens in the anterior cingulate, frontal lobe, and parietal lobe summary regions, and with cored/compact plaque burden in the temporal lobe summary region. Additionally, PiB PET SUVR was significantly correlated with diffuse plaque burden in the amygdala and occipital lobe.

Table 3.2 Regional correlations between [¹¹C]PiB PET SUVRs and plaque area fractions

ADAD	Diffuse plaque			Compact plaque		
	<i>r</i>	<i>SE</i>	<i>p</i>	<i>r</i>	<i>SE</i>	<i>p</i>
Summary regions						
Anterior cingulate	0.81	0.16	0.0018	0.32	0.26	0.45
Caudate	0.62	0.22	0.018	0.066	0.28	0.87
Frontal lobe	0.63	0.19	0.018	0.31	0.26	0.45
Parietal lobe	0.70	0.20	0.012	0.59	0.22	0.15
Posterior cingulate	0.63	0.22	0.018	0.045	0.28	0.87
Putamen	0.34	0.26	0.21	-0.084	0.28	0.87
Temporal lobe	0.60	0.22	0.021	0.31	0.26	0.45
Other regions						
Amygdala	0.43	0.25	0.11	0.58	0.23	0.053
Entorhinal cortex	0.46	0.25	0.081	0.48	0.24	0.10
Globus pallidus	-0.013	0.28	0.96	0.12	0.28	0.79
Hippocampus	0.29	0.27	0.30	0.56	0.23	0.053
Occipital lobe	0.80	0.17	0.00038	0.65	0.21	0.030
Parahippocampal gyrus	0.64	0.21	0.011	0.65	0.21	0.030
Thalamus	0.48	0.24	0.073	0.059	0.28	0.83
LOAD						
Summary regions						
Anterior cingulate	0.82	0.16	0.00098	0.68	0.21	0.018
Caudate	0.36	0.27	0.25	0.087	0.29	0.77
Frontal lobe	0.72	0.20	0.0080	0.81	0.17	0.0028
Parietal lobe	0.83	0.16	0.00098	0.62	0.23	0.030
Posterior cingulate	0.23	0.28	0.43	0.23	0.28	0.61
Putamen	0.52	0.25	0.077	-0.087	0.29	0.77
Temporal lobe	0.54	0.24	0.077	0.68	0.21	0.018
Other regions						
Amygdala	0.71	0.20	0.016	0.34	0.27	0.32
Entorhinal cortex	0.072	0.29	0.81	-0.44	0.26	0.26
Globus pallidus	0.14	0.29	0.81	0.13	0.29	0.77
Hippocampus	0.081	0.29	0.81	-0.059	0.29	0.84
Occipital lobe	0.77	0.18	0.0090	0.39	0.27	0.29

<i>Parahippocampal gyrus</i>	0.49	0.25	0.14	0.59	0.23	0.18
<i>Thalamus</i>	0.50	0.25	0.14	0.48	0.25	0.26

P-values are adjusted for FDR control by the Benjamini-Hochberg procedure. Abbreviations: SE (standard error).

Table 3.3 Extended imaging cohort demographics

		ADAD	LOAD
Number		317	734
Family mutation	<i>PSEN1</i>	131	
	<i>PSEN2</i>	22	
	<i>APP</i>	31	
	Non-carrier	133	
<i>APOE</i>	22	3	3
	23	28	80
	24	12	18
	33	191	368
	34	78	209
	44	5	42
Sex	M	135	313
	F	182	421
Mean baseline MMSE (SD)		28.8 (8.61)	28.7 (1.86)
Baseline CDR	0	251	615
	0.5	43	98
	1	16	21
	2	5	0
	3	2	0
Mean baseline age (SD)		37.7 (10.7)	68.7 (9.49)

3.4.3 Differences between ADAD and LOAD as measured by PiB PET and stereology

Regional differences in amyloid- β burden (as measured by PiB PET and stereology) between the ADAD and LOAD cohorts are shown in Figure 3.1. Diffuse plaque burden was significantly greater in ADAD versus LOAD in all summary regions except for the parietal lobe, and in all other regions, except for the globus pallidus. Cored/compact plaque burden was also greater in ADAD versus LOAD, though only in the cerebellum and brainstem was this difference significant.

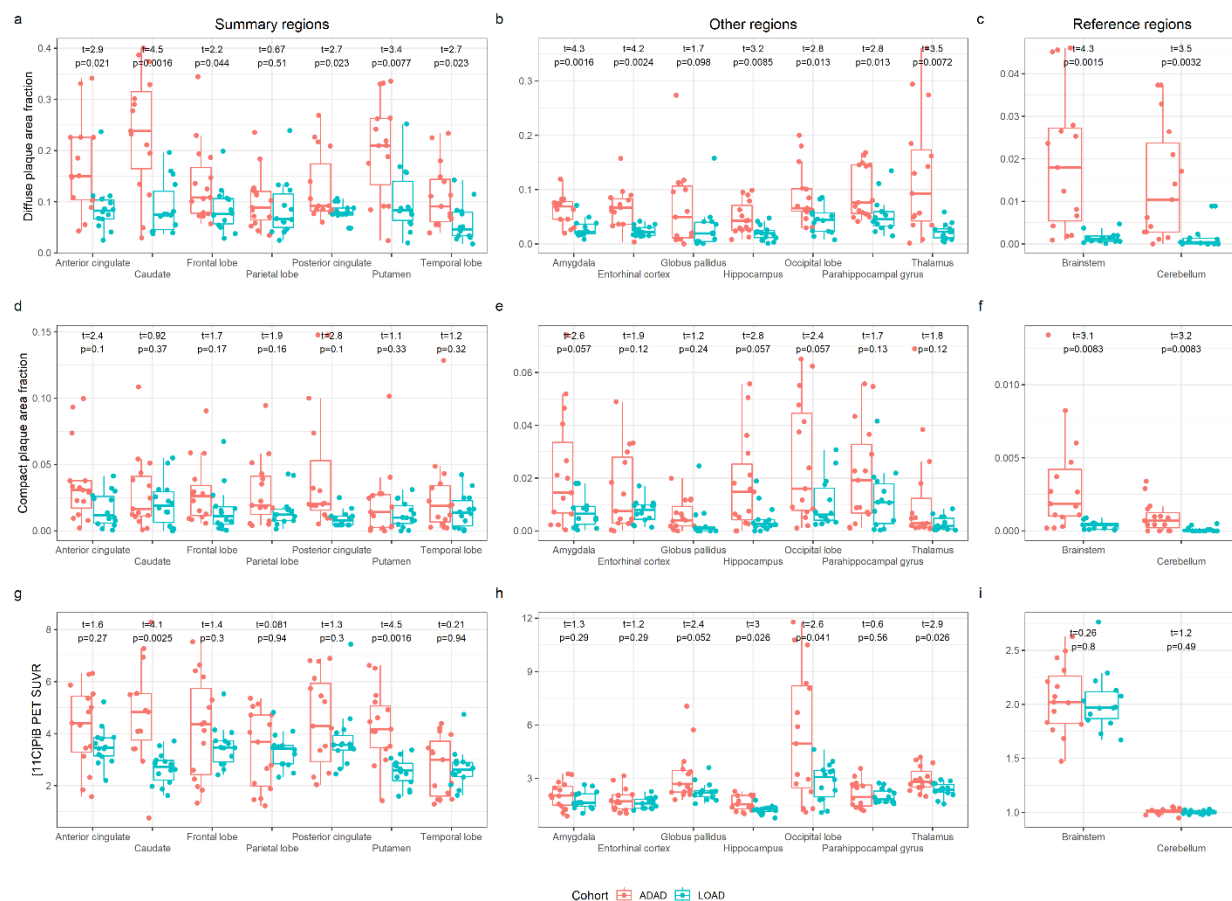


Figure 3.1 Regional differences between ADAD and LOAD as measured by [11C]PiB PET SUVRs and plaque area fractions. Regional differences in diffuse (a, b, c) and compact plaque area fractions (d, e, f) and [11C]PiB PET SUVRs (g, h, i) across summary regions, other regions, and reference regions between ADAD and LOAD. Differences are reported as *t*-values from Welch two sample *t*-tests, accompanied by *p*-values adjusted for FDR control by the Benjamini-Hochberg procedure.

In contrast to stereologic measurements, PiB PET SUVRs (when calculated using the cerebellar gray matter as a reference region) showed no significant differences between ADAD versus LOAD in any summary region examined, with the exceptions of the caudate and the putamen. Additionally, PiB PET SUVR was significantly greater in ADAD versus LOAD in the hippocampus, occipital lobe, and thalamus. Alternative reference regions such as the brainstem, cerebellar white matter, and a combined cerebellar gray and white matter region were also investigated (Figure 3.2). The brainstem as a reference region yielded results similar to those when cerebellar gray matter was used as a reference region (and additionally showed significant

differences in the globus pallidus). When cerebellar white matter was used as a reference region, PiB PET SUVRs showed additional significant differences between ADAD versus LOAD in the anterior cingulate, amygdala, entorhinal cortex, globus pallidus, brainstem, and cerebellum. Use of the combined cerebellar gray and white matter reference region mostly recapitulated the significant differences between ADAD versus LOAD as seen with the cerebellar white matter reference region, with the exception of the amygdala and entorhinal cortex. Nonetheless, no reference region assessed in this study revealed significant between-cohort differences in SUVR in the frontal and temporal lobes, posterior cingulate, and parahippocampal gyrus in a manner concordant with our stereology results. Additionally, the alternative reference regions showed significant between-cohort differences in SUVR in the globus pallidus, which was not seen in stereology.

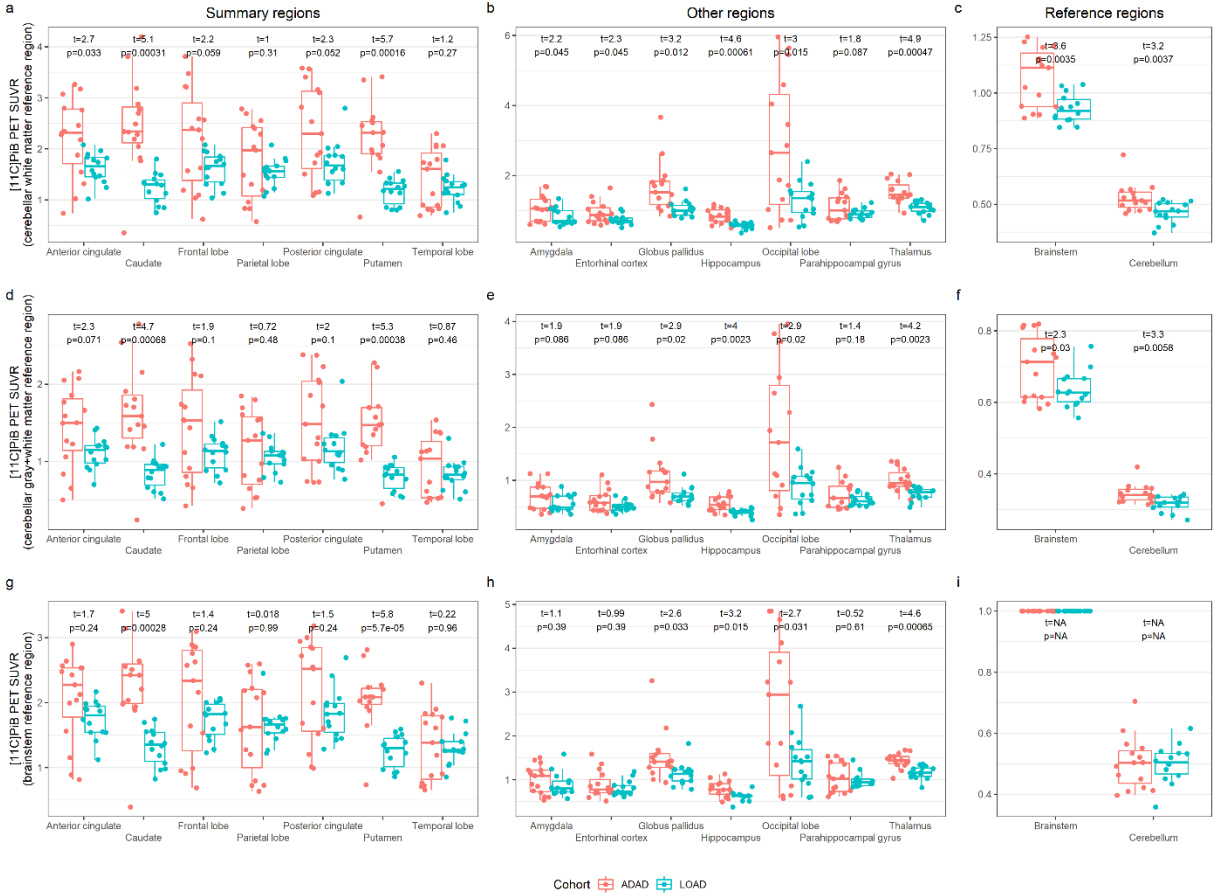


Figure 3.2 Regional differences between ADAD and LOAD as measured by [11C]PiB PET SUVRs while using alternative reference regions. Regional differences in [11C]PiB PET SUVRs when using cerebellar white (a, b, c), cerebellar gray+white (d, e, f), and brainstem reference regions (g, h, i) between ADAD and LOAD. Differences are reported as t -values from Welch two sample t -tests, accompanied by p -values adjusted for FDR control by the Benjamini-Hochberg procedure.

3.4.4 PiB PET staging in ADAD versus LOAD

Regional distributions of PiB PET SUVRs in ADAD versus LOAD are shown in Figure 4.4.

Regional AUC analyses showed that ADAD participants frequently demonstrate elevated PiB PET SUVRs compared to non-carriers/young healthy controls across all brain regions, with several medial temporal lobe regions being the least frequently elevated, namely the amygdala, hippocampus, and entorhinal cortex (Figure 3.3a). In contrast, LOAD participants most frequently demonstrate elevated PiB PET SUVRs compared to non-carriers/young healthy controls across several temporal lobe regions, namely the middle temporal, inferior temporal, and fusiform cortices (Figure 3.3b). In a hierarchical agglomerative clustering dendrogram of ADAD cases,

caudate and putamen PiB PET SUVRs cluster with cortical SUVRs such as those of the occipital lobe, frontal lobe, and the anterior and posterior cingulate (Figure 3.3c). In contrast, in LOAD, caudate and putamen SUVRs cluster with medial temporal lobe SUVRs such as those of the parahippocampal gyrus, entorhinal cortex, amygdala, and hippocampus rather than frontal and cingulate cortex SUVRs (Figure 3.3d).

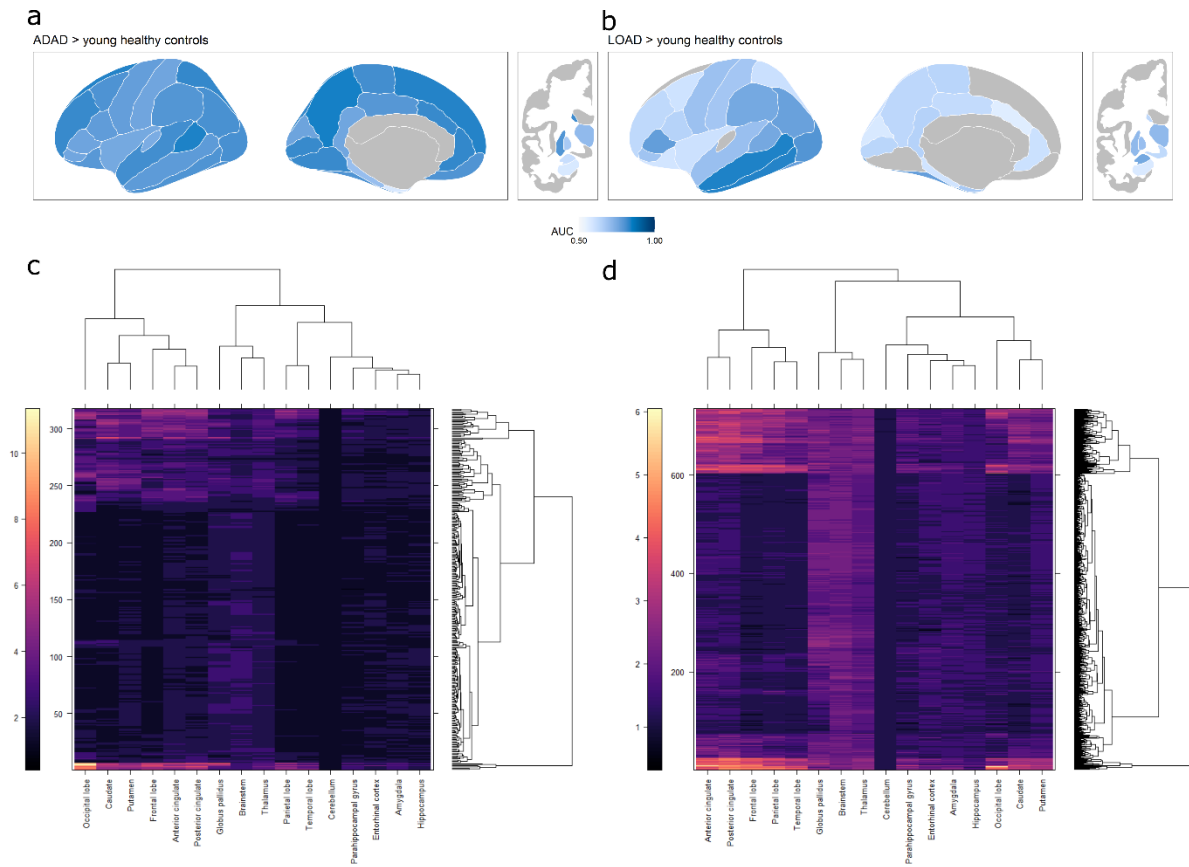


Figure 3.3 Regional distributions of PiB PET SUVRs in ADAD and LOAD. Regional PiB PET SUVRs in ADAD and LOAD. **a** Regional area under the receiver operating characteristic curves for ADAD versus young healthy controls (AUC, the probability that a randomly selected ADAD participant has a higher regional PiB PET SUVR than a randomly selected young healthy control). **b** Regional AUCs for LOAD versus young healthy controls. **c** Heatmap and dendrograms of ADAD participants after hierarchical agglomerative clustering. **d** Heatmap and dendrograms of LOAD participants after hierarchical agglomerative clustering.

3.5 Discussion

Evidence suggests that the primary substrate for PiB retention (and likely that of all PET amyloid- β radiotracers) is fibrillar amyloid- β [76]. Fibrillar amyloid- β is present in both diffuse and cored/compact plaques – although the density is probably much greater in the latter [77]. Therefore, *in vivo* PiB retention cannot distinguish between diffuse and cored/compact deposits of fibrillar amyloid- β . However, the total PiB signal will be primarily driven by the most abundant form of fibrillar amyloid- β , whether in diffuse or cored/compact plaques. To determine which form of plaque (diffuse or cored/compact) is most associated with the *in vivo* PiB PET signal, postmortem-to-*in vivo* correlative studies must be performed. In this study, we compared the correlation of *in vivo* PiB PET retention with postmortem analyses of diffuse and cored/compact plaques in ADAD and LOAD to determine the major contributor to the *in vivo* PiB PET signal in these different forms of AD. From correlational analyses, PiB PET SUVRs in AD summary regions appear to reflect predominantly diffuse plaque burden in ADAD, and a mixture of diffuse and cored/compact plaque burden in LOAD. Outside of these summary regions, PiB PET SUVRs seem to correlate with both diffuse and cored/cored compact plaque burden in the occipital lobe and parahippocampal gyrus in ADAD, and with diffuse plaque burden in the occipital lobe and amygdala in LOAD. These differences suggest that the two forms of AD may require different β -amyloidosis staging schemes to interpret findings from PiB PET. Furthermore, the greater variability of plaque burden observed among ADAD cases additionally suggests that a staging scheme for ADAD might require adjustment for other factors, such as, perhaps, genetic subtype. Nonetheless, some caution is warranted: the presence of cored/compact plaques in several of the aforementioned brain regions is a sign of advanced disease which, in turn, is associated with altered blood flow. Changes in blood flow associated with advanced AD may alter PiB pharmacokinetics

and cause nonspecific retention in affected brain areas [78]; such pathophysiologic changes may be partly responsible for the above observations.

Postmortem stereologic measurements of diffuse and cored/compact plaque burden are significantly greater in ADAD versus LOAD across the brain, yet standard antemortem PiB PET in the same individuals captured significant differences mostly in subcortical regions (specifically the caudate, putamen, and thalamus, as well as the hippocampus and occipital lobe) when using either the cerebellar gray matter or brainstem as reference regions. One possible explanation for the lack of significant differences in cortical amyloid- β between the two cohorts as measured by PiB PET is offered by our stereology results; the cerebellum and brainstem – both commonly used as reference regions in LOAD studies due to their relatively low PiB PET signal in LOAD cohorts – have non-trivial amyloid- β plaque burdens in the ADAD cohort. These circumstances would tend to depress regional PiB PET SUVRs in those ADAD cases with substantial cerebellar and/or brainstem amyloid- β deposits and, thus, selectively reduce the mean SUVR of the ADAD cohort, relative to that of the LOAD cohort. Importantly, this observation suggests that cerebellar gray matter and brainstem may not be appropriate reference regions for evaluating amyloid- β burden with PiB PET in many cases of ADAD. An alternative reference region such as the cerebellar white matter was also evaluated in this study, though using the cerebellar white matter as a reference region only showed additional significant differences in amyloid- β burden between ADAD and LOAD in the anterior cingulate, amygdala, entorhinal cortex, brainstem, cerebellum, and globus pallidus (though this last region did not demonstrate significantly different amyloid- β plaque burden in ADAD versus LOAD). Unfortunately, previous work has shown that white matter reference regions may exhibit confounding age-effects, especially in studies of LOAD [79]. Thus, comparing regional differences in amyloid- β burden accurately between ADAD and LOAD

cohorts using PiB PET may be impossible using a standard approach. One compromise solution may be to use a combined cerebellar gray and white matter reference region, which mitigates the effects of amyloid- β burden in the cerebellar gray matter of ADAD individuals and potentially also the age-related changes in the cerebellar white matter of LOAD individuals; however, this combined reference region still fails to demonstrate the elusive between-cohort differences in amyloid- β burden in several regions implicated by our stereology results (Figure 3.2). Potential reasons for this discrepancy are noted in the penultimate paragraph of this Discussion.

Finally, our results suggest that diffuse and cored/compact amyloid- β plaque burdens are on average greater in ADAD than in LOAD, with diffuse plaque area fraction being greater in ADAD versus LOAD in all brain regions assessed in this study, except for the parietal lobe and globus pallidus. Interestingly, another neuropathological study showed a higher *density* of compact plaques and an equal degree of diffuse plaques in ADAD relative to LOAD, though this was a semi-quantitative study where regional distribution was not taken into account [46]. While overall amyloid- β plaque burdens may generally be greater in ADAD versus LOAD, this difference may not be true for each case of ADAD. Our current experiment encapsulates the heterogeneity in phenotypes previously described across the amyloid- β PET imaging literature of ADAD: Koivunen and colleagues found striatal elevations in specific *PSEN1* mutation carriers [80] and Remes and colleagues found striatal and posterior cingulate elevations in *APP* mutation carriers [81]; Theuns and colleagues found an *APP* mutation carrier who demonstrated elevated amyloid- β burden in cerebral cortex with sparing of subcortex and cerebellum [82]; Tomiyama and colleagues found an *APP* mutation carrier who demonstrated very low amyloid- β signal in the brain [83], and Schöll and colleagues found a similar result in another two *APP* mutation carriers [84]. Beyond imaging studies, many other studies have observed heterogeneities in the ADAD

population, including in age of onset and clinical presentation [85–88] as well as implicated amyloid- β species [89,90]. It would be of future interest to determine how the heterogeneities observed in these other domains may relate to the heterogeneities we observed in postmortem stereology of diffuse and cored/compact plaque burden.

While general correspondence between amyloid- β PET and neuropathologic assessment has been evaluated by several studies, few have done so with unbiased, quantitative stereologic measurements as in the current study. In general, we found that the semi-quantitative ABC scoring of neuropathology cases using Thal phase, Braak NFT stage, and CERAD neuritic plaque score [91] was not granular enough to capture differences and variability between individuals and cohorts that were seen when using quantitative stereologic measurements. Notably, all ADAD cases in our study were Thal phase 5, Braak NFT stage VI, and CERAD neuritic plaque score “frequent”. Additionally, LOAD cases were mostly Thal phase 5 (with two borderline exceptions), mostly Braak NFT stage V, and all CERAD neuritic plaque score “frequent”. This is consistent with our previous study, which found substantial inter-cohort differences in tau neurofibrillary tangle, neuropil thread, and neuritic plaque burden in a cohort of seven ADAD and 10 LOAD individuals who were nonetheless all assessed as Braak NFT stage VI [71].

Nevertheless, several findings from previous studies are concordant with ours, even when reagents and analytic methods differ substantially. For example, Klunk and colleagues compared PiB PET SUVRs of two *PSEN1* mutation carriers who had developed clinical AD – using pons as the reference region – with qualitative assessment of 10D5-immunostained amyloid- β plaques in the striatum of the parent of one of the mutation carriers; from this indirect study, they found intense amyloid- β radiotracer binding in the striatum, consistent with findings from postmortem neuropathology [92]. Two caveats, however: first, the premise that motivated Klunk and

colleagues to use the pons as a reference region – that the pons is a region free of amyloid- β – may not be true for all cases of ADAD; indeed, as our study illustrates, use of this reference region might account for their observation that cortical amyloid- β radiotracer retention was not greater in ADAD versus LOAD. Additionally, we cannot exclude the possibility that the distribution and characteristics of amyloid- β deposits across individuals with the same pathogenic variant completely align.

Imaging-pathology correspondence has not been well-studied in ADAD beyond the previous paper, but it has been more extensively studied in the LOAD literature. Clark and colleagues [93] compared semiquantitative visual ratings and [18F]AV45 (also known as florbetapir or Amyvid) SUVRs with semiquantitative rating and quantitative – but not stereologic – assessment of 4G8 immunostained amyloid- β plaques. This comparison was done across six regions of interest in 29 individuals (which was expanded to 59 individuals in a follow-up study [94]), ranging from cognitively normal to clinically diagnosed with LOAD and non-AD dementia, but all approaching the end of life [93]. In accord with the current study, Clark and colleagues found strong correlations between ante- and postmortem measurements of amyloid- β burden in the frontal, parietal, and temporal lobes and anterior cingulate gyrus, though they additionally found significant correlations in the posterior cingulate and precuneus, which did not reach significance for LOAD in our current study. That our LOAD cohort did not include cognitively normal or non-AD dementia individuals may have contributed to this difference between the two studies; other potential factors include the use of different amyloid- β PET binding agents and different primary anti amyloid- β antibodies.

Particularly of interest are LOAD imaging-pathology studies that also use the PiB PET radioligand. Of note among these is a study by Ikonomic and colleagues, which compared PiB

PET distribution volume ratios (DVRs) and quantitative – but not stereologic – assessment of 6-CN-PiB stained and 6E10 immunostained amyloid- β plaques in a single LOAD individual across 19 regions of interest, including the cortical ribbon and most subcortical nuclei, all sampled in a single axial plane; correlations were strong overall between regional PiB PET DVRs and 6E10 immunostained diffuse and cored/compact amyloid- β plaques [66]. Another study is by Driscoll and colleagues, who investigated six older adults – none of whom progressed to certain AD dementia – by comparing regional PiB PET DVRs with stereologic measurements of 6E10 immunostained amyloid- β plaques; they found statistically significant correlations in the anterior and posterior regions of the cingulate gyrus and in the precuneus [95]. Murray and colleagues investigated 35 cases with antemortem PiB PET imaging and postmortem semi-quantitative scoring and found a PiB PET summary region SUVR of 1.4 was approximately equivalent to a Thal phase of 1 to 2, and that Thal phase, but not Braak NFT stage or cerebral amyloid angiopathy (CAA) score, predicted PiB PET summary region SUVRs [96]. Moving beyond PiB PET studies, Curtis and colleagues investigated 68 patients with antemortem [18F]flutemetamol PET and postmortem semi-quantitative scores; the authors found a median sensitivity and specificity of 88% among five visual readers interpreting [18F]flutemetamol PET scans as positive or negative, compared to the reference standard of postmortem neuritic plaque density as assessed by the modified CERAD score [97]. Ikonomic and colleagues studied 106 end-of-life subjects with antemortem [18F]flutemetamol PET and postmortem semi-quantitative scores, finding that the probability of an abnormal [18F]flutemetamol PET scan increased with neocortical neuritic plaque density (though diffuse plaques and CAA may explain cases with abnormal [18F]flutemetamol PET scans but low neuritic plaque burden), and concluding that amyloid- β in the form of neuritic plaques is the primary form of amyloid- β detectable by [18F]flutemetamol PET [98]. Sabri and

colleagues studied 74 trial participants with antemortem [18F]florbetaben PET and postmortem CERAD scores and concluded that [18F]florbetaben PET demonstrated high sensitivity and specificity for detecting neuritic plaques [99]. Thal and colleagues investigated three cohorts of human autopsy cases neuropathologically and biochemically for the distribution of plaques and CAA, quantity, and composition of amyloid- β pathology and found that these three measures correlated with each other and with [18F]flutemetamol PET, neurofibrillary tangles, neuritic plaques, and dementia severity [100].

One important issue to note when comparing results across studies is that not only are there differences between which amyloid- β PET radioligands are used during antemortem imaging, but there are also differences between which anti-amyloid- β antibodies are used during postmortem immunostaining. Our current study uses the 10D5 antibody to visualize amyloid- β pathology, which is an anti-amyloid- β antibody against N-terminal epitopes [101]. Antibodies against C-terminal epitopes, such as 12F4 or 4G8, may be more sensitive in detecting the earliest appearing amyloid- β deposits in AD and Down syndrome [102–105], and may be of interest in future studies investigating earlier disease stages of LOAD and ADAD and making finer distinctions between plaque subtypes than in our current study.

This current study does have some additional limitations. One potential criticism of the current study is that the imaging-autopsy interval, namely the time interval between the antemortem PiB PET imaging visit and the start of autopsy, could not be matched between ADAD and LOAD cohorts. In the ADAD cohort, individuals continued to undergo PiB PET imaging exams well after showing clinical signs of AD, and imaging-autopsy intervals in the cohort ranged from 0.68 to 5.6 years with an average of 2.4 years. In contrast, individuals in the LOAD cohort did not undergo imaging studies once they progressed to moderate dementia, and the imaging-

autopsy intervals ranged from 0.3 to 9.6 years with an average of 4.7 years. The primary concern would be whether this difference caused greater discordances between ante- and postmortem assessments of amyloid- β burden in the LOAD versus ADAD cohort. Relevant to this issue, two points of evidence suggest that this imaging-autopsy interval difference is not likely to account for all of the differences in amyloid burden between LOAD and ADAD. First, the strongest correlation between PiB PET SUVR and diffuse plaque burden in the entire study was observed within the LOAD cohort, within the parietal lobe (Pearson's $r=0.83$, FDR-adjusted p -value=0.00098). Second, according to highly-cited leading articles in the field of AD research, amyloid- β deposition in the brain occurs over decades, and the majority of it occurs well before clinical symptoms of AD appear [106,107]; in this scenario, a difference of 2.4 years near the end of that 15-to-20-year period is unlikely to impact amyloid burdens substantively. Additionally, the *rate* of amyloid- β deposition slows as an individual enters the symptomatic phase of the disease, and this phenomenon lessens the effect of the imaging-autopsy interval on differences in plaque burden prior to and at death [108]. A related limitation to the long interval between PiB PET and postmortem analysis is that the AD process also advanced during this interval – the PET findings were in the milder stages of AD, whereas the postmortem analysis was at the end-stage of the disease, so end-stage findings may not reflect mild stage findings and vice-versa.

Another difference between the ADAD and LOAD cohorts to be mindful of is age. Age-related co-morbidities are far more common in LOAD than in ADAD [41], and three LOAD participants in this study were over 90 years of age. Specifically in our study, we observed both microinfarcts and TDP-43 pathology, both of which are common co-morbidities among such “oldest-old” individuals [109,110]. Nonetheless, since the focus of the current study is the quantification of amyloid- β burden, the presence of co-morbidities and their potential to contribute

to dementia do not complicate our main findings. This is particularly relevant as there are no known reports of amyloid- β immunostain or radioligand off-target binding to microinfarcts or TDP-43 aggregates, which would be one way these co-morbidities could complicate the quantification of amyloid- β burden.

Another limitation of our study is the manner in which regions were matched between imaging and neuropathology. Regional PiB PET SUVRs were derived from FreeSurfer regions (from the Desikan-Killiany atlas [45]) whereas regional plaque area fractions were derived from standard tissue blocks included in DIAN and Knight ADRC postmortem assessment protocols [41]. FreeSurfer regions and tissue blocks were matched on the basis of shared nomenclature or spatial overlap; however, this solution is imperfect. One primary issue is that brain structures were segmented in their entirety through imaging, but were only be sampled in a chosen plane in neuropathology. For example, neuropathologic assessment of the hippocampus and parahippocampal gyrus was performed at the level of the lateral geniculate nucleus, whereas the hippocampus and parahippocampal gyrus were assessed in their entirety in imaging. Previous work has noted this may lead to discordances in imaging-neuropathology comparisons [71], and future work will aim to target the same regions across both imaging and neuropathology with greater accuracy using improved co-registration methods [111].

Another limitation is that our study does not account for the presence or degree of amyloid- β deposition in the walls of small cortical blood vessels, or CAA, during stereologic quantification. CAA is known to be an additional source of the PiB PET signal [112], potentially contributing to its regional variability across disease conditions [113,114], and can be more prevalent and severe in ADAD relative to LOAD [46]. As such, it may account for higher PiB PET signal in the occipital lobe in ADAD versus LOAD independently of plaque burden, and otherwise influence the

correlation between amyloid- β pathology and PiB PET signal in ways not measured in the current study. CAA may also impact PiB PET SUVR measurements more broadly by appearing within the cerebellum. Like the occipital lobe, the cerebellum often shows disproportionately high CAA relative to other brain areas. However, in the current study, when assessed semi-quantitatively [115,116], CAA does not show any statistically significant correlations with diffuse or cored/compact plaque burden, or PiB PET SUVR, in either the ADAD or LOAD cohort.

We also acknowledge two other limitations of this study. The current imaging-neuropathology findings cannot address whether the PiB PET signal maintains the correlations with diffuse and compact plaque burden as seen here throughout the course of ADAD and LOAD. End-stage postmortem studies cannot determine the absolute staging of different plaque morphologies, though the earliest plaque forms observed in the non-demented aged brain are typically of the diffuse type. This observation may impact the appropriate time to administer anti-amyloid- β drug interventions, which would aim to prevent more cored/compact plaque formation; cored/compact plaques, because they are more likely to be neuritic, may be more closely linked than diffuse plaques to tau pathology, neurodegeneration, and cognitive impairment. Nonetheless, findings from our extended imaging cohort support the idea of developing separate PET staging schemes for ADAD versus LOAD across the lifespan as well. In ADAD, we see most frequent elevations of amyloid- β burden in regions outside the medial temporal lobe, while in LOAD, we see most frequent elevations of amyloid- β burden in posterolateral temporal lobe regions, suggesting two different origins of β -amyloidosis in the two diseases. Furthermore, in ADAD, striatal amyloid- β accumulation appears in step with other cortical amyloid- β accumulation, whereas in LOAD, striatal amyloid- β accumulation appears along with medial temporal lobe amyloid- β accumulation. Our observations in the ADAD participants are consistent with prior

longitudinal analyses in the ADAD population [117] and our observations in the LOAD participants are consistent with prior LOAD schemes, in particular, the scheme of Grothe and colleagues [118], who propose that amyloid- β deposition appears first in temporobasal and frontomedial regions, and appears latest in the medial temporal lobe and striatum. Additional work is needed to understand how changes in the spatial distribution and intensity of the PiB PET signal throughout the disease course of ADAD relates to the distribution of plaque pathology, which has been more extensively studied in the context of LOAD [118–121].

Finally, we note that our current histological approach measures amyloid- β plaque burden in a semi-quantitative approach by its *area*. Thus, in a situation where a diffuse plaque and cored/compact plaque might have the same area, the cored/compact plaque may have a higher *mass* of amyloid- β . This is in contrast to the semi-quantitative nature of PiB PET, where PiB retention is proportional to the number of available binding sites – presumably determined by the *mass* of fibrillar amyloid- β – whether amyloid- β is deposited in the form of a diffuse or cored/compact plaque. This presumption is also somewhat speculative as it is unknown whether the PiB radiotracer can fully penetrate a solid fibrillar plaque core within the typical timeframe of a PiB PET imaging study; it is also possible that conformational and/or biochemical differences might alter the availability of binding sites. The numerous aforementioned differences in how PiB PET and amyloid- β plaques are quantified leave room for future studies to develop more comparable semi-quantitative measures of ante- and postmortem amyloid- β burden. Two promising directions are light microscope high-resolution autoradiography [122], which might be able to quantify the intensity of radiotracer signal contributed by individual plaques in a manner that avoids the issue of quantifying the mass of fibrillar amyloid- β by its area; and single-molecule imaging [123] and small angle neutron scattering [124,125], which may help us understand the

relationship between fibrillar amyloid- β aggregates and various amyloid- β plaque types. A third approach would be to move away from purely neuropathological approaches of assessing characteristics of plaque pathology to instead focus on biochemical approaches. Biochemical approaches quantifying amyloid- β species from brain tissue homogenates have shed light on amyloid pathology in LOAD, indicating increased amounts of A β 40 or A β 42(43) relative to plaque types [126,127]. More recently, a study in LOAD evaluated biochemical fractions of amyloid- β from brain tissue compared to PET imaging to estimate which biochemical pools were most affected in AD, and derived a first approximation of the rates of amyloid- β accumulation [128]. Such approaches can also reveal distinct molecular profiles of amyloid- β in LOAD and ADAD [129].

In summary, our data indicate that there is a close association between fibrillar amyloid- β burden as visualized by PiB PET and as assessed by postmortem stereologic measures. Caveats may be raised: individuals with ADAD show considerable variability in amyloid- β burden and distribution that can also differ considerably from that typical of LOAD; therefore, summary and reference regions commonly used in PiB PET studies of LOAD may potentially need to be adjusted for PiB PET studies of ADAD. This point is especially important when evaluating anti-amyloid- β drug trials that enroll participants with ADAD. In such studies, investigators should be alert to the possibility of variable drug responses and interpret differences in cross-sectional measures of amyloid- β burden between treatment groups with care; indeed, individual-focused longitudinal monitoring strategies might be favorable. Additionally, when comparing trials of the same anti-amyloid- β drug conducted in ADAD versus LOAD, investigators should note that the choice of reference region can strongly influence interpretations of regional amyloid- β burden differences between cohorts.

Chapter 4: Longitudinal head-to-head comparison of ^{11}C -PiB and ^{18}F -florbetapir PET in a Phase 2/3 clinical trial of anti-amyloid- β monoclonal antibodies in dominantly inherited Alzheimer disease

4.1 Abstract

4.1.1 Purpose

Pittsburgh Compound-B (^{11}C -PiB) and ^{18}F -florbetapir are amyloid- β (A β) positron emission tomography (PET) radiotracers that have been used as endpoints in Alzheimer disease (AD) clinical trials to evaluate the efficacy of anti-A β monoclonal antibodies. However, comparing drug effects between and within trials may become complicated if different A β radiotracers were used. To study the consequences of using different A β radiotracers to measure A β clearance, we performed a head-to-head comparison of ^{11}C -PiB and ^{18}F -florbetapir in a Phase 2/3 clinical trial of anti-A β monoclonal antibodies.

4.1.2 Methods

Sixty-six mutation-positive participants enrolled in the gantenerumab and placebo arms of the first Dominantly Inherited Alzheimer Network Trials Unit clinical trial (DIAN-TU-001) underwent both ^{11}C -PiB and ^{18}F -florbetapir PET imaging at baseline and during at least one follow-up visit. For each PET scan, regional standardized uptake value ratios (SUVRs), regional Centiloids, a global cortical SUVR, and a global cortical Centiloid value were calculated. Longitudinal changes in SUVRs and Centiloids were estimated using linear mixed models. Differences in longitudinal change between PET radiotracers and between drug arms were estimated using paired and Welch

two sample t-tests, respectively. Simulated clinical trials were conducted to evaluate the consequences of some research sites using ^{11}C -PiB while other sites use ^{18}F -florbetapir for A β PET imaging.

4.1.3 Results

In the placebo arm, the absolute rate of longitudinal change measured by global cortical ^{11}C -PiB SUVRs did not differ from that of global cortical ^{18}F -florbetapir SUVRs. In the gantenerumab arm, global cortical ^{11}C -PiB SUVRs decreased more rapidly than global cortical ^{18}F -florbetapir SUVRs. Drug effects were statistically significant across both A β radiotracers. In contrast, the rates of longitudinal change measured in global cortical Centiloids did not differ between A β radiotracers in either the placebo or gantenerumab arms, and drug effects remained statistically significant. Regional analyses largely recapitulated these global cortical analyses. Across simulated clinical trials, type I error was higher in trials where both A β radiotracers were used versus trials where only one A β radiotracer was used. Power was lower in trials where ^{18}F -florbetapir was primarily used versus trials where ^{11}C -PiB was primarily used.

4.1.4 Conclusion

Gantenerumab treatment induces longitudinal changes in A β PET, and the absolute rates of these longitudinal changes differ significantly between A β radiotracers. These differences were not seen in the placebo arm, suggesting that A β -clearing treatments may pose unique challenges when attempting to compare longitudinal results across different A β radiotracers. Our results suggest converting A β PET SUVR measurements to Centiloids (both globally and regionally) can harmonize these differences without losing sensitivity to drug effects. Nonetheless, until consensus is achieved on how to harmonize drug effects across radiotracers, and since using multiple radiotracers in the same trial may increase type I error, multi-site studies should consider potential

variability due to different radiotracers when interpreting A β PET biomarker data and, if feasible, use a single radiotracer for the best results.

4.2 Introduction

The first two anti-amyloid- β (A β) drug arms of the first Dominantly Inherited Alzheimer Network Trials Unit clinical trial (DIAN-TU-001) evaluated the effects of the anti-A β monoclonal antibodies gantenerumab and solanezumab in participants with dominantly inherited Alzheimer disease (DIAD) [130]. Initial findings from Pittsburgh Compound-B (^{11}C -PiB) positron emission tomography (PET) imaging indicated that participants in the gantenerumab arm demonstrated longitudinal reduction of cerebral A β levels.

^{11}C -PiB and ^{18}F -florbetapir (i.e. Amyvid) are A β PET radiotracers that have been used as primary and secondary endpoints in AD clinical trials to evaluate the efficacy of anti-A β monoclonal antibodies. ^{11}C -PiB has been used in prior trials of bapineuzumab [131] and ponezumab [132], and ^{18}F -florbetapir has been used in prior trials of aducanumab [133], crenezumab [131], donanemab [134], gantenerumab [135], lecanemab [136], and solanezumab [137] (Table 4.1).

Table 4.1 A β PET radiotracers used in Phase 2 and Phase 3 clinical trials of anti-A β monoclonal antibodies for AD

Anti-A β monoclonal antibody	Sponsor	Clinical trial	A β PET radiotracer
Aducanumab	Biogen	NCT02477800	^{18}F -florbetapir
Bapineuzumab	Janssen and Pfizer	NCT02484547 NCT00574132 NCT00575055 NCT00667810 NCT00676143 NCT00996918 NCT00998764	^{11}C -PiB
Crenezumab	Roche	NCT02670083	^{18}F -florbetapir
Donanemab	Eli Lilly	NCT03367403	^{18}F -florbetapir
Gantenerumab	Roche and Washington University School of Medicine*	NCT01224106 NCT01760005* NCT02051608 NCT03443973 NCT03444870 NCT03444870 NCT03887455	^{18}F -florbetaben, ^{18}F -florbetapir, ^{18}F -flutemetamol, and ^{11}C -PiB
Lecanemab	Eisai	NCT00945672	^{18}F -florbetapir
Ponezumab	Pfizer	NCT01127633	^{11}C -PiB
Solanezumab	Eli Lilly and Washington University School of Medicine*	NCT01760005* NCT01900665 NCT02008357 NCT02760602	^{18}F -florbetapir and ^{11}C -PiB

However, comparing drug effects between trials may not be straightforward if different A β radiotracers were used across trials. While ^{11}C -PiB and ^{18}F -florbetapir share numerous similarities, such as correlated binding characteristics [138] and shared high-affinity binding sites [139], they also demonstrate important differences, such as the greater white matter signal variability of ^{18}F -florbetapir [138,140–142], and the lower cortical uptake relative to white matter uptake of ^{18}F -florbetapir, which has been hypothesized to contribute to the smaller range of standardized uptake value ratios (SUVRs) seen in ^{18}F -florbetapir versus ^{11}C -PiB PET [138]. Whether the differences between ^{11}C -PiB and ^{18}F -florbetapir are enough to impact the interpretation of drug effects is unknown, as all prior work comparing the two A β radiotracers were observational studies. Whether converting ^{11}C -PiB and ^{18}F -florbetapir SUVR results to the Centiloid scale [143] – as is often done in observational studies to standardize results from different A β radiotracers to a common unit of measurement – will sufficiently harmonize ^{11}C -PiB and ^{18}F -florbetapir estimates of drug treatment is also unknown.

Among interventional studies, the DIAN-TU-001 is unique, as most participants underwent both ^{11}C -PiB and ^{18}F -florbetapir PET imaging at baseline and during at least one follow-up visit. This provides an opportunity to perform a head-to-head comparison of ^{11}C -PiB and ^{18}F -florbetapir to study the consequences of using different A β radiotracers to measure A β change in the same individuals.

4.3 Materials and methods

4.3.1 Study approval

The study was conducted in accordance with the Declaration of Helsinki (version 7) and the International Conference on Harmonization and Good Clinical Practice guidelines. Protocols for

the study have received prior approval by the local Institutional Review Board (IRB) or Ethics Committee of each DIAN site, and by the Washington University IRB for the Knight ADRC. Participants or their caregivers provided written informed consent. The clinical trial registration number is NCT01760005.

4.3.2 Participant characteristics

In the DIAN-TU-001, 52 DIAD mutation-positive participants were enrolled in the gantenerumab arm and 40 DIAD mutation-positive participants were enrolled in the placebo arm. Among them, 41 participants in the gantenerumab arm and 25 participants in the placebo arm underwent both ^{11}C -PiB and ^{18}F -florbetapir PET imaging at baseline and during at least one follow-up visit (Table 4.2). During these visits, ^{11}C -PiB and ^{18}F -florbetapir PET were acquired with at most 28 days between imaging sessions.

Due to the lack of a significant effect on ^{11}C -PiB PET outcomes in the solanezumab arm [130], the current study is limited to the gantenerumab and placebo arms.

Table 4.2 Participant characteristics

		Gantenerumab	Placebo
Number		41	25
Female, n		15 (37%)	16 (64%)
Mean age (SD)		46 (10)	44 (10)
CDR®, n	=0	25 (61%)	14 (56%)
	>0	16 (39%)	11 (44%)
Mean EYO (min, max)		-2.1 (-14, 10)	-2.4 (-15, 10)
Family mutation, n	<i>PSEN1</i>	34 (83%)	18 (72%)
	<i>PSEN2</i>	3 (7%)	2 (8%)
	<i>APP</i>	4 (10%)	5 (20%)
<i>APOE</i> , n	$\epsilon 4$ -	29 (71%)	17 (68%)
	$\epsilon 4$ +	12 (29%)	8 (32%)

Abbreviations: *APOE* (apolipoprotein E), *APP* (A β precursor protein), CDR® (Clinical Dementia Rating®), EYO (Estimated Years to symptom Onset), *PSEN1* (presenilin-1), *PSEN2* (presenilin-2), SD (standard deviation).

4.3.3 A β PET acquisition

Participants were scanned on DIAN-approved PET scanners [144,145]. Participants received a single 13 ± 3 (mean \pm standard deviation) mCi intravenous bolus injection of ^{11}C -PiB or a single 9.8 ± 0.7 (mean \pm standard deviation) mCi intravenous bolus injection of ^{18}F -florbetapir (Avid Radiopharmaceuticals, a wholly owned subsidiary of Eli Lilly and Company) at each imaging

session. Emission data were collected 40-70 minutes post injection for ^{11}C -PiB [146] and 50-70 minutes post injection for ^{18}F -florbetapir [140]. List-mode data were reconstructed using ordered subset expectation maximization. A low-dose CT scan preceded PET acquisition for attenuation correction. Reconstructed PET images were processed using the PET Unified Pipeline (<https://github.com/ysu001/PUP>) [16,17]. After segmenting MR images into regions of interest using FreeSurfer version 5.3 [18], regional standardized value uptake ratios (SUVRs) were defined from the reconstructed PET images using a cerebellar gray reference region. A global cortical SUVR for each image was defined as the sum of the mean bilateral SUVRs of the precuneus, superior frontal, rostral middle frontal, lateral orbitofrontal, medial orbitofrontal, superior temporal, and middle temporal ROIs. A global cortical Centiloid for each image was defined by standardizing the mean cortical SUVR to the Centiloid scale [140,143]. Additionally, regional Centiloids were defined by standardizing regional SUVRs to the Centiloid scale by the direct conversion process (method-2) described in Klunk et al. [143].

4.3.4 MRI acquisition

Participants were scanned on DIAN-approved 3T MRI scanners [144,145]. Across all scanners, T1-weighted head MR images were acquired using magnetization prepared rapid gradient echo generalized autocalibrating partial parallel acquisition sequence with a repetition time=2300 ms, echo time=2.95 ms, flip angle=9°, and voxel resolution=1.1×1.1×1.2 mm³.

4.3.5 Statistical analysis of DIAN-TU-001 data

Longitudinal annualized change in regional SUVRs, global cortical SUVRs, regional Centiloids, and global cortical Centiloids were estimated using linear mixed models. Linear mixed models included individual-level random intercepts and random slopes to account for the correlation across repeated measurements from the same individual over time. Differences in longitudinal

change between PET radiotracers and between drug arms were estimated using paired and Welch two sample t-tests, respectively. In particular, test statistics pertaining to regional SUVRs had their p-values adjusted for false discovery rate (FDR) control by the Benjamini-Hochberg procedure [147] at the 0.05 level for discussion purposes.

All analyses were conducted using R version 4.0.2 [22].

4.3.6 Statistical simulations

International clinical trials may necessitate the use of different A β radiotracers within the same trial due to the availability of each radiotracer at each site. An analysis of each radiotracer separately may underpower the study, or it may lead to difficulties in interpretation if the cohorts receiving different radiotracers have differences in their demographics. Taking imaging measures derived from different radiotracers, harmonizing them by the Centiloid method, and then analyzing together would obtain an estimate of treatment efficacy. However, whether this harmonization is appropriate for treatment efficacy inference, e.g. control of type I error, influence on power, has not been investigated before. To evaluate the impact of allowing the use of multiple A β PET radiotracers in the same trial, clinical trials were simulated such that participants were scanned with either ^{11}C -PiB or ^{18}F -florbetapir. Details of the simulations are as follows:

- Bivariate linear mixed models were fit to Centiloid- ^{11}C -PiB and Centiloid- ^{18}F -florbetapir data from the gantenerumab and placebo arms to obtain, for both radiotracers, simultaneously: (1) the covariance matrix of the random intercepts and slopes of the longitudinal data of these two radiotracers; (2) the within-subject error variance for each radiotracers; and (3) the baseline and slopes of each trial arm for each radiotracer.

- The parameters obtained above were then used to simulate individual-level longitudinal data for each radiotracer.
- The following conditions were simulated: sample size=20 participants per arm (treatment arm and placebo arm), 32 participants per arm, and 40 participants per arm; randomization ratio=1:1; participant dropout=0% annually and 5% annually; percentage of participants scanned with ^{18}F -florbetapir=100% (no participants scanned with ^{11}C -PiB), 75%, 50%, 25%, and 0% (all participants scanned with ^{11}C -PiB). For example, for sample size=20 participants per arm and ^{18}F -florbetapir=100%, all participant data in both the treatment and placebo arms were simulated based on the parameters estimated from the Centiloid- ^{18}F -florbetapir data, whereas for the same sample size and ^{18}F -florbetapir=75%, 15 participants of the 20 in each arm were simulated based on the parameters estimated from the Centiloid- ^{18}F -florbetapir data and 5 participants were simulated based on the parameters estimated from the Centiloid- ^{11}C -PiB data. These simulations aimed to cover a broad range of possible data mixing from both radiotracers to evaluate the impact of using two radiotracers on trial outcome in terms of type I error and power.
- Two scenarios were investigated: (1) The no treatment effect, namely both the treatment arm and the placebo arm were simulated using the parameters estimated from the placebo arm of the DIAN-TU-001 study. This provides an estimate of type I error; and (2) the observed treatment effect in the DIAN-TU-001 study, namely the treatment arm was simulated based on the parameters estimated from the gantenerumab arm of the DIAN-TU-001 study and the placebo arm was simulated based on the parameters estimated from the placebo arm of the DIAN-TU-001 study.

- Mimicking the DIAN-TU-001 study schedule [130], longitudinal data were simulated for each participant. Specifically, each participant's intercept and slope were first simulated based on parameters estimated from the trial, then each individual's longitudinal data were simulated using the intercept and slope plus a within-subject error term.
- Each simulated trial was analyzed using linear mixed models with random intercepts and slopes to estimate the difference in the slope (annualized rate of change) between the simulated treatment and simulated placebo arms and output a corresponding p-value. If the two-sided p-value was less than 0.05, then the corresponding trial was considered to reach statistical significance for treatment efficacy.
- A thousand simulated clinical trials were conducted for each scenario above. Overall power and type I error were calculated as the percentage of the 1000 simulated clinical trials that reached statistical significance at a two-sided type I error of 5%.

All simulations were conducted using SAS software, version 9.4.

4.4 Results

4.4.1 DIAN-TU-001 clinical trial results

Mean baseline global cortical SUVRs and Centiloids in the gantenerumab and placebo arms are shown in Table 4.3. The mean of baseline global cortical SUVRs calculated from ^{11}C -PiB (global cortical SUVR- ^{11}C -PiB) in the gantenerumab arm (1.7, standard error [SE]=0.08 [4.8% of the mean]) was similar to that of the placebo arm (1.7, SE=0.09 [5.4%]), with no statistically significant difference (Welch two sample t-test p-value=0.74, Table 3). The mean of baseline global cortical SUVRs calculated from ^{18}F -florbetapir (global cortical SUVR- ^{18}F -florbetapir) in the gantenerumab arm (1.5, SE=0.06 [3.7%]) was also similar to that of the placebo arm (1.4,

SE=0.05 [3.7%]), with no statistically significant difference (Welch two sample t-test p-value=0.48, Table 3). Consistent with the higher dynamic range of ^{11}C -PiB, mean baseline global cortical SUVR- ^{11}C -PiB and SUVR- ^{18}F -florbetapir showed statistically significant differences within the gantenerumab arm (paired t-test p-value= 2.7×10^{-6}) and within the placebo arm (paired t-test p-value=0.00030, Table 4.3).

Table 4.3 Mean baseline global cortical SUVR and Centiloid in the gantenerumab and placebo arms as measured by ^{11}C -PiB and ^{18}F -florbetapir

	Gantenerumab	Placebo	Gantenerumab versus placebo t-value (p-value)	Gantenerumab versus placebo Cohen's d [95% CI]
Mean baseline global cortical SUVR- ^{11}C -PiB [95% CI]	1.7 [1.5, 1.9]	1.7 [1.5, 1.9]	0.34 (0.74)	0.08 [-0.40, 0.57]
Mean baseline global cortical SUVR- ^{18}F -florbetapir [95% CI]	1.5 [1.4, 1.6]	1.4 [1.3, 1.5]	0.72 (0.48)	0.18 [-0.31, 0.66]
Global cortical SUVR- ^{11}C -PiB versus SUVR- ^{18}F -florbetapir t-value (p-value)	5.5 (2.7×10^{-6})***	4.2 (0.00030)***		
Global cortical SUVR- ^{11}C -PiB versus SUVR- ^{18}F -florbetapir Cohen's d	0.85 [0.49, 1.21]	0.84 [0.38, 1.30]		
Mean baseline global cortical Centiloid- ^{11}C -PiB [95% CI]	63 [46, 80]	59 [41, 77]	0.34 (0.74)	0.08 [-0.40, 0.57]
Mean baseline global cortical Centiloid- ^{18}F -florbetapir [95% CI]	61 [43, 79]	52 [35, 69]	0.72 (0.48)	0.18 [-0.31, 0.66]
Global cortical Centiloid- ^{11}C -PiB versus Centiloid- ^{18}F -florbetapir t-value (p-value)	0.43 (0.67)	1.17 (0.25)		
Global cortical Centiloid- ^{11}C -PiB versus Centiloid- ^{18}F -florbetapir Cohen's d [95% CI]	0.07 [-0.24, 0.37]	0.23 [-0.17, 0.63]		

*p-value<0.05, **p-value<0.01, ***p-value<0.001. Abbreviations: CI (confidence interval), SD (standard deviation).

The mean of baseline global cortical Centiloids calculated from ^{11}C -PiB (global cortical Centiloid- ^{11}C -PiB) in the gantenerumab arm (63) was similar to that of the placebo arm (59), with no statistically significant difference (because the Centiloid process involves only a simple linear transformation, all Welch two sample t-test t- and p-values are the same across corresponding global cortical SUVR and global cortical Centiloid comparisons and will not be mentioned further). Likewise, the mean of baseline global cortical Centiloids calculated from ^{18}F -florbetapir (global cortical Centiloid- ^{18}F -florbetapir) in the gantenerumab arm (61) was similar to that of the placebo arm (52). However, in contrast to global cortical SUVRs, baseline global cortical Centiloids calculated from the two A β radiotracers did not show statistically significant differences within the gantenerumab arm (paired t-test p-value=0.67) or within the placebo arm (paired t-test p-value=0.25, Table 4.3).

Mean rate of longitudinal change in global cortical SUVRs and Centiloids in the gantenerumab and placebo arms are shown in Table 4.4. The mean annualized rate of global cortical SUVR-¹¹C-PiB change in the gantenerumab arm (-0.045 [-2.6% change from baseline], SE=0.0086 [19% of the change]) differed from that of the placebo arm (0.022 [1.3%], SE=0.0081 [37%]) and this difference was statistically significant (Welch two sample t-test p-value= 6.6×10^{-12} , Table 4.4 and Figure 4.1). The mean annualized rate of global cortical SUVR-¹⁸F-florbetapir change in the gantenerumab arm (-0.030 [-2.0%], SE=0.0078 [26%]) differed from that of the placebo arm (0.015 [1.1%], SE=0.0088 [59%]) and this difference was statistically significant (Welch two sample t-test p-value= 1.7×10^{-8}). Comparing mean annualized rates of global cortical SUVR-¹¹C-PiB and SUVR-¹⁸F-florbetapir change within the gantenerumab arm showed statistically significant differences (paired t-test p-value=0.00034), but not within the placebo arm (paired t-test p-value=0.26, Table 4.4 and Figure 4.1).

Table 4.4 Mean rates of longitudinal change in global cortical SUVR and Centiloid in the gantenerumab and placebo arms as measured by ¹¹C-PiB and ¹⁸F-florbetapir

	Gantenerumab	Placebo	Gantenerumab versus placebo t-value (p-value)	Gantenerumab versus placebo Cohen's d [95% CI]
Mean annualized global cortical SUVR- ¹¹ C-PiB change (SE)	-0.045 (0.009)	0.022 (0.008)	-8.9 (6.6×10^{-12})***	-2.24 [-2.90, -1.58]
Mean annualized global cortical SUVR- ¹⁸ F-florbetapir change (SE)	-0.030 (0.008)	0.015 (0.009)	-6.6 (1.7×10^{-8})***	-1.64 [-2.21, -1.06]
Global cortical SUVR- ¹¹ C-PiB change versus SUVR- ¹⁸ F-florbetapir change t-value (p-value)	-3.9 (0.00034)***	1.2 (0.26)		
Global cortical SUVR- ¹¹ C-PiB change versus SUVR- ¹⁸ F-florbetapir change Cohen's d [95% CI]	-0.61 [-0.94, -0.27]	0.23 [-0.17, 0.63]		
Mean annualized global cortical Centiloid- ¹¹ C-PiB change (SE)	-4.6 (0.9)	2.2 (0.8)	-8.9 (6.6×10^{-12})***	-2.24 [-2.90, -1.58]
Mean annualized global cortical Centiloid- ¹⁸ F-florbetapir change (SE)	-5 (1)	3 (2)	-6.6 (1.7×10^{-8})***	-1.64 [-2.21, -1.06]
Global cortical Centiloid- ¹¹ C-PiB change versus Centiloid- ¹⁸ F-florbetapir change t-value (p-value)	0.62 (0.54)	-0.38 (0.71)		
Global cortical Centiloid- ¹¹ C-PiB change versus Centiloid- ¹⁸ F-florbetapir change Cohen's d [95% CI]	0.10 [-0.21, 0.40]	-0.08 [-0.47, 0.32]		

*p-value<0.05, **p-value<0.01, ***p-value<0.001. Abbreviations: CI (confidence interval), SE (standard error).

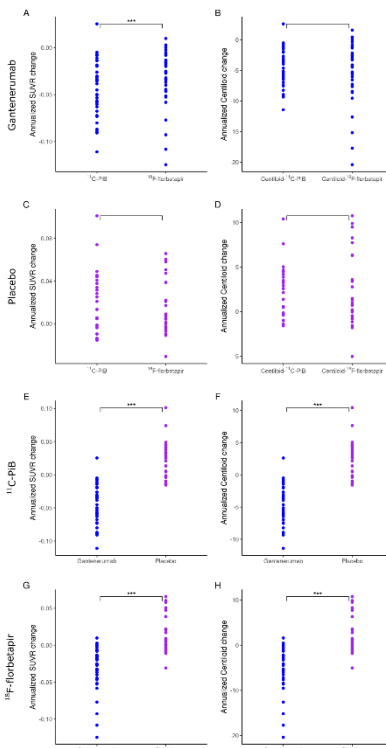


Figure 4.1 Rates of longitudinal change in global cortical SUVRs and Centiloids. (A) Annualized SUVR change in the gantenerumab arm as measured by ^{11}C -PiB and ^{18}F -florbetapir. (B) Annualized Centiloid change in the gantenerumab arm as measured by Centiloid- ^{11}C -PiB and Centiloid- ^{18}F -florbetapir. (C) Annualized SUVR change in the placebo arm as measured by ^{11}C -PiB and ^{18}F -florbetapir. (D) Annualized Centiloid change in the placebo arm as measured by Centiloid- ^{11}C -PiB and Centiloid- ^{18}F -florbetapir. (E) Annualized SUVR change in the gantenerumab and placebo arms as measured by ^{11}C -PiB. (F) Annualized Centiloid change in the gantenerumab and placebo arms as measured by Centiloid- ^{11}C -PiB. (G) Annualized SUVR change in the gantenerumab and placebo arms as measured by ^{18}F -florbetapir. (H) Annualized Centiloid change in the gantenerumab and placebo arms as measured by Centiloid- ^{18}F -florbetapir. *p-value<0.05, **p-value<0.01, ***p-value<0.001.

Mean annualized rate of Centiloid- ^{11}C -PiB change in the gantenerumab arm (-4.6) differed from that of the placebo arm (2.2) and this difference was statistically significant. Likewise, the mean annualized rate of Centiloid- ^{18}F -florbetapir change in the gantenerumab arm (-4.9) differed from that of the placebo arm (2.5) and this difference was statistically significant. However, in contrast to global cortical SUVRs, annualized rates of global cortical Centiloid change calculated from the two A β radiotracers did not show statistically significant differences within either the gantenerumab arm (paired t-test p-value=0.54) or within the placebo arm (paired t-test p-value=0.71, Table 4.4 and Figure 4.1).

Rates of longitudinal change in regional SUVRs are shown in Figure 4.4. Annualized rates of regional SUVR- ^{11}C -PiB and regional SUVR- ^{18}F -florbetapir change showed decreasing values across most brain areas in the gantenerumab arm (Figures 4.1A and 4.1B). In contrast, annualized rates of regional SUVR- ^{11}C -PiB and regional SUVR- ^{18}F -florbetapir change showed increasing values across most brain areas in the placebo arm (Figures 4.1C and 4.1D). Drug effects were statistically significant across all regional SUVR- ^{11}C -PiB and regional SUVR- ^{18}F -florbetapir results (Figures 4.1E and 4.1F).

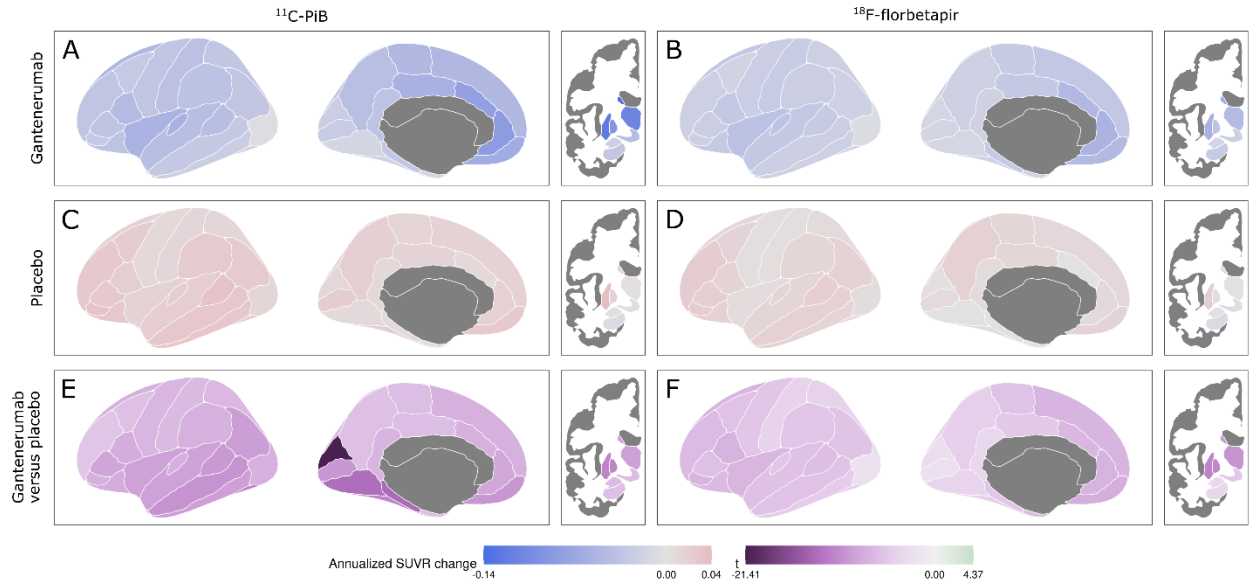


Figure 4.2 Rates of longitudinal change in regional SUVRs. (A, B) Mean annualized SUVR change in the gantenerumab arm as measured by ^{11}C -PiB and ^{18}F -florbetapir, respectively. (C, D) Mean annualized SUVR change in the placebo arm as measured by ^{11}C -PiB and ^{18}F -florbetapir, respectively. (E, F) Differences between longitudinal change in the gantenerumab arm versus the placebo arm as measured by ^{11}C -PiB and ^{18}F -florbetapir, respectively. Only regional comparisons associated with a FDR-adjusted p-value < 0.05 are shown.

Rates of longitudinal change in regional Centiloids are shown in Figure 4.2. Reporting longitudinal change in regional Centiloids recapitulated the above results: annualized rates of regional Centiloid- ^{11}C -PiB and regional Centiloid- ^{18}F -florbetapir change showed decreasing values across most brain areas in the gantenerumab arm (Figures 4.2A and 4.2B), increasing values across most brain areas in the placebo arm (Figures 4.2C and 4.2D), and drug effects remained statistically

significant across all regional Centiloid- ^{11}C -PiB and regional Centiloid- ^{18}F -florbetapir results (Figures 4.2E and 4.2F).

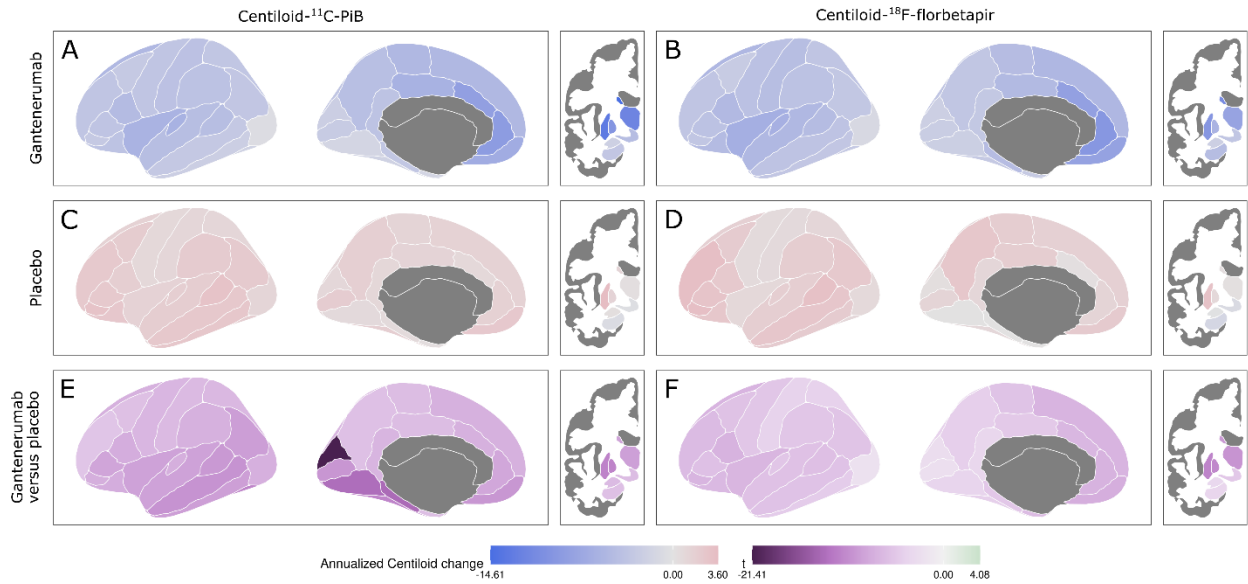


Figure 4.3 Rates of longitudinal change in regional Centiloids. (A, B) Mean annualized Centiloid change in the gantenerumab arm as measured by Centiloid- ^{11}C -PiB and Centiloid- ^{18}F -florbetapir, respectively. (C, D) Mean annualized Centiloid change in the placebo arm as measured by Centiloid- ^{11}C -PiB and Centiloid- ^{18}F -florbetapir, respectively. (E, F) Differences between longitudinal change in the gantenerumab arm versus the placebo arm as measured by Centiloid- ^{11}C -PiB and Centiloid- ^{18}F -florbetapir, respectively. Only regional comparisons associated with a FDR-adjusted p-value < 0.05 are shown.

However, while statistically significantly greater decreases in SUVR- ^{11}C -PiB versus SUVR- ^{18}F -florbetapir were observed across nearly every brain area in the gantenerumab arm, excepting the lateral orbitofrontal frontal gyrus, and basal regions of the temporal lobe and occipital lobe (Figure 4.4A), no statistically significantly different rates of change were seen in Centiloid- ^{11}C -PiB versus Centiloid- ^{18}F -florbetapir across most brain areas, excepting the lingual, parahippocampal, and entorhinal cortices (Centiloid- ^{18}F -florbetapir change greater than Centiloid- ^{11}C -PiB change), and most subcortical structures (Centiloid- ^{11}C -PiB change greater than Centiloid- ^{18}F -florbetapir) (Figure 4.4B). Similarly, while statistically significantly greater increases in SUVR- ^{11}C -PiB versus SUVR- ^{18}F -florbetapir were observed across several brain areas, including the medial orbitofrontal gyrus, and regions within the temporal lobe and medial occipital lobe (Figure 4.4A),

no statistically significantly different rates of change in Centiloid- ^{11}C -PiB versus Centiloid- ^{18}F -florbetapir were found across most brain areas, excepting the amygdala (Figure 4.4B).

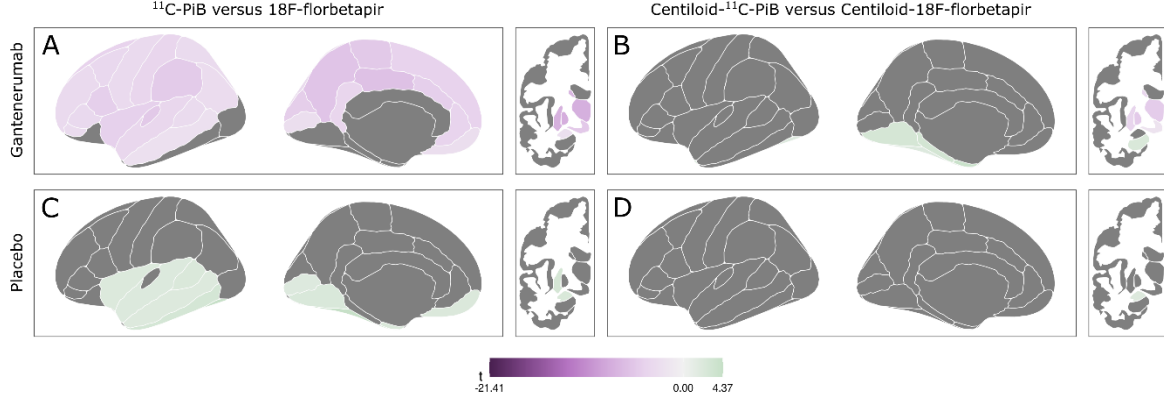


Figure 4.4 Rates of longitudinal change in regional SUVRs versus regional Centiloids. (A) Differences between longitudinal change in the gantenerumab arm as measured by ^{11}C -PiB versus by ^{18}F -florbetapir. (B) Differences between longitudinal change in the gantenerumab arm as measured by Centiloid- ^{11}C -PiB versus by Centiloid- ^{18}F -florbetapir. (C) Differences between longitudinal change in the placebo group as measured by ^{11}C -PiB versus by ^{18}F -florbetapir. (D) Differences between longitudinal change in the placebo group as measured by Centiloid- ^{11}C -PiB versus by Centiloid- ^{18}F -florbetapir. Only regional comparisons associated with a FDR-adjusted p-value < 0.05 are shown.

In addition, the difference between Centiloid- ^{11}C -PiB values at baseline for subcortical structures, for example, the caudate and putamen, versus the global cortical Centiloid- ^{11}C -PiB (mean caudate-global cortical Centiloid- ^{11}C -PiB=13, SE=4.7, 95% CI=[4.2, 23], mean putamen-global cortical Centiloid- ^{11}C -PiB=38, SE=4.5, 95% CI=[29, 47]), is much larger than the difference between Centiloid- ^{18}F -florbetapir for those structures and the global cortical Centiloid- ^{18}F -florbetapir (mean caudate-global cortical Centiloid- ^{18}F -florbetapir=-3.3, SE=4.3, 95% CI=[-11, 5.1], mean putamen-global cortical Centiloid- ^{18}F -florbetapir=25, SE=3.7, 95% CI=[18, 32]), which is statistically significant (caudate-global cortical Centiloid- ^{11}C -PiB versus caudate-global cortical Centiloid- ^{18}F -florbetapir t-value=5.9, p-value= 1.3×10^{-7} , putamen-global cortical Centiloid- ^{11}C -PiB versus putamen-global cortical Centiloid- ^{18}F -florbetapir t-value=5.0, p-value= 4.0×10^{-6}).

4.4.2 Simulated clinical trial results

The results of the simulated clinical trials where some participants are scanned with ^{11}C -PiB while others are scanned with ^{18}F -florbetapir are presented in Table 4.5. Under the no treatment effect

scenario, type I error remained consistent across different sample sizes (20 participants per arm, 32 participants per arm, and 40 participants per arm), and increased as the proportion of participants scanned with the two radiotracers approached 50% each. Under the observed treatment effect scenario, power increased as sample size increased, and increased as the proportion of participants scanned with ^{11}C -PiB approached 100%. Finally, simulating a 5% annual dropout rate in the above scenarios tended to decrease power, but did not have a consistent effect on type I error.

Table 4.5 Type I error and power (%) comparison when using both Centiloid- ^{11}C -PiB and Centiloid- ^{18}F -florbetapir in 1000 simulated clinical trials

Percent (%) of participants scanned with ^{18}F -florbetapir	No treatment effect (type I error comparison)					With observed treatment effect (power comparison)				
	100	75	50	25	0	100	75	50	25	0
20 participants per arm	4.8	9.3	14.8	9.7	4.3	52.9	63.3	65.0	72.5	84.3
32 participants per arm	4.9	8.2	14.6	9.4	5.7	74.4	81.1	83.7	88.4	98.0
40 participants per arm	4.5	8.0	15.0	9.6	4.9	85.0	88.2	88.6	93.9	98.9
With 5% annual dropout										
20 participants per arm	4.6	9.8	12.2	8.5	4.1	48.7	54.8	60.7	67.2	76.5
32 participants per arm	6.0	8.6	13.6	9.9	5.7	67.8	73.1	76.6	84.9	92.1
40 participants per arm	4.7	8.0	11.9	9.4	5.0	78.5	82.2	85.5	94.4	97.6

Each simulated dataset was analyzed using linear mixed models and the treatment effect was defined as the difference between the slopes (annual rate of change in Centiloid). Two-sided t-tests were used with a nominal type I error of 5%.

4.5 Discussion

Similarities and differences between the two A β radiotracers ^{11}C -PiB and ^{18}F -florbetapir have been well-investigated in observational studies of AD [138–142]. The baseline results from our current study of ^{11}C -PiB and ^{18}F -florbetapir PET imaging in the DIAN-TU-001 clinical trial bear out these past findings: at baseline, global cortical SUVR- ^{11}C -PiB differs statistically significantly from global cortical SUVR- ^{18}F -florbetapir in both the gantenerumab and placebo arms. After standardizing global cortical SUVR results to the Centiloid scale, global cortical Centiloid- ^{11}C -PiB shows no statistically significant differences with global cortical Centiloid- ^{18}F -florbetapir in either arm – a result consistent with the intended purpose of the Centiloid method [143]. In the placebo arm only, annualized rates of change did not show statistically significant differences

between ^{11}C -PiB and ^{18}F -florbetapir, whether measured with SUVR values or standardized to Centiloid units.

However, the effects of anti-A β drug treatment on ^{11}C -PiB and ^{18}F -florbetapir measures were not compared head-to-head previously. Our results from the gantenerumab arm of the DIAN-TU-001 show that annualized rates of change as measured by global cortical SUVR- ^{11}C -PiB and global cortical SUVR- ^{18}F -florbetapir are statistically significantly different, likely due to the greater dynamic range of ^{11}C -PiB, which appears to result in both greater baseline SUVR values and a greater drug-induced longitudinal decrease in SUVR. After standardizing global cortical SUVR results to the Centiloid scale, global cortical Centiloid- ^{11}C -PiB shows no statistically significant differences with global cortical Centiloid- ^{18}F -florbetapir – a result also consistent with the intended purpose of the Centiloid method. Thus, standardizing global cortical A β PET biomarker values to the Centiloid scale appears to eliminate statistically significant differences in baseline and longitudinal measurements made with ^{11}C -PiB versus ^{18}F -florbetapir, even when longitudinal changes are modified by anti-A β drug treatment as opposed to disease progression alone.

While most previous applications of the Centiloid conversion process have focused on determination of global cortical Centiloids, we also employed the determination of regional Centiloids also described in the original description of the Centiloid process by the direct conversion process (method-2) as described by Klunk and colleagues [143]. Here we found that standardizing regional A β PET biomarker values to the Centiloid scale appears to eliminate statistically significant differences in longitudinal measurements made with ^{11}C -PiB versus ^{18}F -florbetapir in most brain areas.

The brain areas that retain significant differences between regional ^{11}C -PiB and regional ^{18}F -florbetapir on the Centiloid scale require further investigation. The change in Centiloids was greater in the ^{18}F -florbetapir data in the lingual, parahippocampal, and entorhinal cortices – areas which did not show a greater change in the ^{18}F -florbetapir data when expressed in SUVR units. As these are areas with low retention of both tracers, the signals in these areas are dominated by noise. Thus, this finding may reflect greater noise in the ^{18}F -florbetapir data. The change in Centiloids was greater in the ^{11}C -PiB data in subcortical structures such as the caudate and putamen – areas which also showed a greater change in the ^{11}C -PiB data when expressed in SUVR units. This may relate to the finding that ^{11}C -PiB shows greater retention in subcortical structures than ^{18}F -florbetapir in DIAD. For example, in the current dataset, Centiloid- ^{11}C -PiB values at baseline were on average much greater than the global cortical Centiloid- ^{11}C -PiB in the caudate and putamen than Centiloid- ^{18}F -florbetapir values for the same comparisons. Thus, this difference in subcortical change in radiotracer retention may reflect real differences in the tracers and cannot be harmonized by the simple Centiloid conversion. If supported by further study, this will need to be considered in studies where subcortical changes are considered of high importance, such as studies in DIAD and Down syndrome populations where subcortical retention is early and prominent [148–151].

Previously reported annualized reductions of Centiloid- ^{18}F -florbetapir during gantenerumab or other different anti-A β monoclonal antibody treatments were greater than those reported in our study [135,136,152]. This may limit generalizability from DIAD to AD clinical trials. One reason for the discrepancy may be the insufficient amount of drug being administered in the DIAN-TU-001: the initial dose in the DIAN-TU-001 was 225 mg of gantenerumab administered every four weeks, until midway through the trial (approximately two to three years into the trial), when dose escalation was implemented to increase the gantenerumab dose to 1200

mg every four weeks [153]. In contrast, the dose escalation in the open-label extension of Marguerite RoAD was implemented over an initial two- to six-month titration period to increase the gantenerumab dose to 1200 mg every four weeks [135]. Another contributor could be that individuals with DIAD are generally younger than individuals with late-onset AD and, as one consequence, may have diminished antibody target engagement due to healthier and more intact blood brain barriers [154]. Ongoing studies in the gantenerumab DIAN-TU-OLE are testing higher doses due to higher A β loads and higher A β production [155] in DIAD.

However, reporting only a global cortical Centiloid results in a loss of potential information that can be derived from A β PET imaging. Many of the regions showing the largest SUVR/Centiloid differences were subcortical structures and not part of the global cortical SUVR/Centiloid composite used here – although these regions are part of the standard Centiloid cortical volume of interest. It may be informative for future trials to report both global cortical Centiloid – as has traditionally been done – as well as regional Centiloid measures, to reveal the extent to which anti-A β drug clearance is a local versus global phenomenon. This may become relevant in addressing the aforementioned question of whether a healthy blood brain barrier is inhibiting anti-A β monoclonal antibody penetration throughout the brain. An alternative strategy, which has the potential to be even more informative, would be to transform ^{18}F -florbetapir PET images into synthetic ^{11}C -PiB images at the voxel level using an encoding-decoding network [156].

A limitation to this study is that the Centiloid conversion equation for ^{18}F -florbetapir was established based on a subset of the baseline data of the cohort in this study [19]. Therefore, testing for the presence of baseline differences between Centiloid- ^{11}C -PiB and Centiloid- ^{18}F -florbetapir may involve circular reasoning. Additionally, tracer test-retest reliability might have impacted

results from the current study; however, previous studies have shown that both ^{11}C -PiB [157] and ^{18}F -florbetapir [158] had high test-retest reliability, suggesting that the current results were minimally affected by this phenomenon.

Another limitation to this study is that there is a significant difference in gender balance between the gantenerumab (15 of 41 participants were female, or 37%) and placebo (16 of 25 participants were female, or 64%) arms (Table 4.2). Differences in gender balance between drug arms may contribute to the statistically significant drug effects seen in the gantenerumab versus placebo comparisons. However, initial findings from the DIAN-TU-001 also reported statistically significant drug effects in the gantenerumab versus placebo comparisons for ^{11}C -PiB PET, and in that analysis, baseline demographics were balanced across all drug arms [130]. Naturally, this leaves the possibility of differences in gender balance contributing to the statistically significant drug effect seen with ^{18}F -florbetapir PET; however, a large contribution seems unlikely [159]. Nonetheless, future studies are needed to confirm this.

One limitation for future studies is that while Centiloid provides a way for multiple A β radiotracers to be used in the same study or trial, the results of our simulated clinical trials suggests that type I error is increased when more than one radiotracer is used. Another challenge for future studies is that while ^{18}F -florbetapir has been used in the majority of anti-A β monoclonal antibody trials in AD that incorporate A β PET imaging, using the ^{11}C -PiB radiotracer offers more power to detect A β change in comparison.

Finally, future studies should investigate whether gantenerumab treatment can lead to changes in perfusion to the point of altering A β PET SUVR estimates, as ^{11}C -PiB and ^{18}F -florbetapir may have different sensitivities to changes in perfusion, which may contribute to the

differences observed in annualized rates of SUVR- ^{11}C -PiB and SUVR- ^{18}F -florbetapir change in this study, due to the differences in radiotracer kinetics between ^{11}C -PiB and SUVR- ^{18}F -florbetapir. Nonetheless, the current study shows that the Centiloid method is able to harmonize the different annualized rates of SUVR change between ^{11}C -PiB and ^{18}F -florbetapir in a clinical trial.

In conclusion, gantenerumab treatment induces longitudinal changes in A β PET, and the rates of these longitudinal changes differ significantly between A β radiotracers when expressed in SUVR units. These differences were not seen in the placebo arm, suggesting that A β -removing treatments pose unique challenges when attempting to compare results across different A β radiotracers. Centiloid values derived from PET imaging can harmonize differences between A β radiotracers without losing sensitivity to drug effects. Ultimately, until a consensus emerges on how to harmonize drug effects across radiotracers, and since using multiple radiotracers in the same trial may increase type I error, multi-site studies should consider potential variability due to different radiotracers when interpreting A β PET biomarker data, and if feasible, use a single radiotracer for the best results.

Chapter 5: Future directions

Up to this point, I aimed to ascertain scientific reliability in PET imaging for Alzheimer disease as the technology moves from research to clinical settings, but I always had the benefit of comparing it with an established gold standard:

- Chapter 1 compares tau PET quantification with tau PET visual interpretation
- Chapters 2 and 3 compare tau and A β PET with tau and A β neuropathology
- Chapter 4 compares ^{18}F -florbetapir PET with ^{11}C -PiB

However, these gold standards may not always exist for future research studies. In particular, the gold standard in Chapters 2 and 3 – quantification of neuropathology – was prohibitively time consuming to obtain and could only be performed on a limited subset of participants. Additionally, the data associated with the project described in Chapter 2 took so long to obtain that newer definitions of A β neuropathology arose during the course of the project and it was not feasible to adapt the project to address these developments. To make the quantification of neuropathology more a tractable procedure, new deep learning algorithms for quantifying microscopy images are being developed, which involves segmentation of stained proteins. However, in this situation, no gold standard for segmentation would exist.

Moving forward, it may prove beneficial to adopt a no-gold standard approach to rank the most promising candidate segmentation algorithms for future study. To do so, one approach can be to follow the derivation presented in [160] and assume there exists a linear stochastic relationship between the true quantitative values a_p and experimentally measured values $\hat{a}_{p,k}$, where P is the number of quantitative measurements acquired in the study (for simplicity, let one measurement be obtained for each participant in the study) and K is the number of imaging

methods under consideration (e.g. tau PET visual interpretation guidelines, neuropathology segmentation algorithms, or A β PET radiotracers), such that, a_p is the true quantitative value for the p th participant, and $\hat{a}_{p,k}$ is the experimentally measured quantitative value for the p th participant using the k th method. Furthermore, let this linear stochastic relationship be parameterized by slope u_k , intercept v_k , and a noise term $\varepsilon_{p,k}$ modeled as a random variable sampled from the Gaussian distribution $N(0, \sigma_k^2)$. Thus, this linear stochastic relationship between the true quantitative values a_p and experimentally measured values $\hat{a}_{p,k}$ can be written as

$$\hat{a}_{p,k} = u_k a_p + v_k + \varepsilon_{p,k} \quad (5.1)$$

Furthermore, for a given participant p , this relationship can be written as

$$\begin{bmatrix} \hat{a}_{p,1} \\ \vdots \\ \hat{a}_{p,K} \end{bmatrix} = \begin{bmatrix} u_1 & v_1 & \sigma_1^2 \\ \vdots & \vdots & \vdots \\ u_K & v_K & \sigma_K^2 \end{bmatrix} \begin{bmatrix} a_p \\ 1 \\ 1 \end{bmatrix} \quad (5.2)$$

or simply

$$\hat{A}_p = \Theta A_p \quad (5.3)$$

Additionally, assume that the true quantitative values a_p can be modeled as random variables sampled from a generalized beta distribution. Then the probability distribution function for a_p can be written as

$$p(a_p | \alpha, \beta, g, l) = \frac{(a_p - l)^{(\alpha-1)} (g - a_p)^{(\beta-1)}}{B(\alpha, \beta) (g - l)^{(\alpha+\beta-1)}} \quad (5.4)$$

where $B(\alpha, \beta)$ is the beta function. Let $\Omega = [\alpha, \beta, g, l]$.

The goal now is to estimate the values of all unknown parameters $\{\theta, \Omega\}$ that maximize the probability of observing the measured values \hat{A}_p . Assuming the noise terms $\varepsilon_{p,k}$ are independent for a given value of a_p , the probability density function for the measured values \hat{A}_p can be written as

$$p(\hat{A}_p | \theta, a_p) = \prod_{k=1}^K \frac{1}{\sqrt{2\pi\sigma_k^2}} e^{-\frac{(\hat{a}_{p,k} - u_k a_p - v_k)^2}{2\sigma_k^2}} \quad (5.5)$$

Letting

$$S = \prod_{k=1}^K \frac{1}{\sqrt{2\pi\sigma_k^2}} \quad (5.6)$$

And rewriting gives

$$p(\hat{A}_p | \theta, a_p) = S e^{-\sum_{k=1}^K \frac{(\hat{a}_{p,k} - u_k a_p - v_k)^2}{2\sigma_k^2}} \quad (5.7)$$

Naturally this is not terribly useful as the true quantitative value a_p cannot be known. Continuing to manipulate this equation by multiplying both sides by $p(a_p | \Omega)$ gives

$$p(\hat{A}_p | \theta, a_p) p(a_p | \Omega) = p\left(\frac{\hat{A}_p \theta a_p}{\theta a_p}\right) p\left(\frac{a_p \Omega}{\Omega}\right) = p\left(\frac{\hat{A}_p a_p \theta \Omega}{\theta \Omega}\right) =$$

$$p(\hat{A}_p, a_p | \theta, \Omega) = S p(a_p | \Omega) e^{-\sum_{k=1}^K \frac{(\hat{a}_{p,k} - u_k a_p - v_k)^2}{2\sigma_k^2}} \quad (5.8)$$

Marginalizing over the true quantitative value a_p yields a more useful expression for the probability density for the measured values \hat{A}_p , as it does not depend on knowing the true quantitative value a_p

$$p(\hat{A}_p|\theta, \Omega) = S \int p(a_p|\Omega) e^{-\sum_{k=1}^K \frac{(\hat{a}_{p,k} - u_k a_p - v_k)^2}{2\sigma_k^2}} da_p \quad (5.9)$$

One final assumption is that the P true quantitative values are independent, which allows the likelihood of the set of all measured quantitative values to be written as

$$L(\theta, \Omega|\hat{A}) = p(\hat{A}|\theta, \Omega) = \prod_{p=1}^P p(\hat{A}_p|\theta, \Omega) \quad (5.10)$$

Maximizing this likelihood function will yield the maximum likelihood estimates of θ and Ω , or

$$\{\hat{\theta}, \hat{\Omega}\} = \underset{\theta, \Omega}{\operatorname{argmax}} \ln L(\theta, \Omega|\hat{A}) \quad (5.11)$$

From the estimated parameters (derived using an optimization technique), the noise-to-slope ratio for each imaging method can be written as

$$NSR_k = \frac{\hat{\sigma}_k}{\hat{u}_k} \quad (5.12)$$

It follows that the imaging method with the lowest such noise-to-slope ratio will have the greatest precision among all candidate methods and hold the most promise for future applications in the absence of a gold standard.

The above derivation closely follows the one presented in [160], but it is not the only approach that can be taken. For example, the above derivation models the true quantitative values

a_p as random variables sampled from a generalized beta distribution. The advantage of using the generalized beta distribution over a beta distribution is if a_p is known or assumed to be bounded by a lower bound l and upper bound g . However, if it is known that a_p is bounded by 0 and 1, then the beta distribution is sufficient and the approach from [161] can be used. On the other hand, the approach in [160] is itself not sufficient to handle the random sampling problem. Namely, the participant data available in any given research study is a randomly drawn subset of the entire population. To more appropriately quantify the uncertainty of the noise-to-slope ratio that arises from random sampling, the approach in [162] would be more appropriate. Finally, the approach in [160] makes the assumption that the noise terms $\varepsilon_{p,k}$ are independent; however, the noise between measurements made by k different imaging methods arises during the process of measuring the same underlying true quantitative value a_p and therefore may be correlated. In cases where violating the assumption of independent noise terms can have a significant impact, explicitly modeling correlated noise using a multivariate Gaussian distribution as was done in [163] would be more appropriate.

Considering now the specifics of the problem mentioned earlier (the quantification of neuropathology), results are typically reported as an area fraction, namely a ratio of the area of stained protein to the total area of the tissue sample. Such a ratio is bounded by 0 and 1 and thus using the beta distribution is sufficient for this problem [161]. Next, defining the search space for the parameters of this problem only involves defining the bounds for the shape parameters α and β of the beta distribution and the three slope parameters u_K and three intercept parameters v_k (when assessing $k = 3$ imaging methods for simplicity), and finally the six terms of the noise covariance matrix in the case of correlated noise (three diagonal terms and three off-diagonal

terms) [163]. Assuming that a reasonably stained tissue section should not be completely devoid of the protein of interest ($a_p = 0$), nor completely saturated with the protein of interest ($a_p = 1$), the probability density function

$$p(a_p|\alpha, \beta) = \frac{(a_p)^{(\alpha-1)}(1-a_p)^{(\beta-1)}}{B(\alpha, \beta)} \quad (5.13)$$

should equal 0 when $a_p = 0$ and $a_p = 1$, which requires $\alpha > 1$ and $\beta > 1$. Furthermore, as the distribution of area fractions is typically positively skewed, it can be assumed that $\alpha \leq \beta$. Finally, the $k = 3$ imaging methods to evaluate can be chosen to represent

1. A traditional threshold-based segmentation method. Whether this should be a global threshold for all participants or a participant-specific threshold or even a sample-specific threshold (where there are multiple samples derived from each participant) could be derived from a separate no-gold-standard evaluation of the aforementioned methods.
2. A deep learning segmentation method. As there does not currently exist any deep learning methods for the quantification of neuropathology that has been demonstrated in all proteins of interest across all brain regions of interest (due in part to a complete lack of appropriate training data in this domain), the only appropriate approach is to adapt a pre-trained model.
3. A deep learning segmentation method with manual quality control. As above, no deep learning method exists for quantifying many of the proteins and brain regions in AD. Including this method in the no-gold-standard evaluation will answer the question of whether extensive manual quality control is needed to apply pre-trained models to the current problem.

After implementing these $k = 3$ imaging methods and the no-gold-standard technique, several evaluations should be performed before concluding that the imaging method with the lowest noise-to-slope has superior precision [162].

The first evaluation would be to determine linearity. One of the assumptions made earlier was that there exists a linear stochastic relationship between the true quantitative values a_p and experimentally measured values $\hat{a}_{p,k}$. While this assumption cannot be evaluated, it follows that if such a linear stochastic relationship did exist, then the measured quantitative values $\hat{a}_{p,k}$ for each imaging method should also have linear relationships. Thus, a statistically significant linear correlation coefficient close to 1 should exist between the measured quantitative values $\hat{a}_{p,k}$ for each imaging method. This evaluation can actually be performed before the no-gold-standard technique is applied.

The second evaluation would be to determine uncertainty. As mentioned earlier, the no-gold-standard technique is susceptible to the random sampling problem. A bootstrapping procedure is needed to determine the method with superior precision under uncertainty. A simple procedure for doing so is presented in [162] and repeated here: the vector of quantitative measurements from all P participants across all K imaging methods can be represented as $\{\hat{A}_1 \dots \hat{A}_P\}$. This vector is sampled P times with replacement and evaluated using the no-gold-standard technique to estimate noise-to-slope ratios for all K imaging methods repeated over multiple trials. The imaging method with the lowest noise-to-slope ratio over the majority of trials is then considered to be a candidate for the method with superior precision with a noise-to-slope ratio of NSR_{sp} . If the upper limit of the 95% confidence interval of $\Delta NSR_k = NSR_{sp} - NSR_k$ over

all trials for all k is less than 0, then the candidate method is statistically significantly superior than all other imaging methods.

A third evaluation would be to determine consistency. Without access to a gold standard, an alternative method is needed to evaluate whether the parameters estimated by the no-gold-standard technique are consistent with the quantitative measurements. Instead, this consistency can be measured pairwise between imaging methods. Given the equations relating the measurements of the k th and l th imaging methods to the true quantitative value a_p

$$\hat{a}_{p,k} = u_k a_p + v_k + \varepsilon_{p,k} \quad (5.14)$$

and

$$\hat{a}_{p,l} = u_l a_p + v_l + \varepsilon_{l,k} \quad (5.15)$$

It follows that

$$\hat{a}_{p,k} = \frac{u_k}{u_l} \hat{a}_{p,l} + v_k - \frac{u_k v_l}{u_l} \quad (5.16)$$

and this line should overlap with the actual quantitative measurements such that R^2 is close to 1.

Thus, the imaging method with the lowest noise-to-slope ratio after confirming these three evaluations can be considered to have the greatest precision among all imaging methods tested and used in the absence of a gold standard.

A final note: the current formulation of the no-gold-standard technique typically assumes one quantitative measurement per participant. However, for neuropathology data, it is common to take samples from multiple brain regions, and stain these tissue samples for multiple proteins of

interest. Future work may investigate whether it is beneficial to jointly model multiple samples from each participant.

References

- [1] H. Braak, I. Alafuzoff, T. Arzberger, H. Kretschmar, K. Del Tredici, Staging of Alzheimer disease-associated neurofibrillary pathology using paraffin sections and immunocytochemistry, *Acta Neuropathol.* 112 (2006) 389–404. <https://doi.org/10.1007/s00401-006-0127-z>.
- [2] H. Braak, D.R. Thal, E. Ghebremedhin, K. Del Tredici, Stages of the pathologic process in Alzheimer disease: age categories from 1 to 100 years, *J Neuropathol Exp Neurol.* 70 (2011) 960–969. <https://doi.org/10.1097/NEN.0b013e318232a379>.
- [3] K. Blennow, A. Wallin, H. Agren, C. Spenger, J. Siegfried, E. Vanmechelen, Tau protein in cerebrospinal fluid: a biochemical marker for axonal degeneration in Alzheimer disease?, *Mol Chem Neuropathol.* 26 (1995) 231–245. <https://doi.org/10.1007/BF02815140>.
- [4] D.T. Chien, S. Bahri, A.K. Szardenings, J.C. Walsh, F. Mu, M.-Y. Su, W.R. Shankle, A. Elizarov, H.C. Kolb, Early clinical PET imaging results with the novel PHF-tau radioligand [F-18]-T807, *J Alzheimers Dis.* 34 (2013) 457–468. <https://doi.org/10.3233/JAD-122059>.
- [5] V.L. Villemagne, S. Furumoto, M.T. Fodero-Tavoletti, R.S. Mulligan, J. Hodges, R. Harada, P. Yates, O. Piguet, S. Pejoska, V. Doré, K. Yanai, C.L. Masters, Y. Kudo, C.C. Rowe, N. Okamura, In vivo evaluation of a novel tau imaging tracer for Alzheimer's disease, *Eur J Nucl Med Mol Imaging.* 41 (2014) 816–826. <https://doi.org/10.1007/s00259-013-2681-7>.
- [6] T.J. Betthauser, K.A. Cody, M.D. Zammit, D. Murali, A.K. Converse, T.E. Barnhart, C.K. Stone, H.A. Rowley, S.C. Johnson, B.T. Christian, In Vivo Characterization and Quantification of Neurofibrillary Tau PET Radioligand 18F-MK-6240 in Humans from Alzheimer Disease Dementia to Young Controls, *Journal of Nuclear Medicine.* 60 (2019) 93–99. <https://doi.org/10.2967/jnumed.118.209650>.
- [7] C.R. Jack, H.J. Wiste, S.D. Weigand, T.M. Therneau, V.J. Lowe, D.S. Knopman, J.L. Gunter, M.L. Senjem, D.T. Jones, K. Kantarci, M.M. Machulda, M.M. Mielke, R.O. Roberts, P. Vemuri, D.A. Reyes, R.C. Petersen, Defining imaging biomarker cut-points for brain aging and Alzheimer's disease, *Alzheimers Dement.* 13 (2017) 205–216. <https://doi.org/10.1016/j.jalz.2016.08.005>.
- [8] C.G. Schwarz, T.M. Therneau, S.D. Weigand, J.L. Gunter, V.J. Lowe, S.A. Przybelski, M.L. Senjem, H. Botha, P. Vemuri, K. Kantarci, B.F. Boeve, J.L. Whitwell, K.A. Josephs, R.C. Petersen, D.S. Knopman, C.R. Jack, Selecting software pipelines for change in flortaucipir SUVR: Balancing repeatability and group separation, *NeuroImage.* 238 (2021) 118259. <https://doi.org/10.1016/j.neuroimage.2021.118259>.
- [9] A.H. Boerwinkle, J.K. Wisch, C.D. Chen, B.A. Gordon, O.H. Butt, S.E. Schindler, C. Sutphen, S. Flores, A. Dincer, T.L.S. Benzinger, A.M. Fagan, J.C. Morris, B.M. Ances, Temporal Correlation of CSF and Neuroimaging in the Amyloid-Tau-Neurodegeneration

- Model of Alzheimer Disease, *Neurology*. (2021).
<https://doi.org/10.1212/WNL.00000000000012123>.
- [10] R. La Joie, A. Bejanin, A.M. Fagan, N. Ayakta, S.L. Baker, V. Bourakova, A.L. Boxer, J. Cha, A. Karydas, G. Jerome, A. Maass, A. Mensing, Z.A. Miller, J.P. O’Neil, J. Pham, H.J. Rosen, R. Tsai, A.V. Visani, B.L. Miller, W.J. Jagust, G.D. Rabinovici, Associations between [18F]AV1451 tau PET and CSF measures of tau pathology in a clinical sample, *Neurology*. 90 (2018) e282–e290. <https://doi.org/10.1212/WNL.00000000000004860>.
- [11] M. Bucci, K. Chiotis, A. Nordberg, Alzheimer’s disease profiled by fluid and imaging markers: tau PET best predicts cognitive decline, *Mol Psychiatry*. (2021) 1–11.
<https://doi.org/10.1038/s41380-021-01263-2>.
- [12] R. Ossenkoppele, J. Reimand, R. Smith, A. Leuzy, O. Strandberg, S. Palmqvist, E. Stomrud, H. Zetterberg, Alzheimer’s Disease Neuroimaging Initiative, P. Scheltens, J.L. Dage, F. Bouwman, K. Blennow, N. Mattsson-Carlsson, S. Janelidze, O. Hansson, Tau PET correlates with different Alzheimer’s disease-related features compared to CSF and plasma p-tau biomarkers, *EMBO Mol Med*. 13 (2021) e14398.
<https://doi.org/10.15252/emmm.202114398>.
- [13] S. Weintraub, D. Salmon, N. Mercaldo, S. Ferris, N.R. Graff-Radford, H. Chui, J. Cummings, C. DeCarli, N.L. Foster, D. Galasko, E. Peskind, W. Dietrich, D.L. Beekly, W.A. Kukull, J.C. Morris, The Alzheimer’s Disease Centers’ Uniform Data Set (UDS): The Neuropsychological Test Battery, *Alzheimer Dis Assoc Disord*. 23 (2009) 91–101.
<https://doi.org/10.1097/WAD.0b013e318191c7dd>.
- [14] J.C. Morris, The Clinical Dementia Rating (CDR): Current version and scoring rules, *Neurology*. 43 (1993) 2412–2412-a. <https://doi.org/10.1212/WNL.43.11.2412-a>.
- [15] M.F. Folstein, S.E. Folstein, P.R. McHugh, “Mini-mental state”: A practical method for grading the cognitive state of patients for the clinician, *Journal of Psychiatric Research*. 12 (1975) 189–198. [https://doi.org/10.1016/0022-3956\(75\)90026-6](https://doi.org/10.1016/0022-3956(75)90026-6).
- [16] Y. Su, T.M. Blazey, A.Z. Snyder, M.E. Raichle, D.S. Marcus, B.M. Ances, R.J. Bateman, N.J. Cairns, P. Aldea, L. Cash, J.J. Christensen, K. Friedrichsen, R.C. Hornbeck, A.M. Farrar, C.J. Owen, R. Mayeux, A.M. Brickman, W. Klunk, J.C. Price, P.M. Thompson, B. Ghetti, A.J. Saykin, R.A. Sperling, K.A. Johnson, P.R. Schofield, V. Buckles, J.C. Morris, T.L.S. Benzinger, Dominantly Inherited Alzheimer Network, Partial volume correction in quantitative amyloid imaging, *Neuroimage*. 107 (2015) 55–64.
<https://doi.org/10.1016/j.neuroimage.2014.11.058>.
- [17] Y. Su, G.M. D’Angelo, A.G. Vlassenko, G. Zhou, A.Z. Snyder, D.S. Marcus, T.M. Blazey, J.J. Christensen, S. Vora, J.C. Morris, M.A. Mintun, T.L.S. Benzinger, Quantitative Analysis of PiB-PET with FreeSurfer ROIs, *PLOS ONE*. 8 (2013) e73377.
<https://doi.org/10.1371/journal.pone.0073377>.

- [18] B. Fischl, FreeSurfer, *NeuroImage*. 62 (2012) 774–781.
<https://doi.org/10.1016/j.neuroimage.2012.01.021>.
- [19] Y. Su, S. Flores, R.C. Hornbeck, B. Speidel, A.G. Vlassenko, B.A. Gordon, R.A. Koeppe, W.E. Klunk, C. Xiong, J.C. Morris, T.L.S. Benzinger, Utilizing the Centiloid scale in cross-sectional and longitudinal PiB PET studies, *Neuroimage Clin*. 19 (2018) 406–416.
<https://doi.org/10.1016/j.nicl.2018.04.022>.
- [20] W.E. Klunk, R.A. Koeppe, J.C. Price, T.L. Benzinger, M.D. Devous, W.J. Jagust, K.A. Johnson, C.A. Mathis, D. Minhas, M.J. Pontecorvo, C.C. Rowe, D.M. Skovronsky, M.A. Mintun, The Centiloid Project: standardizing quantitative amyloid plaque estimation by PET, *Alzheimers Dement*. 11 (2015) 1-15.e1–4. <https://doi.org/10.1016/j.jalz.2014.07.003>.
- [21] X. Zhu, V. Melnykov, Manly transformation in finite mixture modeling, *Computational Statistics & Data Analysis*. 121 (2018) 190–208.
<https://doi.org/10.1016/j.csda.2016.01.015>.
- [22] R Core Team, R: A Language and Environment for Statistical Computing, R Foundation for Statistical Computing, Vienna, Austria, 2021. <https://www.R-project.org/>.
- [23] J.W. Vogel, A.L. Young, N.P. Oxtoby, R. Smith, R. Ossenkoppele, O.T. Strandberg, R. La Joie, L.M. Aksam, M.J. Grothe, Y. Iturria-Medina, M.J. Pontecorvo, M.D. Devous, G.D. Rabinovici, D.C. Alexander, C.H. Lyoo, A.C. Evans, O. Hansson, Four distinct trajectories of tau deposition identified in Alzheimer’s disease, *Nat Med*. 27 (2021) 871–881.
<https://doi.org/10.1038/s41591-021-01309-6>.
- [24] S.L. Baker, T.M. Harrison, A. Maass, R.L. Joie, W.J. Jagust, Effect of Off-Target Binding on 18F-Flortaucipir Variability in Healthy Controls Across the Life Span, *Journal of Nuclear Medicine*. 60 (2019) 1444–1451. <https://doi.org/10.2967/jnumed.118.224113>.
- [25] R. Smith, O. Strandberg, A. Leuzy, T.J. Betthausen, S.C. Johnson, J.B. Pereira, O. Hansson, Sex differences in off-target binding using tau positron emission tomography, *Neuroimage Clin*. 31 (2021) 102708. <https://doi.org/10.1016/j.nicl.2021.102708>.
- [26] C.M. Moloney, S.A. Labuzan, J.E. Crook, H. Siddiqui, M. Castanedes-Casey, C. Lachner, R.C. Petersen, R. Duara, N.R. Graff-Radford, D.W. Dickson, M.M. Mielke, M.E. Murray, Phosphorylated tau sites that are elevated in Alzheimer’s disease fluid biomarkers are visualized in early neurofibrillary tangle maturity levels in the post mortem brain, *Alzheimer’s & Dementia*. n/a (n.d.). <https://doi.org/10.1002/alz.12749>.
- [27] M. Wennström, S. Janelidze, K.P.R. Nilsson, G.E. Serrano, T.G. Beach, J.L. Dage, O. Hansson, The Netherlands Brain Bank, Cellular localization of p-tau217 in brain and its association with p-tau217 plasma levels, *Acta Neuropathologica Communications*. 10 (2022) 3. <https://doi.org/10.1186/s40478-021-01307-2>.

- [28] N.R. Barthélemy, K. Horie, C. Sato, R.J. Bateman, Blood plasma phosphorylated-tau isoforms track CNS change in Alzheimer's disease, *Journal of Experimental Medicine*. 217 (2020) e20200861. <https://doi.org/10.1084/jem.20200861>.
- [29] S. Janelidze, N. Mattsson, S. Palmqvist, R. Smith, T.G. Beach, G.E. Serrano, X. Chai, N.K. Proctor, U. Eichenlaub, H. Zetterberg, K. Blennow, E.M. Reiman, E. Stomrud, J.L. Dage, O. Hansson, Plasma P-tau181 in Alzheimer's disease: relationship to other biomarkers, differential diagnosis, neuropathology and longitudinal progression to Alzheimer's dementia, *Nat Med*. 26 (2020) 379–386. <https://doi.org/10.1038/s41591-020-0755-1>.
- [30] M. Suárez-Calvet, T.K. Karikari, N.J. Ashton, J.L. Rodríguez, M. Milà-Alomà, J.D. Gispert, G. Salvadó, C. Minguillon, K. Fauria, M. Shekari, O. Grau-Rivera, E.M. Arenaza-Urquijo, A. Sala-Vila, G. Sánchez-Benavides, J.M. González-de-Echávarri, G. Kollmorgen, E. Stoops, E. Vanmechelen, H. Zetterberg, K. Blennow, J.L. Molinuevo, Novel tau biomarkers phosphorylated at T181, T217 or T231 rise in the initial stages of the preclinical Alzheimer's continuum when only subtle changes in A β pathology are detected, *EMBO Molecular Medicine*. 12 (2020) e12921. <https://doi.org/10.15252/emmm.202012921>.
- [31] J.L. Shuping, D.C. Matthews, K. Adamczuk, D. Scott, C.C. Rowe, W.C. Kreisl, S.C. Johnson, A.S. Lukic, K.A. Johnson, P. Rosa-Neto, R.D. Andrews, K. Van Laere, L. Cordes, L. Ward, C.L. Wilde, J. Barakos, D.D. Purcell, D.P. Devanand, Y. Stern, J.A. Luchsinger, C. Sur, J.C. Price, A.M. Brickman, W.E. Klunk, A.L. Boxer, S.S. Mathotaarachchi, P.J. Lao, J.L. Evelhoch, Development, initial validation, and application of a visual read method for [18F]MK-6240 tau PET, *Alzheimer's & Dementia: Translational Research & Clinical Interventions*. 9 (2023) e12372. <https://doi.org/10.1002/trc2.12372>.
- [32] M.J. Pontecorvo, M.D. Devous, I. Kennedy, M. Navitsky, M. Lu, N. Galante, S. Salloway, P.M. Doraiswamy, S. Southeikal, A.K. Arora, A. McGeehan, N.C. Lim, H. Xiong, S.P. Truocchio, A.D. Joshi, S. Shcherbinin, B. Teske, A.S. Fleisher, M.A. Mintun, A multicentre longitudinal study of flortaucipir (18F) in normal ageing, mild cognitive impairment and Alzheimer's disease dementia, *Brain*. 142 (2019) 1723. <https://doi.org/10.1093/brain/awz090>.
- [33] D.T. Chien, A.K. Szardenings, S. Bahri, J.C. Walsh, F. Mu, C. Xia, W.R. Shankle, A.J. Lerner, M.Y. Su, A. Elizarov, H.C. Kolb, Early clinical PET imaging results with the novel PHF-tau radioligand [F18]-T808, *Journal of Alzheimer's Disease*. 38 (2014) 171–184. <https://doi.org/10.3233/JAD-130098>.
- [34] M. Schöll, R. Ossenkoppele, O. Strandberg, S. Palmqvist, J. Jögi, T. Ohlsson, R. Smith, O. Hansson, Distinct 18F-AV-1451 tau PET retention patterns in early- and late-onset Alzheimer's disease, *Brain*. 140 (2017) 2286–2294. <https://doi.org/10.1093/brain/awx171>.
- [35] B.A. Gordon, T.M. Blazey, J. Christensen, A. Dincer, S. Flores, S. Keefe, C. Chen, Y. Su, E.M. McDade, G. Wang, Y. Li, J. Hassenstab, A. Aschenbrenner, R. Hornbeck, C.R. Jack, B.M. Ances, S.B. Berman, J.R. Brosch, D. Galasko, S. Gauthier, J.J. Lah, M. Masellis, C.H. Van Dyck, M.A. Mintun, G. Klein, S. Ristic, N.J. Cairns, D.S. Marcus, C. Xiong, D.M.

- Holtzman, M.E. Raichle, J.C. Morris, R.J. Bateman, T.L.S. Benzinger, Tau PET in autosomal dominant Alzheimer's disease: Relationship with cognition, dementia and other biomarkers, *Brain*. 142 (2019) 1063–1076. <https://doi.org/10.1093/brain/awz019>.
- [36] R. Smith, M. Wibom, D. Pawlik, E. Englund, O. Hansson, Correlation of in Vivo [¹⁸F]Flortaucipir with Postmortem Alzheimer Disease Tau Pathology, *JAMA Neurology*. 76 (2019) 310–317. <https://doi.org/10.1001/jamaneurol.2018.3692>.
- [37] J.M. Ringman, K.H. Gylys, L.D. Medina, M. Fox, V. Kepe, D.L. Flores, L.G. Apostolova, J.R. Barrio, G. Small, D.H. Silverman, E. Siu, S. Cederbaum, S. Hecimovic, M. Malnar, S. Chakraverty, A.M. Goate, T.D. Bird, J.B. Leverenz, Biochemical, neuropathological, and neuroimaging characteristics of early-onset Alzheimer's disease due to a novel PSEN1 mutation, *Neuroscience Letters*. 487 (2011) 287–292. <https://doi.org/10.1016/j.neulet.2010.10.039>.
- [38] J.M. Ringman, A. Goate, C.L. Masters, N.J. Cairns, A. Danek, N. Graff-Radford, B. Ghetti, J.C. Morris, Genetic Heterogeneity in Alzheimer Disease and Implications for Treatment Strategies, *Current Neurology and Neuroscience Reports*. 14 (2014). <https://doi.org/10.1007/s11910-014-0499-8>.
- [39] A.P. Badhwar, G.P. McFall, S. Sapkota, S.E. Black, H. Chertkow, S. Duchesne, M. Masellis, L. Li, R.A. Dixon, P. Bellec, A multiomics approach to heterogeneity in Alzheimer's disease: focused review and roadmap, *Brain : A Journal of Neurology*. 143 (2020) 1315–1331. <https://doi.org/10.1093/brain/awz384>.
- [40] T.J. Montine, C.H. Phelps, T.G. Beach, E.H. Bigio, N.J. Cairns, D.W. Dickson, C. Duyckaerts, M.P. Frosch, E. Masliah, S.S. Mirra, P.T. Nelson, J.A. Schneider, D.R. Thal, J.Q. Trojanowski, H. V. Vinters, B.T. Hyman, National institute on aging-Alzheimer's association guidelines for the neuropathologic assessment of Alzheimer's disease: A practical approach, *Acta Neuropathologica*. 123 (2012) 1–11. <https://doi.org/10.1007/s00401-011-0910-3>.
- [41] N.J. Cairns, R.J. Perrin, E.E. Franklin, D. Carter, B. Vincent, M. Xie, R.J. Bateman, T. Benzinger, K. Friedrichsen, W.S. Brooks, G.M. Halliday, C. McLean, B. Ghetti, J.C. Morris, Neuropathologic assessment of participants in two multi-center longitudinal observational studies: The Alzheimer Disease Neuroimaging Initiative (ADNI) and the Dominantly Inherited Alzheimer Network (DIAN), *Neuropathology*. 35 (2015) 390–400. <https://doi.org/10.1111/neup.12205>.
- [42] Y. Su, G.M. D'Angelo, A.G. Vlassenko, G. Zhou, A.Z. Snyder, D.S. Marcus, T.M. Blazey, J.J. Christensen, S. Vora, J.C. Morris, M.A. Mintun, T.L.S. Benzinger, Quantitative Analysis of PiB-PET with FreeSurfer ROIs, *PLoS ONE*. 8 (2013) e73377. <https://doi.org/10.1371/journal.pone.0073377>.
- [43] J.C. Morris, The clinical dementia rating (cdr): Current version and scoring rules, *Neurology*. 43 (1993) 2412–2414. <https://doi.org/10.1212/wnl.43.11.2412-a>.

- [44] Y. Su, S. Flores, G. Wang, R.C. Hornbeck, B. Speidel, N. Joseph-Mathurin, A.G. Vlassenko, B.A. Gordon, R.A. Koeppe, W.E. Klunk, C.R. Jack, M.R. Farlow, S. Salloway, B.J. Snider, S.B. Berman, E.D. Roberson, J. Brosch, I. Jimenez-Velazques, C.H. van Dyck, D. Galasko, S.H. Yuan, S. Jayadev, L.S. Honig, S. Gauthier, G.Y.R. Hsiung, M. Masellis, W.S. Brooks, M. Fulham, R. Clarnette, C.L. Masters, D. Wallon, D. Hannequin, B. Dubois, J. Pariente, R. Sanchez-Valle, C. Mummery, J.M. Ringman, M. Bottlaender, G. Klein, S. Milosavljevic-Ristic, E. McDade, C. Xiong, J.C. Morris, R.J. Bateman, T.L.S. Benzinger, Comparison of Pittsburgh compound B and florbetapir in cross-sectional and longitudinal studies, *Alzheimer's and Dementia: Diagnosis, Assessment and Disease Monitoring*. 11 (2019) 180–190. <https://doi.org/10.1016/j.dadm.2018.12.008>.
- [45] B. Fischl, D.H. Salat, E. Busa, M. Albert, M. Dieterich, C. Haselgrove, A. Van Der Kouwe, R. Killiany, D. Kennedy, S. Klaveness, A. Montillo, N. Makris, B. Rosen, A.M. Dale, Whole brain segmentation: Automated labeling of neuroanatomical structures in the human brain, *Neuron*. 33 (2002) 341–355. [https://doi.org/10.1016/S0896-6273\(02\)00569-X](https://doi.org/10.1016/S0896-6273(02)00569-X).
- [46] J.M. Ringman, S. Monsell, D.W. Ng, Y. Zhou, A. Nguyen, G. Coppola, V. Van Berlo, M.F. Mendez, S. Tung, S. Weintraub, M.-M. Mesulam, E.H. Bigio, D.R. Gitelman, A.O. Fisher-Hubbard, R.L. Albin, H. V. Vinters, Neuropathology of Autosomal Dominant Alzheimer Disease in the National Alzheimer Coordinating Center Database, *Journal of Neuropathology and Experimental Neurology*. 75 (2016) 284. <https://doi.org/10.1093/JNEN/NLV028>.
- [47] G. Lace, G.M. Savva, G. Forster, R. de Silva, C. Brayne, F.E. Matthews, J.J. Barclay, L. Dakin, P.G. Ince, S.B. Wharton, on behalf of MRC-CFAS, Hippocampal tau pathology is related to neuroanatomical connections: an ageing population-based study, *Brain*. 132 (2009) 1324–1334. <https://doi.org/10.1093/brain/awp059>.
- [48] H. Braak, E. Braak, Neuropathological staging of Alzheimer-related changes, *Acta Neuropathologica*. 82 (1991) 239–259. <https://doi.org/10.1007/BF00308809>.
- [49] M.J. Pontecorvo, M.D. Devous, M. Navitsky, M. Lu, S. Salloway, F.W. Schaerf, D. Jennings, A.K. Arora, A. McGeehan, N.C. Lim, H. Xiong, A.D. Joshi, A. Siderowf, M.A. Mintun, Relationships between flortaucipir PET tau binding and amyloid burden, clinical diagnosis, age and cognition, *Brain*. 140 (2017) 748–763. <https://doi.org/10.1093/brain/aww334>.
- [50] R. Ossenkoppele, D.R. Schonhaut, M. Schöll, S.N. Lockhart, N. Ayakta, S.L. Baker, J.P. O'Neil, M. Janabi, A. Lazaris, A. Cantwell, J. Vogel, M. Santos, Z.A. Miller, B.M. Bettcher, K.A. Vossell, J.H. Kramer, M.L. Gorno-Tempini, B.L. Miller, W.J. Jagust, G.D. Rabinovici, Tau PET patterns mirror clinical and neuroanatomical variability in Alzheimer's disease, *Brain*. 139 (2016) 1551–1567. <https://doi.org/10.1093/brain/aww027>.
- [51] R. La Joie, A. V. Visani, S.L. Baker, J.A. Brown, V. Bourakova, J. Cha, K. Chaudhary, L. Edwards, L. Iaccarino, M. Janabi, O.H. Lesman-Segev, Z.A. Miller, D.C. Perry, J.P.

- O'Neil, J. Pham, J.C. Rojas, H.J. Rosen, W.W. Seeley, R.M. Tsai, B.L. Miller, W.J. Jagust, G.D. Rabinovici, Prospective longitudinal atrophy in Alzheimer's disease correlates with the intensity and topography of baseline tau-PET, *Science Translational Medicine*. 12 (2020). <https://doi.org/10.1126/scitranslmed.aau5732>.
- [52] C. Busch, J. Bohl, T.G. Ohm, Spatial, temporal and numeric analysis of Alzheimer changes in the nucleus coeruleus, *Neurobiology of Aging*. 18 (1997) 401–406. [https://doi.org/10.1016/S0197-4580\(97\)00035-3](https://doi.org/10.1016/S0197-4580(97)00035-3).
- [53] H. Braak, D.R. Thal, E. Ghebremedhin, K. Del Tredici, Stages of the Pathologic Process in Alzheimer Disease: Age Categories From 1 to 100 Years, *Journal of Neuropathology & Experimental Neurology*. 70 (2011) 960–969. <https://doi.org/10.1097/NEN.0b013e318232a379>.
- [54] J.F. Crary, J.Q. Trojanowski, J.A. Schneider, J.F. Abisambra, E.L. Abner, I. Alafuzoff, S.E. Arnold, J. Attems, T.G. Beach, E.H. Bigio, N.J. Cairns, D.W. Dickson, M. Gearing, L.T. Grinberg, P.R. Hof, B.T. Hyman, K. Jellinger, G.A. Jicha, G.G. Kovacs, D.S. Knopman, J. Kofler, W.A. Kukull, I.R. Mackenzie, E. Masliah, A. McKee, T.J. Montine, M.E. Murray, J.H. Neltner, I. Santa-Maria, W.W. Seeley, A. Serrano-Pozo, M.L. Shelanski, T. Stein, M. Takao, D.R. Thal, J.B. Toledo, J.C. Troncoso, J.P. Vonsattel, C.L. White, T. Wisniewski, R.L. Woltjer, M. Yamada, P.T. Nelson, Primary age-related tauopathy (PART): a common pathology associated with human aging, *Acta Neuropathologica*. 128 (2014) 755–766. <https://doi.org/10.1007/s00401-014-1349-0>.
- [55] W.E. Klunk, H. Engler, A. Nordberg, Y. Wang, G. Blomqvist, D.P. Holt, M. Bergström, I. Savitcheva, G.F. Huang, S. Estrada, B. Ausén, M.L. Debnath, J. Barletta, J.C. Price, J. Sandell, B.J. Lopresti, A. Wall, P. Koivisto, G. Antoni, C.A. Mathis, B. Långström, Imaging Brain Amyloid in Alzheimer's Disease with Pittsburgh Compound-B, *Annals of Neurology*. 55 (2004) 306–319. <https://doi.org/10.1002/ana.20009>.
- [56] A. Lockhart, J.R. Lamb, T. Osredkar, L.I. Sue, J.N. Joyce, L. Ye, V. Libri, D. Leppert, T.G. Beach, PIB is a non-specific imaging marker of amyloid-beta (A β) peptide-related cerebral amyloidosis, *Brain*. 130 (2007) 2607–2615. <https://doi.org/10.1093/brain/awm191>.
- [57] P.T. Nelson, I. Alafuzoff, E.H. Bigio, C. Bouras, H. Braak, N.J. Cairns, R.J. Castellani, B.J. Crain, P. Davies, K. Del Tredici, C. Duyckaerts, M.P. Frosch, V. Haroutunian, P.R. Hof, C.M. Hulette, B.T. Hyman, T. Iwatsubo, K.A. Jellinger, G.A. Jicha, E. Kövari, W.A. Kukull, J.B. Leverenz, S. Love, I.R. MacKenzie, D.M. Mann, E. Masliah, A.C. McKee, T.J. Montine, J.C. Morris, J.A. Schneider, J.A. Sonnen, D.R. Thal, J.Q. Trojanowski, J.C. Troncoso, T. Wisniewski, R.L. Woltjer, T.G. Beach, Correlation of alzheimer disease neuropathologic changes with cognitive status: A review of the literature, *Journal of Neuropathology and Experimental Neurology*. 71 (2012) 362–381. <https://doi.org/10.1097/NEN.0b013e31825018f7>.

- [58] T.C. Dickson, J.C. Vickers, The morphological phenotype of β -amyloid plaques and associated neuritic changes in Alzheimer's disease, *Neuroscience*. 105 (2001) 99–107. [https://doi.org/10.1016/S0306-4522\(01\)00169-5](https://doi.org/10.1016/S0306-4522(01)00169-5).
- [59] R.B. Knowles, C. Wyart, S. V. Buldyrev, L. Cruz, B. Urbanc, M.E. Hasselmo, H.E. Stanley, B.T. Hyman, Plaque-induced neurite abnormalities: Implications for disruption of neural networks in Alzheimer's disease, *Proceedings of the National Academy of Sciences of the United States of America*. 96 (1999) 5274–5279. <https://doi.org/10.1073/pnas.96.9.5274>.
- [60] J.L. Price, D.W. McKeel, V.D. Buckles, C.M. Roe, C. Xiong, M. Grundman, L.A. Hansen, R.C. Petersen, J.E. Parisi, D.W. Dickson, C.D. Smith, D.G. Davis, F.A. Schmitt, W.R. Markesbery, J. Kaye, R. Kurlan, C. Hulette, B.F. Kurland, R. Higdon, W. Kukull, J.C. Morris, Neuropathology of nondemented aging: Presumptive evidence for preclinical Alzheimer disease, *Neurobiology of Aging*. 30 (2009) 1026–1036. <https://doi.org/10.1016/j.neurobiolaging.2009.04.002>.
- [61] R.J. Bateman, P.S. Aisen, B. De Strooper, N.C. Fox, C.A. Lemere, J.M. Ringman, S. Salloway, R.A. Sperling, M. Windisch, C. Xiong, Autosomal-dominant Alzheimer's disease: A review and proposal for the prevention of Alzheimer's disease, *Alzheimer's Research and Therapy*. 2 (2011). <https://doi.org/10.1186/alzrt59>.
- [62] D.R. Thal, U. Rüb, M. Orantes, H. Braak, Phases of A β -deposition in the human brain and its relevance for the development of AD, *Neurology*. 58 (2002) 1791–1800. <https://doi.org/10.1212/WNL.58.12.1791>.
- [63] S.S. Mirra, A. Heyman, D. McKeel, S.M. Sumi, B.J. Crain, L.M. Brownlee, F.S. Vogel, J.P. Hughes, G. van Belle, L. Berg, M.J. Ball, L.M. Bierer, D. Claasen, L.R. Hansen, M. Hart, J. Hedreen, B. Baltimore, V. Hen Derson, B.T. Hyman, C. Joachim, W. Mark-Esbey, A.J. Mar Tinez, A. McKee, C. Miller, J. Moossy, D. Nochlin, D. Perl, C. Petito, G.R. Rao, R.L. Schelper, U. Slager, R.D. Terry, The consortium to establish a registry for Alzheimer's disease (CERAD). Part II. Standardization of the neuropathologic assessment of Alzheimer's disease, *Neurology*. 41 (1991) 479–486. <https://doi.org/10.1212/wnl.41.4.479>.
- [64] B.T. Hyman, C.H. Phelps, T.G. Beach, E.H. Bigio, N.J. Cairns, M.C. Carrillo, D.W. Dickson, C. Duyckaerts, M.P. Frosch, E. Masliah, S.S. Mirra, P.T. Nelson, J.A. Schneider, D.R. Thal, B. Thies, J.Q. Trojanowski, H. V. Vinters, T.J. Montine, National Institute on Aging-Alzheimer's Association guidelines for the neuropathologic assessment of Alzheimer's disease, *Alzheimer's and Dementia*. 8 (2012) 1–13. <https://doi.org/10.1016/j.jalz.2011.10.007>.
- [65] W.E. Klunk, R.A. Koeppe, J.C. Price, T.L. Benzinger, M.D. Devous, W.J. Jagust, K.A. Johnson, C.A. Mathis, D. Minhas, M.J. Pontecorvo, C.C. Rowe, D.M. Skovronsky, M.A. Mintun, The Centiloid project: Standardizing quantitative amyloid plaque estimation by PET, *Alzheimer's and Dementia*. 11 (2015) 1-15.e4. <https://doi.org/10.1016/j.jalz.2014.07.003>.

- [66] M.D. Ikonomovic, W.E. Klunk, E.E. Abrahamson, C.A. Mathis, J.C. Price, N.D. Tsopelas, B.J. Lopresti, S. Ziolko, W. Bi, W.R. Paljug, M.L. Debnath, C.E. Hope, B.A. Isanski, R.L. Hamilton, S.T. DeKosky, Post-mortem correlates of in vivo PiB-PET amyloid imaging in a typical case of Alzheimer's disease, *Brain*. 131 (2008) 1630–1645.
<https://doi.org/10.1093/brain/awn016>.
- [67] N.A. Verwey, J.J.M. Hoozemans, C. Korth, M.R. Van Royen, I. Prikulis, D. Wouters, H.A.M. Twaalfhoven, E.S. Van Haastert, D. Schenk, P. Scheltens, A.J.M. Rozemuller, M.A. Blankenstein, R. Veerhuis, Immunohistochemical characterization of novel monoclonal antibodies against the N-terminus of amyloid β -peptide, *Amyloid*. 20 (2013) 179–187. <https://doi.org/10.3109/13506129.2013.797389>.
- [68] J.C. Morris, P.S. Aisen, R.J. Bateman, T.L. Benzinger, N.J. Cairns, A.M. Fagan, B. Ghetti, A.M. Goate, D.M. Holtzman, W.E. Klunk, E. McDade, D.S. Marcus, R.N. Martins, C.L. Masters, R. Mayeux, A. Oliver, K. Quaid, J. M Ringman, M.N. Rossor, S. Salloway, P.R. Schofield, N.J. Selsor, R.A. Sperling, M.W. Weiner, C. Xiong, K.L. Moulder, V.D. Buckles, Developing an international network for Alzheimer's research: the Dominantly Inherited Alzheimer Network, *Clinical Investigation*. 2 (2012) 975–984.
<https://doi.org/10.4155/cli.12.93>.
- [69] T.L.S. Benzinger, T. Blazey, C.R. Jack, R.A. Koeppe, Y. Su, C. Xiong, M.E. Raichle, A.Z. Snyder, B.M. Ances, R.J. Bateman, N.J. Cairns, A.M. Fagan, A. Goate, D.S. Marcus, P.S. Aisen, J.J. Christensen, L. Ercole, R.C. Hornbeck, A.M. Farrar, P. Aldea, M.S. Jasielec, C.J. Owen, X. Xie, R. Mayeux, A. Brickman, E. McDade, W. Klunk, C.A. Mathis, J. Ringman, P.M. Thompson, B. Ghetti, A.J. Saykin, R.A. Sperling, K.A. Johnson, S. Salloway, S. Correia, P.R. Schofield, C.L. Masters, C. Rowe, V.L. Villemagne, R. Martins, S. Ourselin, M.N. Rossor, N.C. Fox, D.M. Cash, M.W. Weiner, D.M. Holtzman, V.D. Buckles, K. Moulder, J.C. Morris, Regional variability of imaging biomarkers in autosomal dominant Alzheimer's disease, *Proceedings of the National Academy of Sciences of the United States of America*. 110 (2013) E4502–E4509.
<https://doi.org/10.1073/pnas.1317918110>.
- [70] D.F. Wong, P.B. Rosenberg, Y. Zhou, A. Kumar, V. Rayment, H.T. Ravert, R.F. Dannals, A. Nandi, J.R. Brašić, W. Ye, J. Hilton, C. Lyketsos, H.F. Kung, A.D. Joshi, D.M. Skovronsky, M.J. Pontecorvo, In vivo imaging of amyloid deposition in Alzheimer disease using the radioligand 18F-AV-45 (flobetapir F 18), *Journal of Nuclear Medicine*. 51 (2010) 913–920. <https://doi.org/10.2967/jnumed.109.069088>.
- [71] C.D. Chen, T.R. Holden, B.A. Gordon, E.E. Franklin, Y. Li, D.W. Coble, H. Luo, R.J. Bateman, B.M. Ances, R.J. Perrin, T.L.S. Benzinger, N.J. Cairns, J.C. Morris, Ante- and postmortem tau in autosomal dominant and late-onset Alzheimer's disease, *Annals of Clinical and Translational Neurology*. 7 (2020) 2475–2480.
<https://doi.org/10.1002/acn3.51237>.

- [72] Y. Su, S. Flores, R.C. Hornbeck, B. Speidel, A.G. Vlassenko, B.A. Gordon, R.A. Koeppe, W.E. Klunk, C. Xiong, J.C. Morris, T.L.S. Benzinger, Utilizing the Centiloid scale in cross-sectional and longitudinal PiB PET studies, *NeuroImage: Clinical*. 19 (2018) 406–416. <https://doi.org/10.1016/j.nicl.2018.04.022>.
- [73] Y. Su, T.M. Blazey, A.Z. Snyder, M.E. Raichle, D.S. Marcus, B.M. Ances, R.J. Bateman, N.J. Cairns, P. Aldea, L. Cash, J.J. Christensen, K. Friedrichsen, R.C. Hornbeck, A.M. Farrar, C.J. Owen, R. Mayeux, A.M. Brickman, W. Klunk, J.C. Price, P.M. Thompson, B. Ghetti, A.J. Saykin, R.A. Sperling, K.A. Johnson, P.R. Schofield, V. Buckles, J.C. Morris, T.L.S. Benzinger, Partial volume correction in quantitative amyloid imaging, *NeuroImage*. 107 (2015) 55–64. <https://doi.org/10.1016/j.neuroimage.2014.11.058>.
- [74] S. van Buuren, K. Groothuis-Oudshoorn, mice: Multivariate imputation by chained equations in R, *Journal of Statistical Software*. 45 (2011) 1–67. <https://doi.org/10.18637/jss.v045.i03>.
- [75] B. Efron, Size, power and false discovery rates, *Annals of Statistics*. 35 (2007) 1351–1377. <https://doi.org/10.1214/009053606000001460>.
- [76] W.E. Klunk, B.J. Lopresti, M.D. Ikonomovic, I.M. Lefterov, R.P. Koldamova, E.E. Abrahamson, M.L. Debnath, D.P. Holt, G.F. Huang, L. Shao, S.T. DeKosky, J.C. Price, C.A. Mathis, Binding of the positron emission tomography tracer Pittsburgh Compound-B reflects the amount of amyloid- β in Alzheimer's Disease brain but not in transgenic mouse brain, *Journal of Neuroscience*. 25 (2005) 10598–10606. <https://doi.org/10.1523/JNEUROSCI.2990-05.2005>.
- [77] C.A. Davies, D.M.A. Mann, Is the “preamyloid” of diffuse plaques in Alzheimer's disease really nonfibrillar?, *American Journal of Pathology*. 143 (1993) 1594–1605.
- [78] B.N.M. Van Berckel, R. Ossenkoppele, N. Tolboom, M. Yaquib, J.C. Foster-Dingley, A.D. Windhorst, P. Scheltens, A.A. Lammertsma, R. Boellaard, Longitudinal amyloid imaging using 11C-PiB: Methodologic considerations, *Journal of Nuclear Medicine*. 54 (2013) 1570–1576. <https://doi.org/10.2967/jnumed.112.113654>.
- [79] V.J. Lowe, E.S. Lundt, M.L. Senjem, C.G. Schwarz, H.K. Min, S.A. Przybelski, K. Kantarci, D. Knopman, R.C. Petersen, C.R. Jack, White matter reference region in PET studies of 11C-Pittsburgh compound B uptake: Effects of age and amyloid- β deposition, *Journal of Nuclear Medicine*. 59 (2018) 1583–1589. <https://doi.org/10.2967/jnumed.117.204271>.
- [80] J. Koivunen, A. Verkkoniemi, S. Aalto, A. Paetau, J.P. Ahonen, M. Viitanen, K. Någren, J. Rokka, M. Haaparanta, H. Kalimo, J.O. Rinne, PET amyloid ligand [11C]PIB uptake shows predominantly striatal increase in variant Alzheimer's disease, *Brain*. 131 (2008) 1845–1853. <https://doi.org/10.1093/brain/awn107>.
- [81] A.M. Remes, L. Laru, H. Tuominen, S. Aalto, N. Kemppainen, H. Mononen, K. Någren, R. Parkkola, J.O. Rinne, Carbon 11-labeled Pittsburgh Compound B positron emission

- tomographic amyloid imaging in patients with APP locus duplication, *Archives of Neurology*. 65 (2008) 540–544. <https://doi.org/10.1001/archneur.65.4.540>.
- [82] J. Theuns, E. Marjaux, M. Vandenbulcke, K. Van Laere, S. Kumar-Singh, G. Bormans, N. Brouwers, M. Van Den Broeck, K. Vennekens, E. Corsmit, M. Cruts, B. De Strooper, C. Van Broeckhoven, R. Vandenberghe, Alzheimer dementia caused by a novel mutation located in the APP C-terminal intracytosolic fragment, *Human Mutation*. 27 (2006) 888–896. <https://doi.org/10.1002/humu.20402>.
- [83] T. Tomiyama, T. Nagata, H. Shimada, R. Teraoka, A. Fukushima, H. Kanemitsu, H. Takuma, R. Kuwano, M. Imagawa, S. Ataka, Y. Wada, E. Yoshioka, T. Nishizaki, Y. Watanabe, H. Mori, A new amyloid β variant favoring oligomerization in Alzheimer's-type dementia, *Annals of Neurology*. 63 (2008) 377–387. <https://doi.org/10.1002/ana.21321>.
- [84] M. Schöll, A. Wall, S. Thordardottir, D. Ferreira, N. Bogdanovic, B. Långström, O. Almkvist, C. Graff, A. Nordberg, Low PiB PET retention in presence of pathologic CSF biomarkers in Arctic APP mutation carriers, *Neurology*. 79 (2012) 229–236. <https://doi.org/10.1212/WNL.0b013e31825fdf18>.
- [85] A.J. Larner, M. Doran, Clinical phenotypic heterogeneity of Alzheimer's disease associated with mutations of the presenilin-1 gene, *Journal of Neurology*. 253 (2006) 139–158. <https://doi.org/10.1007/s00415-005-0019-5>.
- [86] D. Sepulveda-Falla, L. Chavez-Gutierrez, E. Portelius, J.I. Véléz, A. Barrera-Ocampo, F. Dinkel, C. Hagel, B. Puig, C. Mastronardi, F. Lopera, K. Blennow, M. Arcos-Burgos, B. de Strooper, M. Glatzel, A multifactorial model of pathology for age of onset variability in Familial Alzheimer's disease, *Sci Transl Med*. revised ve (2018). <https://doi.org/10.1007/s00401-020-02249-0>.
- [87] M. Tang, D.C. Ryman, E. McDade, M.S. Jasielec, V.D. Buckles, N.J. Cairns, A.M. Fagan, A. Goate, D.S. Marcus, C. Xiong, R.F. Allegri, J.P. Chhatwal, A. Danek, M.R. Farlow, N.C. Fox, B. Ghetti, N.R. Graff-Radford, C. Laske, R.N. Martins, C.L. Masters, R.P. Mayeux, J.M. Ringman, M.N. Rossor, S.P. Salloway, P.R. Schofield, J.C. Morris, R.J. Bateman, Neurological manifestations of autosomal dominant familial Alzheimer's disease: a comparison of the published literature with the Dominantly Inherited Alzheimer Network observational study (DIAN-OBS), *The Lancet Neurology*. 15 (2016) 1317–1325. [https://doi.org/10.1016/S1474-4422\(16\)30229-0](https://doi.org/10.1016/S1474-4422(16)30229-0).
- [88] D.C. Ryman, N. Acosta-Baena, P.S. Aisen, T. Bird, A. Danek, N.C. Fox, A. Goate, P. Frommelt, B. Ghetti, J.B.S. Langbaum, F. Lopera, R. Martins, C.L. Masters, R.P. Mayeux, E. McDade, S. Moreno, E.M. Reiman, J.M. Ringman, S. Salloway, P.R. Schofield, R. Sperling, P.N. Tariot, C. Xiong, J.C. Morris, R.J. Bateman, Symptom onset in autosomal dominant Alzheimer disease: A systematic review and meta-analysis, *Neurology*. 83 (2014) 253–260. <https://doi.org/10.1212/WNL.0000000000000596>.

- [89] C.L. Maarouf, I.D. Daus, S. Spina, R. Vidal, T.A. Kokjohn, R.L. Patton, W.M. Kalback, D.C. Luehrs, D.G. Walker, E.M. Castaño, T.G. Beach, B. Ghetti, A.E. Roher, Histopathological and molecular heterogeneity among individuals with dementia associated with Presenilin mutations, *Molecular Neurodegeneration*. 3 (2008) 20. <https://doi.org/10.1186/1750-1326-3-20>.
- [90] E. Portelius, U. Andreasson, J.M. Ringman, K. Buerger, J. Daborg, P. Buchhave, O. Hansson, A. Harmsen, M.K. Gustavsson, E. Hanse, D. Galasko, H. Hampel, K. Blennow, H. Zetterberg, Distinct cerebrospinal fluid amyloid peptide signatures in sporadic and PSEN1 A431E-associated familial Alzheimer's disease, *Molecular Neurodegeneration*. 5 (2010) 2. <https://doi.org/10.1186/1750-1326-5-2>.
- [91] B.T. Hyman, C.H. Phelps, T.G. Beach, E.H. Bigio, N.J. Cairns, M.C. Carrillo, D.W. Dickson, C. Duyckaerts, M.P. Frosch, E. Masliah, S.S. Mirra, P.T. Nelson, J.A. Schneider, D.R. Thal, B. Thies, J.Q. Trojanowski, H. V. Vinters, T.J. Montine, National Institute on Aging-Alzheimer's Association guidelines for the neuropathologic assessment of Alzheimer's disease, *Alzheimer's and Dementia*. 8 (2012) 1–13. <https://doi.org/10.1016/j.jalz.2011.10.007>.
- [92] W.E. Klunk, J.C. Price, C.A. Mathis, N.D. Tsopelas, B.J. Lopresti, S.K. Ziolk, W. Bi, J.A. Hoge, A.D. Cohen, M.D. Ikonovic, J.A. Saxton, B.E. Snitz, D.A. Pollen, M. Moonis, C.F. Lippa, J.M. Swearer, K.A. Johnson, D.M. Rentz, A.J. Fischman, H.J. Aizenstein, S.T. DeKosky, Amyloid deposition begins in the striatum of presenilin-1 mutation carriers from two unrelated pedigrees, *Journal of Neuroscience*. 27 (2007) 6174–6184. <https://doi.org/10.1523/JNEUROSCI.0730-07.2007>.
- [93] C.M. Clark, J.A. Schneider, B.J. Bedell, T.G. Beach, W.B. Bilker, M.A. Mintun, M.J. Pontecorvo, F. Hefti, A.P. Carpenter, M.L. Flitter, M.J. Krautkramer, H.F. Kung, R.E. Coleman, P.M. Doraiswamy, A.S. Fleisher, M.N. Sabbagh, C.H. Sadowsky, E.M. Reiman, S.P. Zehntner, D.M. Skovronsky, for the A.-A.S. Group, Use of Florbetapir-PET for Imaging β -Amyloid Pathology, *JAMA*. 305 (2011) 275–283. <https://doi.org/10.1001/JAMA.2010.2008>.
- [94] C.M. Clark, M.J. Pontecorvo, T.G. Beach, B.J. Bedell, R.E. Coleman, P.M. Doraiswamy, A.S. Fleisher, E.M. Reiman, M.N. Sabbagh, C.H. Sadowsky, J.A. Schneider, A. Arora, A.P. Carpenter, M.L. Flitter, A.D. Joshi, M.J. Krautkramer, M. Lu, M.A. Mintun, D.M. Skovronsky, Cerebral PET with florbetapir compared with neuropathology at autopsy for detection of neuritic amyloid- β plaques: A prospective cohort study, *The Lancet Neurology*. 11 (2012) 669–678. [https://doi.org/10.1016/S1474-4422\(12\)70142-4](https://doi.org/10.1016/S1474-4422(12)70142-4).
- [95] I. Driscoll, J.C. Troncoso, G. Rudow, J. Sojkova, O. Pletnikova, Y. Zhou, M.A. Kraut, L. Ferrucci, C.A. Mathis, W.E. Klunk, R.J. O'Brien, C. Davatzikos, D.F. Wong, S.M. Resnick, Correspondence between in vivo ¹¹C-PiB-PET amyloid imaging and postmortem, region-matched assessment of plaques, *Acta Neuropathologica*. 124 (2012) 823–831. <https://doi.org/10.1007/s00401-012-1025-1>.

- [96] M.E. Murray, V.J. Lowe, N.R. Graff-Radford, A.M. Liesinger, A. Cannon, S.A. Przybelski, B. Rawal, J.E. Parisi, R.C. Petersen, K. Kantarci, O.A. Ross, R. Duara, D.S. Knopman, C.R. Jack, D.W. Dickson, Clinicopathologic and 11C-Pittsburgh compound B implications of Thal amyloid phase across the Alzheimer's disease spectrum, *Brain*. 138 (2015) 1370–1381. <https://doi.org/10.1093/brain/awv050>.
- [97] C. Curtis, J.E. Gamez, U. Singh, C.H. Sadowsky, T. Villena, M.N. Sabbagh, T.G. Beach, R. Duara, A.S. Fleisher, K.A. Frey, Z. Walker, A. Hunjan, C. Holmes, Y.M. Escovar, C.X. Vera, M.E. Agronin, J. Ross, A. Bozoki, M. Akinola, J. Shi, R. Vandenberghe, M.D. Ikonovic, P.F. Sherwin, I.D. Grachev, G. Farrar, A.P.L. Smith, C.J. Buckley, R. McLain, S. Salloway, Phase 3 trial of flutemetamol labeled with radioactive fluorine 18 imaging and neuritic plaque density, *JAMA Neurology*. 72 (2015) 287–294. <https://doi.org/10.1001/jamaneurol.2014.4144>.
- [98] M.D. Ikonovic, C.J. Buckley, K. Heurling, P. Sherwin, P.A. Jones, M. Zanette, C.A. Mathis, W.E. Klunk, A. Chakrabarty, J. Ironside, A. Ismail, C. Smith, D.R. Thal, T.G. Beach, G. Farrar, A.P.L. Smith, Post-mortem histopathology underlying β -amyloid PET imaging following flutemetamol F 18 injection, *Acta Neuropathologica Communications*. 4 (2016) 130. <https://doi.org/10.1186/s40478-016-0399-z>.
- [99] O. Sabri, M.N. Sabbagh, J. Seibyl, H. Barthel, H. Akatsu, Y. Ouchi, K. Senda, S. Murayama, K. Ishii, M. Takao, T.G. Beach, C.C. Rowe, J.B. Leverenz, B. Ghetti, J.W. Ironside, A.M. Catafau, A.W. Stephens, A. Mueller, N. Koglin, A. Hoffmann, K. Roth, C. Reininger, W.J. Schulz-Schaeffer, Florbetaben PET imaging to detect amyloid beta plaques in Alzheimer's disease: Phase 3 study, *Alzheimer's and Dementia*. 11 (2015) 964–974. <https://doi.org/10.1016/j.jalz.2015.02.004>.
- [100] D.R. Thal, A. Ronisz, T. Tousseyn, A. Rijal Upadhaya, K. Balakrishnan, R. Vandenberghe, M. Vandenbulcke, C.A.F. Von Arnim, M. Otto, T.G. Beach, J. Lilja, K. Heurling, A. Chakrabarty, A. Ismail, C. Buckley, A.P.L. Smith, S. Kumar, G. Farrar, J. Walter, Different aspects of Alzheimer's disease-related amyloid β -peptide pathology and their relationship to amyloid positron emission tomography imaging and dementia, *Acta Neuropathologica Communications*. 7 (2019) 178. <https://doi.org/10.1186/s40478-019-0837-9>.
- [101] F. Dé Rique Bard, R. Barbour, C. Cannon, R. Carretto, M. Fox, D. Games, T. Guido, K. Hoenow, K. Hu, K. Johnson-Wood, K. Khan, D. Kholodenko, C. Lee, M. Lee, R. Motter, M. Nguyen, A. Reed, D. Schenk, P. Tang, N. Vasquez, P. Seubert, T. Yednock, Epitope and isotype specificities of antibodies to-amyloid peptide for protection against Alzheimer's disease-like neuropathology, 2003.
- [102] E. Kida, K.E. Wisniewski, H.M. Wisniewski, Early amyloid β deposits show different immunoreactivity to the amino- and carboxy-terminal regions of β -peptide in Alzheimer's disease and Down's syndrome brain, *Neuroscience Letters*. 193 (1995) 105–108. [https://doi.org/10.1016/0304-3940\(95\)11678-P](https://doi.org/10.1016/0304-3940(95)11678-P).

- [103] M. Lalowski, A. Golabek, C.A. Lemere, D.J. Selkoe, H.M. Wisniewski, R.C. Beavis, B. Frangione, T. Wisniewski, The “Nonamyloidogenic” p3 fragment (amyloid β 17-42) is a major constituent of down’s syndrome cerebellar preamyloid, *Journal of Biological Chemistry*. 271 (1996) 33623–33631. <https://doi.org/10.1074/jbc.271.52.33623>.
- [104] C.A. Lemere, J.K. Blusztajn, H. Yamaguchi, T. Wisniewski, T.C. Saido, D.J. Selkoe, Sequence of deposition of heterogeneous amyloid β -peptides and APO E in down syndrome: Implications for initial events in amyloid plaque formation, *Neurobiology of Disease*. 3 (1996) 16–32. <https://doi.org/10.1006/nbdi.1996.0003>.
- [105] D.R. Thal, I. Sassin, C. Schultz, C. Haass, E. Braak, H. Braak, Fleecy amyloid deposits in the internal layers of the human entorhinal cortex are comprised of N-terminal truncated fragments of $a\beta$, *Journal of Neuropathology and Experimental Neurology*. 58 (1999) 210–216. <https://doi.org/10.1097/00005072-199902000-00010>.
- [106] C.R. Jack, D.S. Knopman, W.J. Jagust, L.M. Shaw, P.S. Aisen, M.W. Weiner, R.C. Petersen, J.Q. Trojanowski, Hypothetical model of dynamic biomarkers of the Alzheimer’s pathological cascade, *The Lancet Neurology*. 9 (2010) 119–128. [https://doi.org/10.1016/S1474-4422\(09\)70299-6](https://doi.org/10.1016/S1474-4422(09)70299-6).
- [107] V.L. Villemagne, S. Burnham, P. Bourgeat, B. Brown, K.A. Ellis, O. Salvado, C. Szoek, S.L. Macaulay, R. Martins, P. Maruff, D. Ames, C.C. Rowe, C.L. Masters, Amyloid β deposition, neurodegeneration, and cognitive decline in sporadic Alzheimer’s disease: A prospective cohort study, *The Lancet Neurology*. 12 (2013) 357–367. [https://doi.org/10.1016/S1474-4422\(13\)70044-9](https://doi.org/10.1016/S1474-4422(13)70044-9).
- [108] C.R. Jack, D.S. Knopman, W.J. Jagust, R.C. Petersen, M.W. Weiner, P.S. Aisen, L.M. Shaw, P. Vemuri, H.J. Wiste, S.D. Weigand, T.G. Lesnick, V.S. Pankratz, M.C. Donohue, J.Q. Trojanowski, Tracking pathophysiological processes in Alzheimer’s disease: An updated hypothetical model of dynamic biomarkers, *The Lancet Neurology*. 12 (2013) 207–216. [https://doi.org/10.1016/S1474-4422\(12\)70291-0](https://doi.org/10.1016/S1474-4422(12)70291-0).
- [109] P.T. Nelson, D.W. Dickson, J.Q. Trojanowski, C.R. Jack, P.A. Boyle, K. Arfanakis, R. Rademakers, I. Alafuzoff, J. Attems, C. Brayne, I.T.S. Coyle-Gilchrist, H.C. Chui, D.W. Fardo, M.E. Flanagan, G. Halliday, S.R.K. Hokkanen, S. Hunter, G.A. Jicha, Y. Katsumata, C.H. Kawas, C.D. Keene, G.G. Kovacs, W.A. Kukull, A.I. Levey, N. Makkinejad, T.J. Montine, S. Murayama, M.E. Murray, S. Nag, R.A. Rissman, W.W. Seeley, R.A. Sperling, C.L. White, L. Yu, J.A. Schneider, Limbic-predominant age-related TDP-43 encephalopathy (LATE): Consensus working group report, *Brain*. 142 (2019) 1503–1527. <https://doi.org/10.1093/brain/awz099>.
- [110] M.M. Corrada, J.A. Sonnen, R.C. Kim, C.H. Kawas, Microinfarcts are common and strongly related to dementia in the oldest-old: The 90+ study, *Alzheimer’s and Dementia*. 12 (2016) 900–908. <https://doi.org/10.1016/j.jalz.2016.04.006>.

- [111] D.C. Van Essen, S. Jbabdi, S.N. Sotiropoulos, C. Chen, K. Dikranian, T. Coalson, J. Harwell, T.E.J. Behrens, M.F. Glasser, Mapping Connections in Humans and Non-Human Primates. Aspirations and Challenges for Diffusion Imaging., in: *Diffusion MRI: From Quantitative Measurement to In Vivo Neuroanatomy: Second Edition*, Elsevier Inc., 2013: pp. 337–358. <https://doi.org/10.1016/B978-0-12-396460-1.00016-0>.
- [112] A. Charidimou, K. Farid, J.C. Baron, Amyloid-PET in sporadic cerebral amyloid angiopathy, *Neurology*. 89 (2017) 1490–1498. <https://doi.org/10.1212/WNL.0000000000004539>.
- [113] J. V. Ly, G.A. Donnan, V.L. Villemagne, J.A. Zavala, H. Ma, G. O’Keefe, S.J. Gong, R.M. Gunawan, T. Saunder, U. Ackerman, H. Tochon-Danguy, L. Churilov, T.G. Phan, C.C. Rowe, 11C-PIB binding is increased in patients with cerebral amyloid angiopathy-related hemorrhage, *Neurology*. 74 (2010) 487–493. <https://doi.org/10.1212/WNL.0b013e3181cef7e3>.
- [114] K.A. Johnson, M. Gregas, J.A. Becker, C. Kinnecom, D.H. Salat, E.K. Moran, E.E. Smith, J. Rosand, D.M. Rentz, W.E. Klunk, C.A. Mathis, J.C. Price, S.T. DeKosky, A.J. Fischman, S.M. Greenberg, Imaging of amyloid burden and distribution in cerebral amyloid angiopathy, *Annals of Neurology*. 62 (2007) 229–234. <https://doi.org/10.1002/ana.21164>.
- [115] J.M. Olichney, L.A. Hansen, C.R. Hofstetter, J.H. Lee, R. Katzman, L.J. Thal, Association between severe cerebral amyloid angiopathy and cerebrovascular lesions in Alzheimer disease is not a spurious one attributable to apolipoprotein E4, *Archives of Neurology*. 57 (2000) 869–874. <https://doi.org/10.1001/archneur.57.6.869>.
- [116] J.P.G. Vonsattel, R.H. Myers, E. Tessa Hedley-Whyte, A.H. Ropper, E.D. Bird, E.P. Richardson, Cerebral amyloid angiopathy without and with cerebral hemorrhages: A comparative histological study, *Annals of Neurology*. 30 (1991) 637–649. <https://doi.org/10.1002/ana.410300503>.
- [117] B.A. Gordon, T.M. Blazey, Y. Su, A. Hari-Raj, A. Dincer, S. Flores, J. Christensen, E. McDade, G. Wang, C. Xiong, N.J. Cairns, J. Hassenstab, D.S. Marcus, A.M. Fagan, C.R. Jack, R.C. Hornbeck, K.L. Paumier, B.M. Ances, S.B. Berman, A.M. Brickman, D.M. Cash, J.P. Chhatwal, S. Correia, S. Förster, N.C. Fox, N.R. Graff-Radford, C. la Fougère, J. Levin, C.L. Masters, M.N. Rossor, S. Salloway, A.J. Saykin, P.R. Schofield, P.M. Thompson, M.M. Weiner, D.M. Holtzman, M.E. Raichle, J.C. Morris, R.J. Bateman, T.L.S. Benzinger, Spatial patterns of neuroimaging biomarker change in individuals from families with autosomal dominant Alzheimer’s disease: a longitudinal study, *The Lancet Neurology*. 17 (2018) 241–250. [https://doi.org/10.1016/S1474-4422\(18\)30028-0](https://doi.org/10.1016/S1474-4422(18)30028-0).
- [118] M.J. Grothe, H. Barthel, J. Sepulcre, M. Dyrba, O. Sabri, S.J. Teipel, In vivo staging of regional amyloid deposition, *Neurology*. 89 (2017) 2031–2038. <https://doi.org/10.1212/WNL.0000000000004643>.

- [119] B.J. Hanseeuw, R.A. Betensky, E.C. Mormino, A.P. Schultz, J. Sepulcre, J.A. Becker, H.I.L. Jacobs, R.F. Buckley, M.R. LaPoint, P. Vannini, N.J. Donovan, J.P. Chhatwal, G.A. Marshall, K. V. Papp, R.E. Amariglio, D.M. Rentz, R.A. Sperling, K.A. Johnson, PET staging of amyloidosis using striatum, *Alzheimer's and Dementia*. 14 (2018) 1281–1292. <https://doi.org/10.1016/j.jalz.2018.04.011>.
- [120] R. La Joie, N. Ayakta, W.W. Seeley, E. Borys, A.L. Boxer, C. DeCarli, V. Doré, L.T. Grinberg, E. Huang, J.H. Hwang, M.D. Ikonomovic, C. Jack, W.J. Jagust, L.W. Jin, W.E. Klunk, J. Kofler, O.H. Lesman-Segev, S.N. Lockhart, V.J. Lowe, C.L. Masters, C.A. Mathis, C.L. McLean, B.L. Miller, D. Mungas, J.P. O'Neil, J.M. Olichney, J.E. Parisi, R.C. Petersen, H.J. Rosen, C.C. Rowe, S. Spina, P. Vemuri, V.L. Villemagne, M.E. Murray, G.D. Rabinovici, Multisite study of the relationships between antemortem [11 C]PIB-PET Centiloid values and postmortem measures of Alzheimer's disease neuropathology, *Alzheimer's and Dementia*. 15 (2019) 205–216. <https://doi.org/10.1016/j.jalz.2018.09.001>.
- [121] D.R. Thal, T.G. Beach, M. Zanette, J. Lilja, K. Heurling, A. Chakrabarty, A. Ismail, G. Farrar, C. Buckley, A.P.L. Smith, Estimation of amyloid distribution by [18F]flutemetamol PET predicts the neuropathological phase of amyloid β -protein deposition, *Acta Neuropathologica*. 136 (2018) 557–567. <https://doi.org/10.1007/s00401-018-1897-9>.
- [122] L.G. Caro, Chapter 16 High-Resolution Autoradiography, *Methods in Cell Biology*. 1 (1964) 327–363. [https://doi.org/10.1016/S0091-679X\(08\)62098-1](https://doi.org/10.1016/S0091-679X(08)62098-1).
- [123] T. Ding, T. Wu, H. Mazidi, O. Zhang, M.D. Lew, Single-molecule orientation localization microscopy for resolving structural heterogeneities between amyloid fibrils, *Optica*. 7 (2020) 602. <https://doi.org/10.1364/optica.388157>.
- [124] T.S. Burkoth, T.L.S. Benzinger, V. Urban, D.G. Lynn, S.C. Meredith, P. Thiyagarajan, Self-assembly of A β ((10-35))-PEG block copolymer fibrils [13], *Journal of the American Chemical Society*. 121 (1999) 7429–7430. <https://doi.org/10.1021/ja991233x>.
- [125] P. Thiyagarajan, T.S. Burkoth, V. Urban, S. Seifert, T.L.S. Benzinger, D.M. Morgan, D. Gordon, S.C. Meredith, D.G. Lynn, pH dependent self assembly of β -amyloid(10-35) and β -amyloid(10-35)-PEG3000, in: *Journal of Applied Crystallography*, 2000: pp. 535–539. <https://doi.org/10.1107/S0021889899014387>.
- [126] S.J. Frucht, E.H. Koo, β -amyloid protein is higher in alzheimer's disease brains: Description of aquantitative biochemical assay, *Journal of Neuropathology and Experimental Neurology*. 52 (1993) 640–647. <https://doi.org/10.1097/00005072-199311000-00011>.
- [127] S.A. Gravina, L. Ho, C.B. Eckman, K.E. Long, L. Otvos, L.H. Younkin, N. Suzuki, S.G. Younkin, Amyloid β protein (A β) in Alzheimer's disease brain. Biochemical and immunocytochemical analysis with antibodies specific for forms ending at A β 40 or A β 42(43), *Journal of Biological Chemistry*. 270 (1995) 7013–7016. <https://doi.org/10.1074/jbc.270.13.7013>.

- [128] B.R. Roberts, M. Lind, A.Z. Wagen, A. Rembach, T. Frugier, Q.X. Li, T.M. Ryan, C.A. McLean, J.D. Doecke, C.C. Rowe, V.L. Villemagne, C.L. Masters, Biochemically-defined pools of amyloid- β in sporadic Alzheimer's disease: Correlation with amyloid PET, *Brain*. 140 (2017) 1486–1498. <https://doi.org/10.1093/brain/awx057>.
- [129] G. Di Fede, M. Catania, E. Maderna, R. Ghidoni, L. Benussi, E. Tonoli, G. Giaccone, F. Moda, A. Paterlini, I. Campagnani, S. Sorrentino, L. Colombo, A. Kubis, E. Bistaffa, B. Ghetti, F. Tagliavini, Molecular subtypes of Alzheimer's disease, *Scientific Reports*. 8 (2018). <https://doi.org/10.1038/s41598-018-21641-1>.
- [130] S. Salloway, M. Farlow, E. McDade, D.B. Clifford, G. Wang, J.J. Llibre-Guerra, J.M. Hitchcock, S.L. Mills, A.M. Santacruz, A.J. Aschenbrenner, J. Hassenstab, T.L.S. Benzinger, B.A. Gordon, A.M. Fagan, K.A. Coalier, C. Cruchaga, A.A. Goate, R.J. Perrin, C. Xiong, Y. Li, J.C. Morris, B.J. Snider, C. Mummery, G.M. Surti, D. Hannequin, D. Wallon, S.B. Berman, J.J. Lah, I.Z. Jimenez-Velazquez, E.D. Roberson, C.H. van Dyck, L.S. Honig, R. Sánchez-Valle, W.S. Brooks, S. Gauthier, D.R. Galasko, C.L. Masters, J.R. Brosch, G.-Y.R. Hsiung, S. Jayadev, M. Formaglio, M. Masellis, R. Clarnette, J. Pariente, B. Dubois, F. Pasquier, C.R. Jack, R. Koeppe, P.J. Snyder, P.S. Aisen, R.G. Thomas, S.M. Berry, B.A. Wendelberger, S.W. Andersen, K.C. Holdridge, M.A. Mintun, R. Yaari, J.R. Sims, M. Baudler, P. Delmar, R.S. Doody, P. Fontoura, C. Giacobino, G.A. Kerchner, R.J. Bateman, A trial of gantenerumab or solanezumab in dominantly inherited Alzheimer's disease, *Nat Med*. (2021) 1–10. <https://doi.org/10.1038/s41591-021-01369-8>.
- [131] E. Liu, M.E. Schmidt, R. Margolin, R. Sperling, R. Koeppe, N.S. Mason, W.E. Klunk, C.A. Mathis, S. Salloway, N.C. Fox, D.L. Hill, A.S. Les, P. Collins, K.M. Gregg, J. Di, Y. Lu, I.C. Tudor, B.T. Wyman, K. Booth, S. Broome, E. Yuen, M. Grundman, H.R. Brashear, Amyloid- β 11C-PiB-PET imaging results from 2 randomized bapineuzumab phase 3 AD trials, *Neurology*. 85 (2015) 692–700. <https://doi.org/10.1212/WNL.0000000000001877>.
- [132] J.W. Landen, N. Andreasen, C.L. Cronenberger, P.F. Schwartz, A. Börjesson-Hanson, H. Östlund, C.A. Sattler, B. Binneman, M.M. Bednar, Ponezumab in mild-to-moderate Alzheimer's disease: Randomized phase II PET-PIB study, *Alzheimers Dement (N Y)*. 3 (2017) 393–401. <https://doi.org/10.1016/j.trci.2017.05.003>.
- [133] J. Sevigny, P. Chiao, T. Bussière, P.H. Weinreb, L. Williams, M. Maier, R. Dunstan, S. Salloway, T. Chen, Y. Ling, J. O'Gorman, F. Qian, M. Arastu, M. Li, S. Chollate, M.S. Brennan, O. Quintero-Monzon, R.H. Scannevin, H.M. Arnold, T. Engber, K. Rhodes, J. Ferrero, Y. Hang, A. Mikulskis, J. Grimm, C. Hock, R.M. Nitsch, A. Sandrock, The antibody aducanumab reduces A β plaques in Alzheimer's disease, *Nature*. 537 (2016) 50–56. <https://doi.org/10.1038/nature19323>.
- [134] M.A. Mintun, A.C. Lo, C. Duggan Evans, A.M. Wessels, P.A. Ardayfio, S.W. Andersen, S. Shcherbinin, J. Sparks, J.R. Sims, M. Brys, L.G. Apostolova, S.P. Salloway, D.M. Skovronsky, Donanemab in Early Alzheimer's Disease, *New England Journal of Medicine*. 384 (2021) 1691–1704. <https://doi.org/10.1056/NEJMoa2100708>.

- [135] G. Klein, P. Delmar, N. Voyle, S. Rehal, C. Hofmann, D. Abi-Saab, M. Andjelkovic, S. Ristic, G. Wang, R. Bateman, G.A. Kerchner, M. Baudler, P. Fontoura, R. Doody, Gantenerumab reduces amyloid- β plaques in patients with prodromal to moderate Alzheimer's disease: a PET substudy interim analysis, *Alzheimer's Research & Therapy*. 11 (2019) 101. <https://doi.org/10.1186/s13195-019-0559-z>.
- [136] C.J. Swanson, Y. Zhang, S. Dhadda, J. Wang, J. Kaplow, R.Y.K. Lai, L. Lannfelt, H. Bradley, M. Rabe, A. Koyama, L. Reyderman, D.A. Berry, S. Berry, R. Gordon, L.D. Kramer, J.L. Cummings, A randomized, double-blind, phase 2b proof-of-concept clinical trial in early Alzheimer's disease with lecanemab, an anti-A β protofibril antibody, *Alz Res Therapy*. 13 (2021) 80. <https://doi.org/10.1186/s13195-021-00813-8>.
- [137] L.S. Honig, B. Vellas, M. Woodward, M. Boada, R. Bullock, M. Borrie, K. Hager, N. Andreasen, E. Scarpini, H. Liu-Seifert, M. Case, R.A. Dean, A. Hake, K. Sundell, V.P. Hoffmann, C. Carlson, R. Khanna, M. Mintun, R. DeMattos, K.J. Selzler, E. Siemers, Trial of Solanezumab for Mild Dementia Due to Alzheimer's Disease, *New England Journal of Medicine*. (2018). <https://doi.org/10.1056/NEJMoa1705971>.
- [138] D.A. Wolk, Z. Zhang, S. Boudhar, C.M. Clark, M.J. Pontecorvo, S.E. Arnold, Amyloid imaging in Alzheimer's disease: comparison of Florbetapir and Pittsburgh Compound-B PET, *J Neurol Neurosurg Psychiatry*. 83 (2012) 923–926. <https://doi.org/10.1136/jnnp-2012-302548>.
- [139] R. Ni, P.-G. Gillberg, A. Bergfors, A. Marutle, A. Nordberg, Amyloid tracers detect multiple binding sites in Alzheimer's disease brain tissue, *Brain*. 136 (2013) 2217–2227. <https://doi.org/10.1093/brain/awt142>.
- [140] Y. Su, S. Flores, G. Wang, R.C. Hornbeck, B. Speidel, N. Joseph-Mathurin, A.G. Vlassenko, B.A. Gordon, R.A. Koeppe, W.E. Klunk, C.R. Jack, Jr, M.R. Farlow, S. Salloway, B.J. Snider, S.B. Berman, E.D. Roberson, J. Brosch, I. Jimenez-Velazques, C.H. van Dyck, D. Galasko, S.H. Yuan, S. Jayadev, L.S. Honig, S. Gauthier, G.-Y.R. Hsiung, M. Masellis, W.S. Brooks, M. Fulham, R. Clarnette, C.L. Masters, D. Wallon, D. Hannequin, B. Dubois, J. Pariente, R. Sanchez-Valle, C. Mummery, J.M. Ringman, M. Bottlaender, G. Klein, S. Milosavljevic-Ristic, E. McDade, C. Xiong, J.C. Morris, R.J. Bateman, T.L.S. Benzinger, Comparison of Pittsburgh compound B and florbetapir in cross-sectional and longitudinal studies, *Alzheimer's & Dementia : Diagnosis, Assessment & Disease Monitoring*. 11 (2019) 180. <https://doi.org/10.1016/j.dadm.2018.12.008>.
- [141] S.M. Landau, B.A. Thomas, L. Thurfjell, M. Schmidt, R. Margolin, M. Mintun, M. Pontecorvo, S.L. Baker, W.J. Jagust, the Alzheimer's Disease Neuroimaging Initiative, Amyloid PET imaging in Alzheimer's disease: a comparison of three radiotracers, *Eur J Nucl Med Mol Imaging*. 41 (2014) 1398–1407. <https://doi.org/10.1007/s00259-014-2753-3>.
- [142] B.A. Thomas, K. Erlandsson, M. Modat, L. Thurfjell, R. Vandenberghe, S. Ourselin, B.F. Hutton, The importance of appropriate partial volume correction for PET quantification in

Alzheimer's disease, *Eur J Nucl Med Mol Imaging*. 38 (2011) 1104–1119.
<https://doi.org/10.1007/s00259-011-1745-9>.

- [143] W.E. Klunk, R.A. Koeppe, J.C. Price, T.L. Benzinger, M.D. Devous, W.J. Jagust, K.A. Johnson, C.A. Mathis, D. Minhas, M.J. Pontecorvo, C.C. Rowe, D.M. Skovronsky, M.A. Mintun, The Centiloid Project: standardizing quantitative amyloid plaque estimation by PET, *Alzheimers Dement*. 11 (2015) 1–15.e1–4. <https://doi.org/10.1016/j.jalz.2014.07.003>.
- [144] T.L.S. Benzinger, T. Blazey, C.R. Jack, R.A. Koeppe, Y. Su, C. Xiong, M.E. Raichle, A.Z. Snyder, B.M. Ances, R.J. Bateman, N.J. Cairns, A.M. Fagan, A. Goate, D.S. Marcus, P.S. Aisen, J.J. Christensen, L. Ercole, R.C. Hornbeck, A.M. Farrar, P. Aldea, M.S. Jasielec, C.J. Owen, X. Xie, R. Mayeux, A. Brickman, E. McDade, W. Klunk, C.A. Mathis, J. Ringman, P.M. Thompson, B. Ghetti, A.J. Saykin, R.A. Sperling, K.A. Johnson, S. Salloway, S. Correia, P.R. Schofield, C.L. Masters, C. Rowe, V.L. Villemagne, R. Martins, S. Ourselin, M.N. Rossor, N.C. Fox, D.M. Cash, M.W. Weiner, D.M. Holtzman, V.D. Buckles, K. Moulder, J.C. Morris, Regional variability of imaging biomarkers in autosomal dominant Alzheimer's disease, *Proc Natl Acad Sci U S A*. 110 (2013) E4502–4509.
<https://doi.org/10.1073/pnas.1317918110>.
- [145] J.C. Morris, P.S. Aisen, R.J. Bateman, T.L.S. Benzinger, N.J. Cairns, A.M. Fagan, B. Ghetti, A.M. Goate, D.M. Holtzman, W.E. Klunk, E. McDade, D.S. Marcus, R.N. Martins, C.L. Masters, R. Mayeux, A. Oliver, K. Quaid, J.M. Ringman, M.N. Rossor, S. Salloway, P.R. Schofield, N.J. Selsor, R.A. Sperling, M.W. Weiner, C. Xiong, K.L. Moulder, V.D. Buckles, Developing an international network for Alzheimer research: The Dominantly Inherited Alzheimer Network, *Clin Investig (Lond)*. 2 (2012) 975–984.
<https://doi.org/10.4155/cli.12.93>.
- [146] N.S. McKay, B.A. Gordon, R.C. Hornbeck, C.R. Jack, R. Koeppe, S. Flores, S. Keefe, D.A. Hobbs, N. Joseph-Mathurin, Q. Wang, F. Rahmani, C.D. Chen, A. McCullough, D. Koudelis, J. Chua, B.M. Ances, P.R. Millar, M. Nickels, R.J. Perrin, R.F. Allegri, S.B. Berman, W.S. Brooks, D.M. Cash, J.P. Chhatwal, M.R. Farlow, N.C. Fox, M. Fulham, B. Ghetti, N. Graff-Radford, T. Ikeuchi, G. Day, W. Klunk, J. Levin, J.-H. Lee, R. Martins, C.L. Masters, J. McConathy, H. Mori, J.M. Noble, C. Rowe, S. Salloway, R. Sanchez-Valle, P.R. Schofield, H. Shimada, M. Shoji, Y. Su, K. Suzuki, J. Vöglein, I. Yakushev, L. Swisher, C. Cruchaga, J. Hassenstab, C. Karch, E. McDade, C. Xiong, J.C. Morris, R.J. Bateman, T.L.S. Benzinger, D.I.A. Network, Neuroimaging within the Dominantly Inherited Alzheimer's Network (DIAN): PET and MRI, (2022) 2022.03.25.485799.
<https://doi.org/10.1101/2022.03.25.485799>.
- [147] Y. Benjamini, Y. Hochberg, Controlling the False Discovery Rate: A Practical and Powerful Approach to Multiple Testing, *Journal of the Royal Statistical Society: Series B (Methodological)*. 57 (1995) 289–300. <https://doi.org/10.1111/j.2517-6161.1995.tb02031.x>.
- [148] V. Tentolouris-Piperas, N.S. Ryan, D.L. Thomas, K.M. Kinnunen, Brain imaging evidence of early involvement of subcortical regions in familial and sporadic Alzheimer's disease, *Brain Research*. 1655 (2017) 23–32. <https://doi.org/10.1016/j.brainres.2016.11.011>.

- [149] W.E. Klunk, J.C. Price, C.A. Mathis, N.D. Tsopelas, B.J. Lopresti, S.K. Ziolko, W. Bi, J.A. Hoge, A.D. Cohen, M.D. Ikonomovic, J.A. Saxton, B.E. Snitz, D.A. Pollen, M. Moonis, C.F. Lippa, J.M. Swearer, K.A. Johnson, D.M. Rentz, A.J. Fischman, H.J. Aizenstein, S.T. DeKosky, Amyloid Deposition Begins in the Striatum of Presenilin-1 Mutation Carriers from Two Unrelated Pedigrees, *J Neurosci.* 27 (2007) 6174–6184. <https://doi.org/10.1523/JNEUROSCI.0730-07.2007>.
- [150] C.D. Chen, N. Joseph-Mathurin, N. Sinha, A. Zhou, Y. Li, K. Friedrichsen, A. McCullough, E.E. Franklin, R. Hornbeck, B. Gordon, V. Sharma, C. Cruchaga, A. Goate, C. Karch, E. McDade, C. Xiong, R.J. Bateman, B. Ghetti, J.M. Ringman, J. Chhatwal, C.L. Masters, C. McLean, T. Lashley, Y. Su, R. Koeppe, C. Jack, W.E. Klunk, J.C. Morris, R.J. Perrin, N.J. Cairns, T.L.S. Benzinger, Comparing amyloid- β plaque burden with antemortem PiB PET in autosomal dominant and late-onset Alzheimer disease, *Acta Neuropathol.* 142 (2021) 689–706. <https://doi.org/10.1007/s00401-021-02342-y>.
- [151] T. Annus, L.R. Wilson, Y.T. Hong, J. Acosta-Cabronero, T.D. Fryer, A. Cardenas-Blanco, R. Smith, I. Boros, J.P. Coles, F.I. Aigbirhio, D.K. Menon, S.H. Zaman, P.J. Nestor, A.J. Holland, The pattern of amyloid accumulation in the brains of adults with Down syndrome, *Alzheimers Dement.* 12 (2016) 538–545. <https://doi.org/10.1016/j.jalz.2015.07.490>.
- [152] S.L. Lowe, B.A. Willis, A. Hawdon, F. Natanegara, L. Chua, J. Foster, S. Shcherbinin, P. Ardayfio, J.R. Sims, Donanemab (LY3002813) dose-escalation study in Alzheimer's disease, *Alzheimers Dement (N Y)*. 7 (2021) e12112. <https://doi.org/10.1002/trc2.12112>.
- [153] S. Retout, R. Gieschke, D. Serafin, C. Weber, N. Frey, C. Hofmann, Disease Modeling and Model-Based Meta-Analyses to Define a New Direction for a Phase III Program of Gantenerumab in Alzheimer's Disease, *Clinical Pharmacology & Therapeutics.* 111 (2022) 857–866. <https://doi.org/10.1002/cpt.2535>.
- [154] M.D. Sweeney, A.P. Sagare, B.V. Zlokovic, Blood–brain barrier breakdown in Alzheimer disease and other neurodegenerative disorders, *Nat Rev Neurol.* 14 (2018) 133–150. <https://doi.org/10.1038/nrneurol.2017.188>.
- [155] R. Potter, B.W. Patterson, D.L. Elbert, V. Ovod, T. Kasten, W. Sigurdson, K. Mawuenyega, T. Blazey, A. Goate, R. Chott, K.E. Yarasheski, D.M. Holtzman, J.C. Morris, T.L.S. Benzinger, R.J. Bateman, Increased in vivo Amyloid- β 42 production, exchange, and irreversible loss in Presenilin Mutations Carriers, *Sci Transl Med.* 5 (2013) 10.1126/scitranslmed.3005615. <https://doi.org/10.1126/scitranslmed.3005615>.
- [156] J. Shah, F. Gao, B. Li, V. Ghisays, J. Luo, Y. Chen, W. Lee, Y. Zhou, T.L.S. Benzinger, E.M. Reiman, K. Chen, Y. Su, T. Wu, Deep residual inception encoder-decoder network for amyloid PET harmonization, *Alzheimers Dement.* (2022). <https://doi.org/10.1002/alz.12564>.

- [157] N. Tolboom, M. Yaqub, R. Boellaard, G. Luurtsema, A.D. Windhorst, P. Scheltens, A.A. Lammertsma, B.N.M. van Berckel, Test-retest variability of quantitative [¹¹C]PIB studies in Alzheimer's disease, *Eur J Nucl Med Mol Imaging*. 36 (2009) 1629–1638. <https://doi.org/10.1007/s00259-009-1129-6>.
- [158] A.D. Joshi, M.J. Pontecorvo, C.M. Clark, A.P. Carpenter, D.L. Jennings, C.H. Sadowsky, L.P. Adler, K.D. Kovnat, J.P. Seibyl, A. Arora, K. Saha, J.D. Burns, M.J. Lowrey, M.A. Mintun, D.M. Skovronsky, the F.F. 18 S. Investigators, Performance Characteristics of Amyloid PET with Florbetapir F 18 in Patients with Alzheimer's Disease and Cognitively Normal Subjects, *Journal of Nuclear Medicine*. 53 (2012) 378–384. <https://doi.org/10.2967/jnumed.111.090340>.
- [159] K.A. Johnson, R.A. Sperling, C.M. Gidicsin, J.S. Carmasin, J.E. Maye, R.E. Coleman, E.M. Reiman, M.N. Sabbagh, C.H. Sadowsky, A.S. Fleisher, P. Murali Doraiswamy, A.P. Carpenter, C.M. Clark, A.D. Joshi, M. Lu, M. Grundman, M.A. Mintun, M.J. Pontecorvo, D.M. Skovronsky, Florbetapir (F18-AV-45) PET to assess amyloid burden in Alzheimer's disease dementia, mild cognitive impairment, and normal aging, *Alzheimer's & Dementia*. 9 (2013) S72–S83. <https://doi.org/10.1016/j.jalz.2012.10.007>.
- [160] A.K. Jha, B. Caffo, E.C. Frey, A no-gold-standard technique for objective assessment of quantitative nuclear-medicine imaging methods, *Phys Med Biol*. 61 (2016) 2780–2800. <https://doi.org/10.1088/0031-9155/61/7/2780>.
- [161] J.W. Hoppin, M.A. Kupinski, G.A. Kastis, E. Clarkson, H.H. Barrett, Objective comparison of quantitative imaging modalities without the use of a gold standard, *IEEE Transactions on Medical Imaging*. 21 (2002) 441–449. <https://doi.org/10.1109/TMI.2002.1009380>.
- [162] A.K. Jha, E. Mena, B. Caffo, S. Ashrafinia, A. Rahmim, E. Frey, R.M. Subramaniam, Practical no-gold-standard evaluation framework for quantitative imaging methods: application to lesion segmentation in positron emission tomography, *J Med Imaging (Bellingham)*. 4 (2017) 011011. <https://doi.org/10.1117/1.JMI.4.1.011011>.
- [163] Z. Liu, Z. Li, J.C. Mhlanga, B.A. Siegel, A.K. Jha, No-gold-standard evaluation of quantitative imaging methods in the presence of correlated noise, *Proceedings of SPIE--the International Society for Optical Engineering*. 12035 (2022). <https://doi.org/10.1117/12.2605762>.